

Application of InSAR Analysis to Earthquake-Induced Liquefaction Observations

by

Hanze Yao

A dissertation submitted in partial satisfaction of the

requirements for the degree of

Doctor of Philosophy

in

Engineering - Civil and Environmental Engineering

in the

Graduate Division

of the

University of California, Berkeley

Committee in charge:

Professor Robert Kayen, Co-chair

Professor Nicholas Sitar, Co-chair

Professor Roland Bürgmann

Professor Dimitrios Zekkos

Summer 2023

Application of InSAR Analysis to Earthquake-Induced Liquefaction Observations

Copyright 2023
by
Hanze Yao

Abstract

Application of InSAR Analysis to Earthquake-Induced Liquefaction Observations

by

Hanze Yao

Doctor of Philosophy in Engineering - Civil and Environmental Engineering

University of California, Berkeley

Professor Robert Kayen, Co-chair

Professor Nicholas Sitar, Co-chair

Liquefaction mapping currently relies on visual analysis of satellite and aerial images that covers the area of interest. Sand boils, lateral spreading and ground settlement are common evidences that researchers look for when identifying liquefaction damaged areas after an earthquake. However, this method can be unreliable. For example, irrelevant objects on images like burnt rice stalks in agricultural field can be misclassified as sand boils. Interferometric Synthetic Aperture Radar (InSAR), as a remote sensing technique, is widely used for characterizing ground displacement with high resolution and accuracy. With the increasing availability of free InSAR data sets and the short return period of modern satellites, co-seismic InSAR analysis becomes possible shortly after the occurrence of an earthquake. Therefore, InSAR is well suited for analyzing lateral and vertical displacement caused by liquefaction and works as a reference for field reconnaissance teams. In this thesis three earthquake case histories with significant liquefaction damage, specifically the 2010-2011 Canterbury Earthquake Sequence including 2010 Darfield Earthquake and 2011 Christchurch Earthquake, the 2016 Kumamoto Earthquake and the 2018 Hokkaido Eastern Iburi Earthquake are analyzed with four different InSAR methods: differential InSAR analysis, persistent scatter time series analysis, coherence-based method and pixel (dense) offset analysis. The co-seismic displacement results are converted into vertical and horizontal displacements to compare with field observations from reconnaissances right after these earthquakes. After comparing the effectiveness of the different methods and different satellites at each site, an InSAR workflow for analysing earthquake-induced liquefaction observations is presented.

To my family

I am truly grateful to your unconditional support throughout the years that makes this work possible.

Contents

| | |
|---|------|
| Contents | ii |
| List of Figures | iv |
| List of Tables | viii |
| 1 Introduction | 1 |
| 1.1 Overview | 1 |
| 1.2 Objectives | 2 |
| 1.3 Outline | 3 |
| 2 Methodology | 4 |
| 2.1 InSAR analysis methods used in this research | 4 |
| 2.2 Atmospheric phase correction | 9 |
| 3 Canterbury Earthquake Sequence Case Study | 10 |
| 3.1 Introduction | 10 |
| 3.2 Local Geology | 10 |
| 3.3 InSAR analysis results compared to field observations | 11 |
| 3.4 Discussion | 28 |
| 4 Kumamoto Earthquake Case Study | 34 |
| 4.1 Introduction | 34 |
| 4.2 Local geology | 34 |
| 4.3 InSAR analysis results compared to field observations | 35 |
| 4.4 Discussion | 48 |
| 5 Hokkaido Eastern Iburi Earthquake Case Study | 53 |
| 5.1 Introduction | 53 |
| 5.2 Local Geology | 53 |
| 5.3 InSAR analysis results compared to field observations | 54 |
| 5.4 Discussion | 70 |

| | |
|---|-----------|
| 6 Conclusion and future work | 73 |
| 6.1 Conclusions on the effectiveness of the four InSAR analysis methods on earthquake-induced liquefaction analysis | 73 |
| 6.2 InSAR workflow for analysing earthquake-induced liquefaction | 75 |
| 6.3 Future work | 77 |
| Bibliography | 79 |
| A Manual for InSAR Liquefaction Analysis Workflow | 87 |
| A.1 Find SAR data set | 87 |
| A.2 ISCE2 workflow | 87 |
| A.3 PS analysis workflow | 89 |
| A.4 Post-processing in QGIS workflow | 90 |

List of Figures

| | | |
|------|--|----|
| 2.1 | Stripmap and TOPS acquisition mode [17] | 6 |
| 2.2 | Schematic illustration of the pixel offset method (credit to the Jupyter notebook created by Bryan Riel and Brent Minchew from MIT). | 8 |
| 3.1 | (a) Simplified Christchurch geology map [49]. (b) Simplified soil profile along cross section A-A' [6, 49]. | 11 |
| 3.2 | (a) Greendale fault (2010 Darfield earthquake), co-seismic pair between scenes from 03/11/2010 and 09/11/2010, positive displacement is moving away from the satellite in the LOS direction. (b) Port Hills fault (2011 Christchurch earthquake), co-seismic pair between scenes from 10/27/2010 and 03/14/2011, positive displacement is moving away from the satellite in the LOS direction. | 13 |
| 3.3 | Maximum relative fault displacement in the LOS direction is \sim 3.4 m in the green circle. The light green zone near fault trace is due to the decorrelation caused by fault rupture. | 14 |
| 3.4 | (a) 2010 Darfield earthquake LOS displacements (b) 2011 Christchurch earthquake LOS displacements | 15 |
| 3.5 | (a) 2010 Darfield earthquake liquefaction map overlay (b) 2011 Christchurch earthquake liquefaction map overlay | 16 |
| 3.6 | Locations with significant lateral spreading along Avon River in the 2010 Darfield earthquake [13]. | 18 |
| 3.7 | (a) Avon River left bank LOS displacement (b) Avon River right bank LOS displacement (The locations of these data points are marked from west to east along the Avon River in Figure 3.6). The theoretical minimum and maximum LOS displacements on both banks of the Avon River are converted from the field measurement in Table 3.2 assuming no vertical displacement. | 19 |
| 3.8 | (a) 2010 Darfield earthquake liquefaction map overlay in Kaiapoi (b) 2011 Christchurch earthquake liquefaction map overlay in Kaiapoi [69] | 20 |
| 3.9 | Lateral spreading in Kaiapoi following the 2010 Darfield earthquake. The red lines indicate where Cubrinovski et al. 2012 [13] measured lateral ground movement. | 21 |
| 3.10 | Converted lateral ground movement (in the direction perpendicular to the rivers or streams on the bank where lateral ground movement was measured in the field assuming no vertical displacement) from InSAR results (The locations of these data points are marked in Figure 3.9) | 22 |

| | |
|---|----|
| 3.11 InSAR result in Kaiapoi along Charles St following the 2010 Darfield earthquake. (The google earth map is from 2022.) Red zones indicate 7.1-18.4 cm settlement caused by liquefaction. | 23 |
| 3.12 InSAR result in western Kaiapoi following the 2010 Darfield earthquake. (The google earth map is from 2022.) The red zone south of Murphy park indicates 4.3-12.2 cm settlement caused by liquefaction. | 23 |
| 3.13 InSAR result in eastern Kaiapoi following the 2010 Darfield earthquake. (The google earth map is from 2022.) The red zone indicates 4.7-20.5 cm settlement caused by liquefaction. | 24 |
| 3.14 (a) 2010 Darfield earthquake liquefaction map overlay near Heathcote River (b) 2011 Christchurch earthquake liquefaction map overlay near Heathcote River . . | 25 |
| 3.15 InSAR result in St. Martins following the 2011 Christchurch earthquake. (The google earth map is from 2022) | 26 |
| 3.16 Preliminary model of the southeast-dipping fault (rectangular area) that ruptured across the southern part of Christchurch and northern Port Hills during the 2011 Christchurch earthquake. The red, green and yellow symbols show some of the GPS stations whose displacements were used to derive this fault slip model (GNS Media Release, April 2011). | 26 |
| 3.17 (a) InSAR result from the co-seismic pair of the 2010 Darfield earthquake in Christchurch CBD (b) InSAR result from the co-seismic pair of the 2011 Christchurch earthquake in Christchurch CBD | 29 |
| 3.18 Location of geomorphic feature in area of apartment and duplex complexes north of Salisbury Street in CBD [15]. Figure 3.19 corresponds to Figure 6 and Figure 3.20 corresponds to Figure 8 in this figure. | 30 |
| 3.19 Apartment complex: A) looking south from northern building showing tilt of southern building, and B) looking north at liquefaction feature at edge of southern building (7 March 2011; S43.52434 E172.64432) [15]. | 30 |
| 3.20 Duplex housing complex: A) looking north at the center building, and B) close- up of ground settlement next to the center building (16 March 2011; S43.52399 E172.64417) [15]. | 31 |
| 3.21 The InSAR result at the location of the building complex in Figure 3.18 . . . | 31 |
| 3.22 Liquefaction-induced differential settlement and sliding of building in the CBD (24 March 2011; S43.52878 E172.64252) [15]. | 32 |
| 3.23 Building undergoing significant liquefaction-induced differential settlement due to part of it being founded on the liquefaction feature in this area (24 March 2011; S43.52878 E172.64252) [15]. | 32 |
| 3.24 The InSAR result at the location of the two buildings in Figure 3.22 and Figure 3.23 | 33 |

| | | |
|------|--|----|
| 4.1 | Source fault model for the hosts of both the foreshock and the mainshock. The three white rectangles denote fault planes projected onto the surface. Black and white arrows at each GNSS station indicate horizontal displacements observed and predicted from the source model. (Background interferogram is from the ALOS-2 co-seismic pair between March 7th, 2016 and April 18th, 2016 on descending track) [40] | 36 |
| 4.2 | E-W fault movement map (East movement is positive.) | 38 |
| 4.3 | N-S fault movement map (North movement is positive.) | 38 |
| 4.4 | Vertical fault movement map (Uplift is positive.) | 39 |
| 4.5 | Irregular blue lines show surface ruptures caused by liquefaction-induced lateral spreading interpreted from aerial photos [71]. Total horizontal displacement map is from Fujiwara et al. 2017 [23]. | 40 |
| 4.6 | Photos of typical compression and extension surface features in the Matoishi area [23]. | 41 |
| 4.7 | E-W displacement map in the Aso Valley (East movement is positive.) | 43 |
| 4.8 | N-S displacement map in the Aso Valley (North movement is positive.) | 43 |
| 4.9 | Vertical displacement map in the Aso Valley (Uplift is positive.) | 44 |
| 4.10 | Total Horizontal displacement map in the Aso Valley | 44 |
| 4.11 | Displacement map in Uchinomaki | 45 |
| 4.12 | Displacement map in Kario | 45 |
| 4.13 | Displacement map in Matoishi | 46 |
| 4.14 | E-W displacement at the locations of four field observations | 46 |
| 4.15 | Liquefaction map in Kumamoto City | 47 |
| 4.16 | Normalized coherence change in Aso Valley | 49 |
| 4.17 | Normalized coherence change in Kumamoto City with liquefaction damaged areas bounded by red lines | 49 |
| 4.18 | Updated normalized coherence change in Kumamoto City with liquefaction damaged areas bounded by red lines | 50 |
| 4.19 | Normalized coherence change at the artificial island to the west of Kumamoto City | 50 |
| 4.20 | Normalized coherence change at the south-east corner of Shirakawa River | 51 |
| 4.21 | Normalized coherence change at the bridge crossing a tributary of the Midorikawa River at the east of Kumamoto City | 51 |
| 5.1 | a and b show the vertical and E-W displacement maps derived from ALOS-2 data set. c and d show the vertical and E-W displacement maps predicted by the fault model. e and f show the residuals of the two displacement components. [44] . | 55 |
| 5.2 | The co-seismic LOS displacement map for persistent scatters on descending track (Positive displacement is moving away from the satellite.) | 57 |
| 5.3 | Co-seismic Vertical and E-W displacement plots from 3D decomposition at the 12 location in Figure 5.2 (Positive displacement is uplift and eastward displacement.) | 58 |
| 5.4 | Uneven subsidence of road due to liquefaction with sand boiling in Tomakomai (photo taken by Watabe, Y., Hokkaido Univ.) | 58 |

| | | |
|------|---|----|
| 5.5 | (a) Minor settlement of concrete slabs. (b) Sand boils surrounding a light tower. Sand boils near the southern seawall and in the container backyard. Sand boils in the undeveloped area between the marine container facility and the HEPCO coal plant.(photos taken by the GEER field reconnaissance team [42]) | 59 |
| 5.6 | Sand boils in an undeveloped area where Tomato-Atsuma Thermal Electric Power Plant is in sight (photo taken by the GEER field reconnaissance team [42]) | 60 |
| 5.7 | Normalized coherence change map in Tomakomai | 61 |
| 5.8 | Sand boils observed by Japanese researchers (left). Blue tarps on top of the flood control levee (right). (photos taken by the GEER field reconnaissance team [42]) | 62 |
| 5.9 | Normalized coherence change map in Mukawa | 62 |
| 5.10 | Blue tarps on top of the levee found on Google Earth image taken in September 2018 | 63 |
| 5.11 | (a) Head scarp of the flow-failure (b) Older building with mat foundation on the left and contemporary building with pile foundation on the right. Structures' performance highly depends on foundation design. (photos taken by the GEER field reconnaissance team [42]) | 64 |
| 5.12 | Normalized coherence change map in Sapporo City where flow-failure occurred (Liquefaction-damaged areas bounded in blue lines are from Ishikawa et al. 2021 [36]) | 65 |
| 5.13 | Liquefaction damaged area above the Namboku subway line [36] | 66 |
| 5.14 | Liquefaction damaged area above the Toho subway line [36]) | 66 |
| 5.15 | Situation near Kita 34 Station two days after the earthquake (location corresponds to the number in Figure 5.13) [36]) | 67 |
| 5.16 | Situation along the Higashi 15-chome Tonden street two days after the earthquake (location corresponds to the number in Figure 5.14) [36]) | 68 |
| 5.17 | Normalized coherence change map of the area with liquefaction damage on roads above subway lines | 69 |
| 5.18 | (a) Landslide in Yoshino village (south) (b) Landslide in Yoshino village (north) (c) Landslide in Tomisato village (water treatment plant [78] | 71 |
| 5.19 | Vertical displacement map derived from the pixel offset analysis of Yoshino village and Tomisato village (Horizontal displacement and vertical displacement in parentheses are labeled at 10 locations on the sliding surface.) | 72 |
| 6.1 | InSAR workflow for earthquake induced liquefaction analysis (ISCE2 is the second iteration of the InSAR Scientific Computing Environment developed by JPL.) . . | 76 |
| 6.2 | Artist Rendering of NISAR from NISAR official website | 78 |
| A.1 | ASF Vertex Data Search Website | 88 |
| A.2 | Modification required before using SNAP2STAMPS | 90 |
| A.3 | MATLAB script used to generate outputs in CSV format | 91 |

List of Tables

| | | |
|-----|--|----|
| 2.1 | SAR data sets used in this research | 6 |
| 3.1 | SAR data sets used in the Canterbury earthquake sequence case study | 12 |
| 3.2 | Range of measured permanent lateral ground displacements induced by lateral spreading at or near the waterway after the 2010 Darfield earthquake [13] | 17 |
| 4.1 | SAR data sets used in the 2016 Kumamoto earthquake case study | 37 |
| 4.2 | The maximum horizontal displacement and the vertical displacement range along the cross sections b, c and d in Figure 4.5 from the InSAR analysis results in Fujiwara et al. 2017 [23] | 47 |
| 4.3 | SAR data sets used in the coherence change method | 48 |
| 5.1 | SAR data sets used in the 2018 Kumamoto earthquake case study | 56 |
| 5.2 | Co-seismic Vertical and E-W displacement from 3D decomposition at the 12 location in Figure 5.2 (Positive displacement is uplift and eastward displacement.) | 57 |
| 5.3 | SAR data sets used in the coherence-change analysis | 61 |
| 5.4 | Vertical displacement from the PS analysis result at the locations with settlement in Figure 5.13 and Figure 5.14 (Settlement is negative.) | 69 |

Acknowledgments

First of all I would like to thank my advisor Professor Robert Kayen. You brought me to the world of earthquake research. I still remember the surface wave tests we did together at Richmond Field Station five years ago. It was then you inspired me to pursue a PhD degree and commit myself to research in the next five years. I am forever grateful to your support and guidance over the years.

Next I want to thank Professor Jonathan Bray, Professor Nicholas Sitar, Professor Kenichi Soga, Professor Michael Riemer and Professor Dimitrios Zekkos. Your amazing lectures take my understanding of Geotechnical Engineering to another level. I am also grateful for the advice you gave to me when I worked as a GSI.

I also want to Thank Dr. Xie Hu. Your presentation at the Geosystems Wednesday seminar four years ago introduced the InSAR technique to me for the very first time. Thank you for teaching me the basics of InSAR when I started doing research in this field.

A special thank goes to Professor Roland Bürgmann. Thank you for letting me participate in your group meeting. Many of your group members, Dr. Kang Wang, Yuexin Li and Danielle Lindsay introduced some of the latest InSAR processing techniques to me. Your professional advice pointed me to the correct direction in this field which I knew nothing about beforehand.

Finally, I would like to thank my parents and grand parents. Life was not easy during the pandemic. Your unconditional support encouraged me to stay positive and keep my research and everyday life organized.

InSAR data sets used in this thesis are from the satellites launched by Japan Aerospace Exploration Agency (JAXA) and European Space Agency (ESA). The digital elevation model (DEM) is from the Shuttle Radar Topography Mission (SRTM) by NASA. SNAP developed by ESA, ISCE developed by JPL and StaMPS developed by Professor Andy Hooper were used for InSAR processing. I thank Alaska Satellite Facility for the creation ASF Vertex that provides a free and user friendly interface to search and download InSAR data sets. Funding for this research is provided by University of California, Berkeley and Chinese Scholarship Council (CSC).

Chapter 1

Introduction

1.1 Overview

Liquefaction is one of the most important, interesting, and complex topics in geotechnical earthquake engineering [45]. Liquefaction hazards drew the attention of researchers after the Alaska ($M_w = 9.2$) and Niigata ($M_w = 7.5$) earthquakes in 1964. The generation of excess pore pressure under undrained loading conditions is a hallmark of all liquefaction phenomena. When loose cohesionless soils are saturated, rapid loading occurs under undrained conditions, so the tendency for densification causes excess pore pressures to increase and effective stresses to decrease. Liquefaction phenomena that results from this process can be divided into two main groups: flow liquefaction and cyclic mobility. In the field, flow liquefaction occurs much less frequently than cyclic mobility but its effects are usually far more severe. Cyclic mobility, on the other hand, can occur under a much broader range of soil and site conditions than flow liquefaction; its effects can range from insignificant to highly damaging [45]. Since liquefaction tends to happen at locations that liquefied in the past earthquakes, liquefaction mapping is crucial to earthquake case studies. Currently, satellite and aerial images are widely used for characterizing liquefied areas ahead of field reconnaissances. However, this method can lead to overestimation of liquefaction damage. One example was presented by Anderson et al. 2016 [1] from the 2016 Kumamoto, Japan earthquake showed that bundles and burnt rice stalks on satellite images were misidentified as sand boils by many researchers. Therefore, more accurate remote sensing techniques are needed for liquefaction characterization to provide the field reconnaissance teams with better references and potentially reduce their exposure to post seismic hazards.

Synthetic Aperture Radar (SAR) was invented in 1952 to overcome the resolution issue in along-track (azimuth) direction of existing Side-looking Airborne Radar (SLAR) technology [21, 68]. Interferometric Synthetic Aperture Radar (InSAR) has been developed into an advanced remote sensing technique since it was first introduced by Graham in 1974 [28]. The first InSAR applications to terrains date back to late 1980s [25, 76]. InSAR can reveal ground deformation to centimeter level accuracy (even millimeter level accuracy for some of the

InSAR analysis methods) by isolating the phase difference caused by ground displacements from an interferogram formed by a pair of coregistered SAR images and transforming it into displacement with the radar wavelength. The shorter return period of modern InSAR satellites, like ALOS-2 (14 days) and Sentinel-1 (12 days, 6 days if using Sentinel-1A and B at the same time), makes co-seismic InSAR analysis possible shortly after the earthquake. With an easier access to InSAR data sets with better quality and coverage, InSAR has become an excellent remote sensing technique for liquefaction mapping.

To compare the effectiveness of the different InSAR analysis methods for earthquake induced liquefaction observations, three case histories (2010~2011 Canterbury, 2016 Kumamoto and 2018 Hokkaido) were selected for this research. The selection is based on the extent of liquefaction damage and the availability of InSAR data sets. 2010-2011 Canterbury earthquake sequence contains two major earthquakes: 2010 Darfield earthquake and 2011 Christchurch earthquake. There is well documented liquefaction damage for both earthquakes. ALOS-1 (launched by JAXA) L-band data set is available for both earthquake events. Thus, the comparison between the damage in the city of Christchurch, New Zealand, from the two earthquakes is highly suitable for investigation with InSAR. The 2016 Kumamoto earthquake provides a great opportunity to compare the results from different satellites with different radar wavelength (L-band ALOS-2 and C-band Sentinel-1). The large horizontal displacements and settlements in Aso Valley caused by liquefaction fit the purpose of this research perfectly. The 2018 Hokkaido earthquake is an excellent case history to test different InSAR analysis methods with only free C-band Sentinel-1 data set because most of the documented displacements caused by liquefaction are within decimeter level. Unfortunately, this research project does not have access to the ALOS-2 data set for this case study. Two earthquakes with significant liquefaction damage: 2011 Tohoku earthquake and 2018 Palu earthquake are not a part of this research for the following reasons. Although the liquefaction damage caused by 2011 Tohoku earthquake in Urayasu City is well documented [11, 37], this research project did not have access to the ALOS-1 data set for this case and the free Envisat data set does not have coverage for Urayasu City. In the second case, the liquefaction caused displacements in the 2018 Palu earthquake are very large and chaotic due to poor ground conditions [47, 65]. As a result, the C-band Sentinel-1 data set is discorrelated and the L-band ALOS-2 data set can only reveal the displacement of the ruptured fault [16, 57, 63].

1.2 Objectives

This research aims to construct the optimum InSAR workflow for earthquake induced liquefaction analysis. It focuses on the following key objectives:

- Analyse available InSAR data sets with different methods.
- Compare the InSAR analysis results with documented field observations.

- Discuss the advantages and disadvantages of different methods.
- Construct the InSAR workflow based on different site characteristics.

1.3 Outline

The four different InSAR analysis methods used in this research: conventional differential InSAR (DInSAR), persistent scatter time-series analysis, coherence-change method and pixel (dense) offset are introduced in Chapter 2 together with the most important error correction: atmospheric phase correction.

Chapter 3, Chapter 4 and Chapter 5 cover the three case studies respectively. Each case study includes site geology, comparison between InSAR analysis results and field observations, discussion on the effectiveness of different methods.

Chapter 6 summarizes the discussion in the previous three chapters and presents the InSAR workflow for earthquake induced liquefaction analysis. Finally, based on the findings in this research and the recent InSAR research progress, future work on potential areas is discussed.

The detailed steps of the InSAR workflow presented in Chapter 6, the scripts that are used, and the steps for solving some of the common issues are included in Appendix A.

Chapter 2

Methodology

The invention of Radio Detection and Ranging, or radar, as a concept for detecting and localizing objects in a three-dimensional space dates back to the turn of 20th century. Once invented, radar technology developed rapidly during World War II era, motivated mostly by air defense and over-the-horizon surveillance considerations. By the early 1940s, radars had become small enough to be implemented on airplanes, expanding the application realm of radar systems into a range of new fields, including the growing discipline of Earth observation [21].

Synthetic Aperture Radar (SAR) was invented by Carl Wiley, an engineer with the Goodyear Aircraft Cooperation, in 1952. He discovered that a sequence of acquisitions made with a shorter antenna along the flight path of the radar sensor can create a much longer effective antenna, which can significantly increase the resolution of the radar image. Interferometric Synthetic Aperture Radar (InSAR) is a remote sensing technology developed based on the SAR sensing technique. When the radar sensor makes radar acquisitions over the same area of interest at two different times, a phase difference will generate if the microwave travels different distance to get back to the radar sensor. Such phase difference can be caused by different factors, like ground displacement, atmosphere etc. The key to InSAR is to isolate the phase difference caused by the ground displacement, which will be discussed in detail in this chapter.

2.1 InSAR analysis methods used in this research

In this section, the four InSAR analysis methods used in this research are introduced.

Differential InSAR (DInSAR)

DInSAR is a conventional InSAR analysis method. It was first introduced by Gabriel et al. in 1989 [24]. The interferometric phase ($\Delta\phi$) of an InSAR interferogram formed by two SAR acquisitions at different times over the same area contains the following components:

$$\Delta\phi = \Delta\phi_{displacement} + \Delta\phi_{geometry} + \Delta\phi_{atmosphere} + \Delta\phi_{noise} \quad (2.1)$$

- $\Delta\phi_{displacement}$: phase due to ground displacement
- $\Delta\phi_{geometry}$: geometrical phase (e.g. topography, earth curvature)
- $\Delta\phi_{atmosphere}$: atmospheric phase delay (ionospheric and tropospheric phase delay)
- $\Delta\phi_{noise}$: phase due to other noise

The phase due to ground displacement $\Delta\phi_{displacement}$ here is a modulo of 2π , which is called the wrapped phase. It needs to be unwrapped before being used to reveal the ground displacement. Goldstein et al. first discussed two-dimensional phase unwrapping in 1988 [26]. The widely used Statistical-cost, Network-flow Algorithm for Phase Unwrapping (SNAPHU) today was proposed and implemented by Chen and Zebker in the early 2000s [8, 9, 10]. Because the radar beam starts from the satellite, bounces back on the ground and then travels back to the satellite, one radar wavelength of displacement on the ground in the line-of-sight (LOS) direction is equivalent to 4π of phase change which is represented by two-cycle of color fringes on the interferogram.

To isolate $\Delta\phi_{displacement}$, other phase components need to be estimated and subtracted from interferometric phase $\Delta\phi$. The geometrical phase $\Delta\phi_{geometry}$ can be estimated with the digital elevation model (DEM) from SRTM and the precise orbit data of the satellite. The methods to correct $\Delta\phi_{atmosphere}$ are introduced in Section 2.2. The phase due to noise $\Delta\phi_{noise}$ is considered as irreducible error. Whether it is reasonable to ignore $\Delta\phi_{noise}$ depends on the requirements of the project.

Data sets from two different SAR acquisition modes are used in this research: stripmap mode and TOPS mode. In conventional stripmap mode, the radar antenna is fixed to a specific direction, illuminating a single swath of the scene with a fixed squint angle (the angle between radar beam and the cross-track direction). The stripmap mode has been used by several SAR missions: Envisat, ERS, ALOS-1, TerraSAR-X etc. TOPS stands for Terrain Observation with Progressive Scans. In TOPS mode, the radar sensor steers the antenna from a backward along-track direction to a forward along-track direction for a subswath. After a successful scan at this subswath, the antenna is rolled back to its initial position and pointed to a new subswath to increase coverage. After the same scan process is done for three subswaths, the entire scanning process is repeated. Each scan at a subswath is called a "burst". Within each subswath, there is a small overlap between successive bursts to ensure continuous coverage. The Sentinel-1 launched by ESA in 2014 is a typical SAR mission in TOPS mode. The SAR data sets used in this research are summarized in Table 2.1.

The DInSAR analysis of this research was performed in the InSAR Scientific Computing Environment (ISCE) created by Rosen et al. [53, 52, 54].

¹The operating acquisition mode of ALOS-2 is ScanSAR. But it is acquiring stripmap data in certain areas. The ALOS-2 data set used in this research was acquired in stripmap mode.

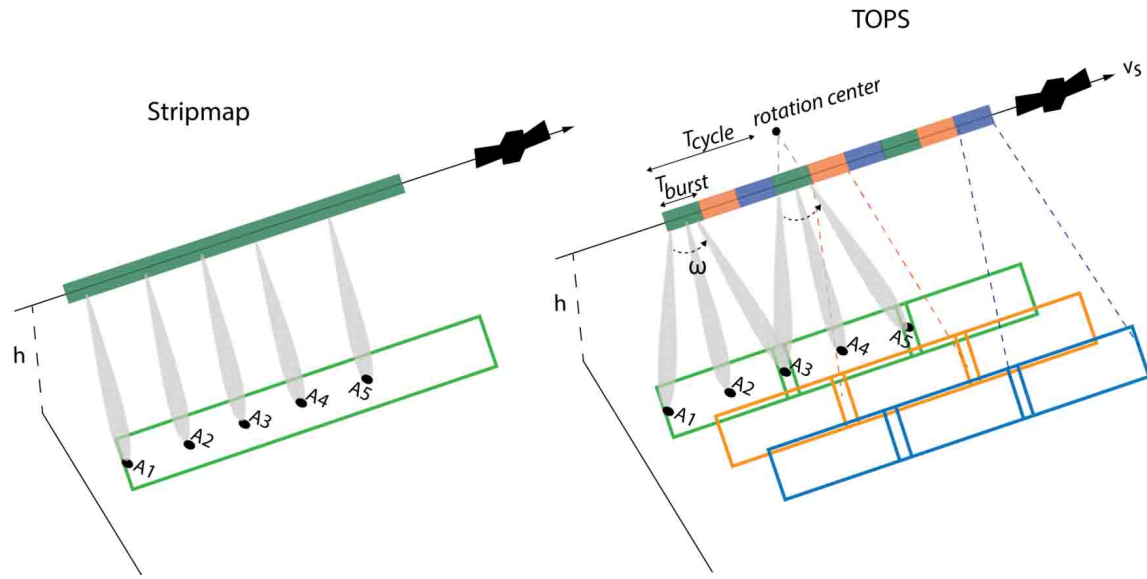


Figure 2.1: Stripmap and TOPS acquisition mode [17]

| Name | Time | Acquisition mode | Radar band | Wavelength (cm) |
|------------|-----------------|---------------------------------|------------|-----------------|
| ALOS-1 | 2006 to 2011 | stripmap | L-band | 22.9 |
| Sentinel-1 | 2014 to present | TOPS | C-band | 5.6 |
| ALOS-2 | 2014 to present | ScanSAR ¹ , stripmap | L-band | 22.9 |

Table 2.1: SAR data sets used in this research

Persistent Scatterer, time-series Analysis (PSInSAR)

Persistent Scatterer InSAR is an extension to the conventional InSAR techniques (DInSAR), which addresses the problems of decorrelation and atmospheric delay [34]. The first PS algorithm was created by Ferretti et al. [18, 19]. The strategy to select PS candidates of this algorithm is based on the amplitude dispersion D_A :

$$D_A = \frac{\sigma_A}{m_A} \quad (2.2)$$

where σ_A and m_A are the standard deviation and mean of the amplitude value [19]. Similar algorithms were developed by Crosetto et al. [12], Lyons and Sandwell [46], Werner et al. [67] and Kampes [39] afterwards. These algorithms are very successful for InSAR analysis in scenes with sufficient number of man-made structures, which provide efficient reflectors that dominate background scattering. These algorithms also require approximate knowledge of temporal deformation change to identify PS pixels. Therefore, when this information is not available (for example, volcanoes), these algorithms are not usable [34].

To solve those problems, Hooper [31, 32, 33] proposed a new PS analysis method, named as StaMPS (Stanford Method for Persistent Scatterers). StaMPS uses spatial correlation of phase measurements to identify PS pixels. Thus, it is applicable in areas that undergo non-steady deformation with prior knowledge on temporal deformation variations. StaMPS is capable of identifying decent density of PS pixels in mountainous areas. This is the main reason StaMPS was selected in this research to perform PSInSAR analysis for the two Japan case studies.

The preprocessing of the Sentinel-1 data sets for PSInSAR analysis was performed in Sentinel Application Platform (SNAP). Snap2stamps, a python package implemented by Foumelis et al. [22], was used to convert the products from SNAP into the format that is readable by StaMPS.

Coherence-change method

Damage caused by earthquake can be chaotic (e.g. flow liquefaction). As a result, the co-seismic interferogram might be decorrelated which makes phase unwrapping impossible. Coherence is a measure of the similarity between two SAR scenes that form the interferogram. Its decrease is a viable proxy for identifying earthquake damage.

Kobayashi et al. [43] used this method to identify liquefied areas in 2011 Tohoku earthquake and found good correlation between liquefaction and coherence decrease. Tamura and El-Gharbawi [61] used coherence change to detect urban damage in Ishinomaki City caused by 2011 Tohoku earthquake and subsequent tsunami. Watanabe et al. [64] used coherence-change technique with coherence filter and polarization to detect damaged urban areas by the 2015 Gorkha earthquake and successfully increased the accuracy. Fielding et al. [20] used InSAR coherence and coherence change to map the surface disruptions due to fault ruptures reaching the surface.

In this research, coherence-change method was used as a complimentary method to identify liquefied areas with large displacement. Normalized coherence change ($\Delta\gamma$) is calculated with Equation 2.3:

$$\Delta\gamma = \frac{\gamma_{pre} - \gamma_{co}}{\gamma_{pre} + \gamma_{co}} \quad (2.3)$$

where γ_{pre} is the coherence of an interferogram before the earthquake and γ_{co} is the coherence of the co-seismic interferogram.

Pixel offset method

The mathematical theory behind Pixel offset method is 2D cross-correlation. A given template patch extracted from the secondary SAR scene is slid across the reference SAR scene to find the location with the highest 2D cross-correlation. And then the displacement of this patch is measured with number of pixels in the range and azimuth direction. This process is shown in Figure 2.2. The template patch was slid over the reference SAR scene at 9 discrete locations. The peak correlation is at the location with index (1, 1). A dense offset map can

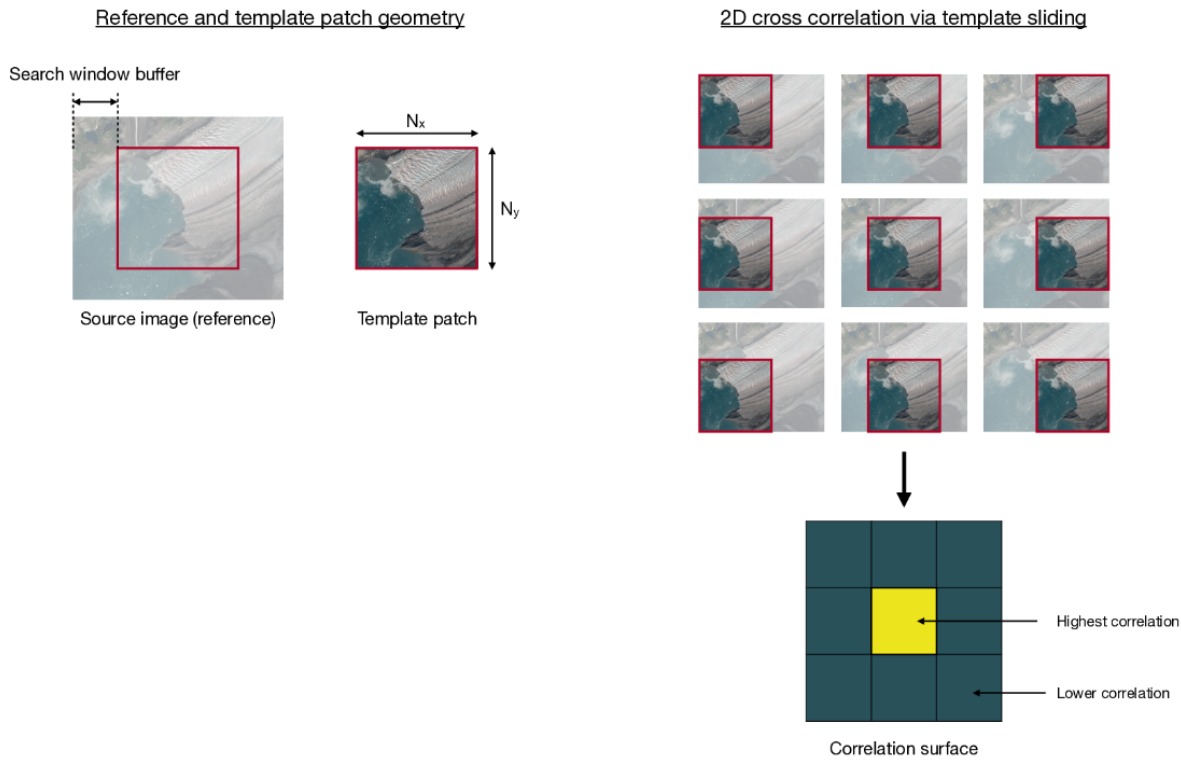


Figure 2.2: Schematic illustration of the pixel offset method (credit to the Jupyter notebook created by Bryan Riel and Brent Minchew from MIT).

be created by repeating this process for a dense array of patches from the secondary SAR scenes.

Pixel offset method is useful when the displacement between two SAR acquisitions is large enough to cause complete decorrelation on the interferogram. Singleton et al. [56], Sun and Muller [58] evaluated this method for monitoring landslides in vegetated terrains. Riel et al. [50] applied this method to glacier movement tracking. Earthquake-induced displacement also satisfies the characteristics of large displacement in a short period of time. In this research, pixel offset method was used when InSAR analysis cannot reveal the amount of displacement observed in field.

The pixel offset analysis was performed within the InSAR Scientific Computing Environment (ISCE) [53, 52, 54] in this research.

2.2 Atmospheric phase correction

Ionospheric phase delay

Ionospheric phase delay is caused by the Total Electron Content (TEC) gradients in the azimuth direction, which introduces extra azimuth offsets between two SAR scenes. These extra azimuth offsets will increase the phase delay. The dispersive property of ionospheric phase delay makes it possible to be separated from other non-dispersive phase components from Equation 2.1. It is a prevalent issue for L-band satellites like ALOS-1.

The widely used method to estimate ionospheric phase delay today is split spectrum method [17, 27, 66]. The interferograms at two different frequencies (one high band f_H and one low band f_L) are required for this method. After phase unwrapping, the interferometric phase of the two interferograms: The parameters $\Delta\phi_H$ and $\Delta\phi_L$ are used to estimate the dispersive ionospheric phase and the non-dispersive other phase components with the following equations:

$$\begin{aligned}\hat{\Delta\phi}_{iono} &= \frac{f_L f_H}{f_0(f_H^2 - f_L^2)} (\Delta\phi_L f_H - \Delta\phi_H f_L) \\ \hat{\Delta\phi}_{non-disp} &= \frac{f_0}{(f_H^2 - f_L^2)} (\Delta\phi_H f_H - \Delta\phi_L f_L)\end{aligned}\tag{2.4}$$

where $\hat{\Delta\phi}_{iono}$ is the estimated ionospheric phase delay.

Tropospheric phase delay

Tropospheric phase delay is caused by the spatial and temporal variations of tropospheric water vapor. There are two kinds of methods for estimating tropospheric phase delay: methods without external information (stacking, filtering) and methods using independent data (GPS, weather models etc.).

The Generic Atmospheric Correction Online Service for InSAR (GACOS) was used for tropospheric phase delay in this research. It utilises the Iterative Tropospheric Decomposition (ITD) model [73] to separate stratified and turbulent signals from tropospheric total delays, and generate high spatial resolution zenith total delay maps to be used for correcting InSAR measurements and other applications [72, 74].

GACOS has the advantage of global coverage and real time on-demand service. That is why GACOS was selected over the other methods for this research.

Chapter 3

Canterbury Earthquake Sequence Case Study

3.1 Introduction

On September 4th 2010, Darfield earthquake ($M_W = 7.1$) struck the Canterbury region of New Zealand. The epicenter was located about 40 km west of the Central Business District (CBD) of Christchurch at a depth of about 10 km. Extensive damage was inflicted to lifelines and residential houses due to widespread liquefaction and lateral spreading in areas close to major streams, rivers and wetlands throughout Christchurch and Kaiapoi [29]. Five months later, on February 22nd 2011, Christchurch earthquake ($M_w = 6.3$), the most costly earthquake to affect New Zealand, struck the same area. The epicenter was near Lyttelton, only 6 km to the southeast of the Christchurch CBD at a depth of 5 km. Despite the smaller moment magnitude, 2011 Christchurch earthquake caused more damage to pipeline networks, transport facilities, residential houses/properties and multistory buildings in the CBD than the 2010 Darfield earthquake, mainly due to the epicenter closer to the city and at a shallower depth [49]. This provided a rare opportunity to learn how the same ground and infrastructure responded to two significant earthquakes [14] fewer than six months apart.

3.2 Local Geology

The Canterbury Plains is the largest low-lying farm area of New Zealand, formed by complex overlapping fans of glacier-fed rivers originating from the Southern Alps. Most soils are derived from greywacke or loess. Weathered volcanic rock (Basalt) and thick deposits of Pleistocene loess are present on the slopes of the Port Hills of Banks Peninsula, the eroded remnant of the extinct Lyttelton Volcano [49].

The city of Christchurch is located on the east coast of the Canterbury Plains adjacent to the Banks Peninsula. Most of the city was mainly a swamp behind coastal sand dunes, and estuaries and lagoons that have now been drained [5]. The surface geology of the greater

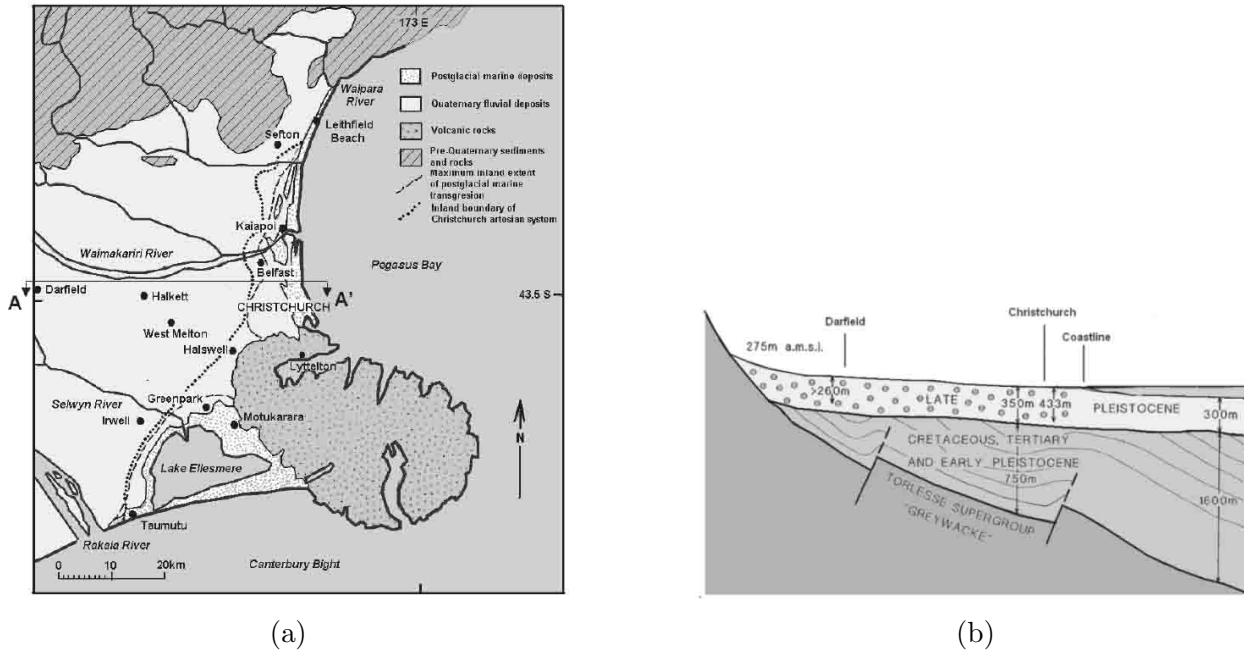


Figure 3.1: (a) Simplified Christchurch geology map [49]. (b) Simplified soil profile along cross section A-A' [6, 49].

Christchurch area consists of predominantly recent Holocene (<11,700 years old) alluvial gravel, sand, and silt of the Springston Formation, while Christchurch Formation sediments have been mapped along the eastern margin of the city [6]. The Springston Formation, with maximum thickness of 20 m to the west of Christchurch, consists of river flood channels. It contains alluvial gravel as the main component, and overbank deposits of sand and silt that are susceptible to liquefaction. The Christchurch Formation, with maximum thickness of 40 m at the coast of New Brighton, contains fixed and semi-fixed dunes and beach sands, which are generally denser and less prone to liquefaction. 300-400 meters of Riccarton Gravel Formation lies underneath these two formations. The bedrock is generally hundreds of meters deep. The simplified geology map and soil profile of Christchurch are shown in Figure 3.1.

3.3 InSAR analysis results compared to field observations

Faults ruptured in the two earthquakes

A previously unidentified right lateral strike-slip fault, the Greendale fault, ruptured in the 2010 Darfield earthquake. Offsets and fracture patterns reveal up to 4.6 meters of displacement, with an average displacement of ~ 2.3 m across the entire rupture. Vertical

| Satellite | Time | Flight Direction | Path | Frame | Wavelength (cm) |
|-----------|------------|------------------|------|-------|-----------------|
| ALOS-1 | 03/11/2010 | Ascending | 336 | 6300 | 22.9 |
| ALOS-1 | 09/11/2010 | Ascending | 336 | 6300 | 22.9 |
| ALOS-1 | 08/13/2010 | Ascending | 337 | 6290 | 22.9 |
| ALOS-1 | 09/28/2010 | Ascending | 337 | 6290 | 22.9 |
| ALOS-1 | 10/27/2010 | Ascending | 336 | 6300 | 22.9 |
| ALOS-1 | 03/14/2011 | Ascending | 336 | 6300 | 22.9 |

Table 3.1: SAR data sets used in the Canterbury earthquake sequence case study

offsets of up to ~ 1 m occur at constraining or releasing bends [29]. The 2011 Christchurch earthquake occurred on an unmapped fault located beneath the Port Hills of the northern Banks Peninsula. GNS modeled the fault plane as a rectangle, dipping 65 degrees southeast, and extending from ~ 6 km depth to ~ 1 km depth. GPS data indicates that the Port Hills were uplifted by about 15~45 cm, while the Christchurch area north of the projection of the fault subsided by about 5~15 cm [14]. Figure 3.2 shows the InSAR analysis results of the co-seismic pair in the two earthquakes. The InSAR data set used in this case study is summarized in Table 3.1.

The maximum relative displacement in the LOS direction of Greendale fault is approximately 3.4 m as shown in Figure 3.3. The 4.6 m displacement mentioned previously in this chapter is equivalent to 2.9 m in the LOS direction. Vertical offset of up to 1 m at constraining or releasing bends can also contribute up to 0.77 m in the LOS direction. Therefore, in reality, the maximum relative displacement in the LOS direction is up to 3.67 m. This upper limit may never be reached because the maximum horizontal and vertical offsets might not occur at the same location. So, the InSAR result is consistent with field observation.

The 15~45 cm uplift of Port Hills and the 5~15 cm subsidence of Christchurch north of the fault are equivalent to 11.6~34.7 cm towards the satellite and 3.9~11.6 cm away from the satellite in the LOS direction respectively. Considering the contribution from horizontal displacement caused by tectonic movement and extensive lateral spreading due to liquefaction in this region, the -23.3~63.7 cm range from InSAR analysis is reasonable.

Liquefaction near Avon River

Both earthquakes caused extensive liquefaction in Christchurch area. The shallower depth and the closer distance to the city of the 2011 event resulted in more significant and widespread liquefaction damage in this area than the 2010 event. First of all, it is important to compare the liquefaction map with the InSAR co-seismic pair analysis results to determine whether the InSAR results can reveal the liquefaction damaged zones. The LOS displacements maps from InSAR analysis are shown in Figure 3.4. The liquefaction map overlays are shown in Figure 3.5. These liquefaction maps are cited from Orense et al. 2011 [49]. In general, the liquefaction maps agree quite well with the InSAR analysis results

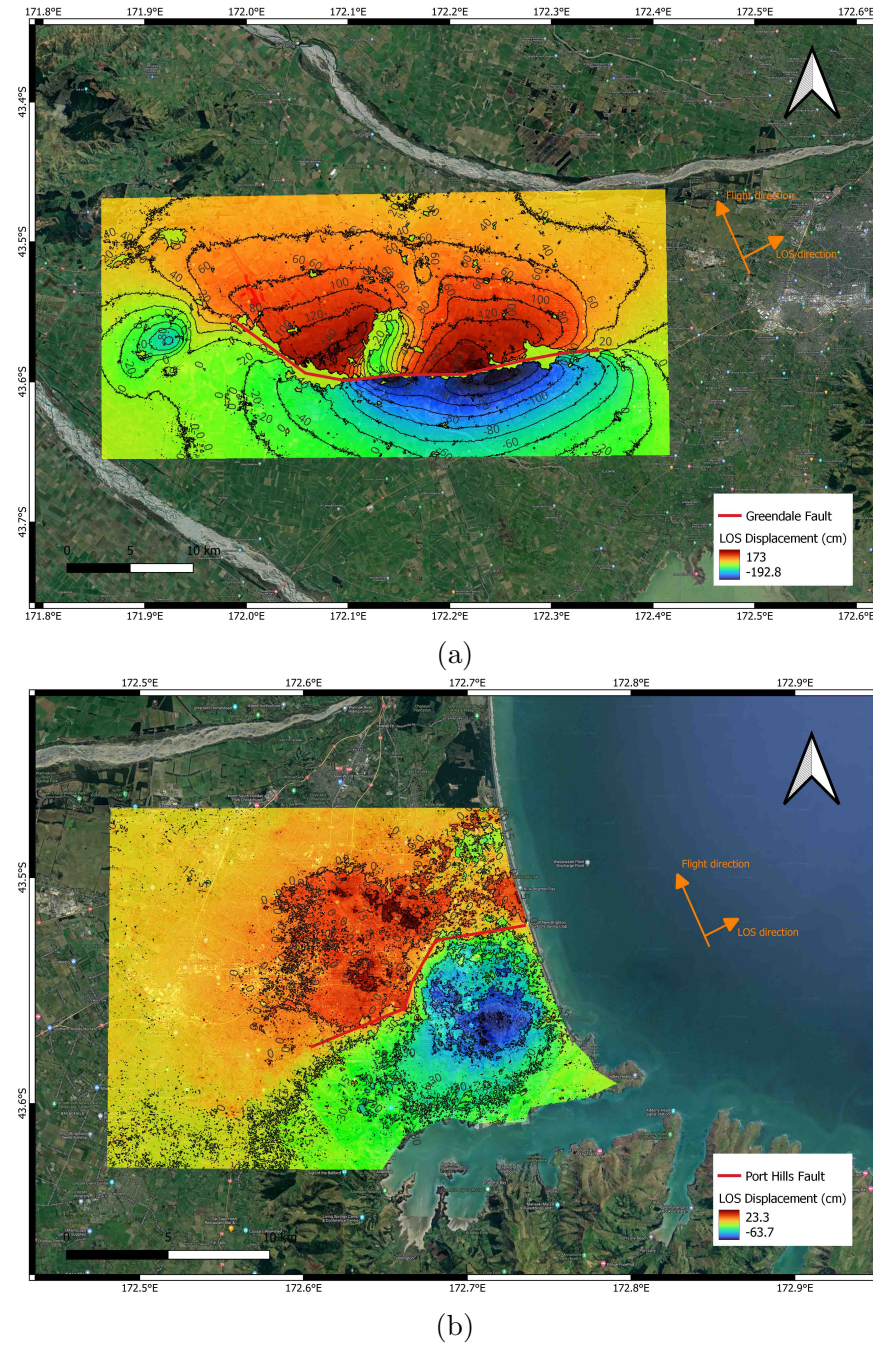


Figure 3.2: (a) Greendale fault (2010 Darfield earthquake), co-seismic pair between scenes from 03/11/2010 and 09/11/2010, positive displacement is moving away from the satellite in the LOS direction. (b) Port Hills fault (2011 Christchurch earthquake), co-seismic pair between scenes from 10/27/2010 and 03/14/2011, positive displacement is moving away from the satellite in the LOS direction.

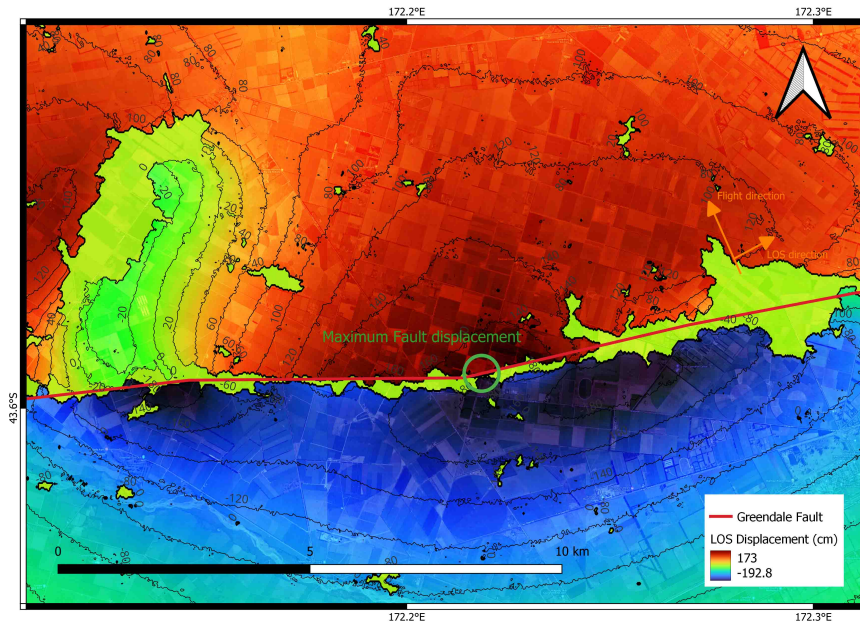


Figure 3.3: Maximum relative fault displacement in the LOS direction is ~ 3.4 m in the green circle. The light green zone near fault trace is due to the decorrelation caused by fault rupture.

for two reasons: (1) The LOS displacement shows concentration along the Avon River for the 2010 event while the LOS displacement from the 2011 event is scattered over a much wider area; and (2) The No liquefaction zone on the map coincides with the areas that have noticeable smaller LOS displacement than the surrounding areas. Therefore, the InSAR co-seismic analysis results with ALOS-1 data sets can reveal the liquefaction damaged areas in Christchurch.

Next, with the well-documented permanent lateral ground displacement caused by lateral spreading by Cubrinovski et al. 2012 [13], it is interesting to compare the field measurements with the LOS displacement along the Avon River from the InSAR analysis. The field measurements are projected to the LOS direction with the assumption that there is no vertical offset and the lateral spreading on both banks are moving towards the river. According to the preliminary model of the fault ruptured in the 2011 Christchurch earthquake in Figure 3.16, the tectonic displacement along the Avon River caused by the 2011 event ranges from 15 cm of settlement to 25 cm of uplift and the tectonic displacement is not uniform along the Avon River. Since this is only a preliminary model, it is not possible to remove the tectonic displacement accurately. Therefore, only the 2010 event is usable for this comparison. The measured permanent lateral ground displacements induced by lateral spreading at the banks after the 2010 Darfield earthquake from the field reconnaissance are summarized in Table 3.2 [13]. The locations with significant lateral spreading along the Avon River in the 2010 Darfield earthquake according to Cubrinovski et al. 2012 [13] are labeled in Figure

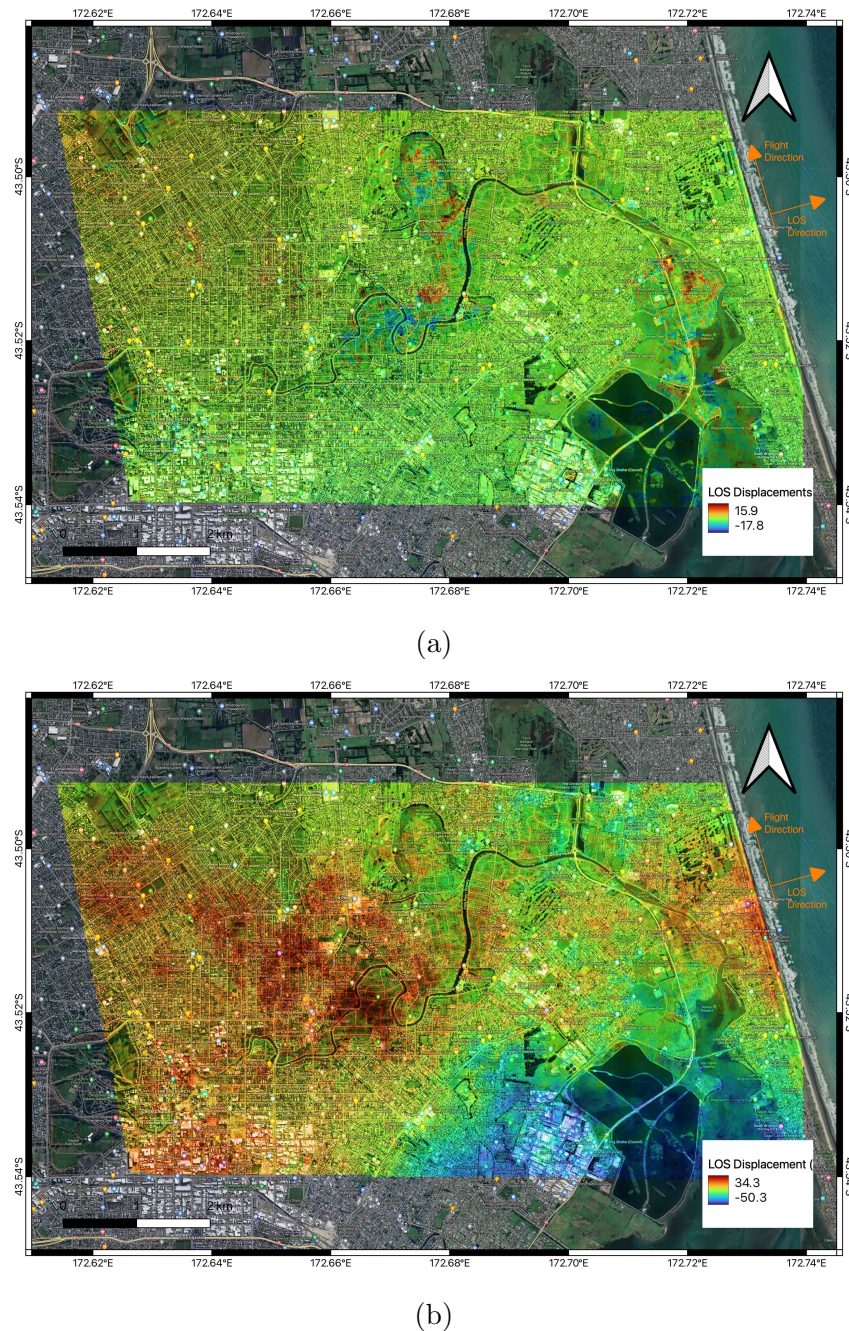


Figure 3.4: (a) 2010 Darfield earthquake LOS displacements (b) 2011 Christchurch earthquake LOS displacements

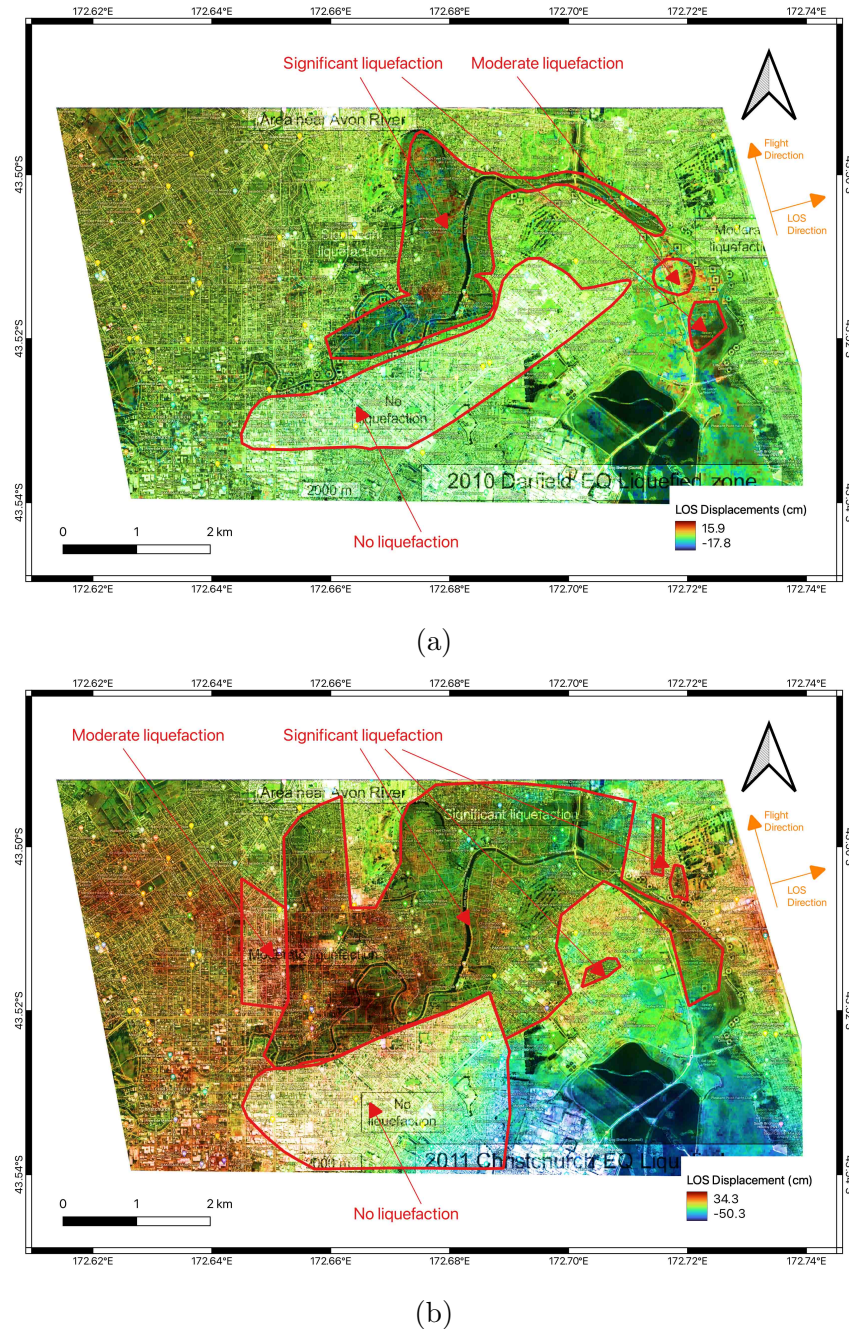


Figure 3.5: (a) 2010 Darfield earthquake liquefaction map overlay (b) 2011 Christchurch earthquake liquefaction map overlay

| Location | Permanent lateral ground displacement (m) |
|--------------------------------|--|
| South Kaiapoi | 0.5-3.5 |
| North Kaiapoi | 0.2-3.1 |
| Spencerville | 0.6-1.5 |
| Bexley | 0.3-0.9 |
| Burwood | 0.1-0.9 |
| Darlington, Avonside, Avondale | 0.5-1.8 |

Table 3.2: Range of measured permanent lateral ground displacements induced by lateral spreading at or near the waterway after the 2010 Darfield earthquake [13]

3.6. Before doing calculations, it is important to check whether the InSAR results make sense. As shown in Figure 3.6, the LOS displacement along N-S flowing river sections is larger than that of the E-W flowing river sections. This is consistent with one of InSAR's characteristics: low sensitivity to displacement in the azimuth direction because the lateral spreading displacements along E-W river sections are in the N-S direction, which is close to the azimuth direction. The theoretical minimum and maximum LOS displacement converted from the field measurements in Table 3.2 assuming no vertical displacement and the LOS displacement from InSAR analysis for both banks of the Avon River from Avonside to Bexley are plotted in Figure 3.7. As shown in Figure 3.7, the InSAR LOS displacements generally do not sit within the range of the theoretical LOS displacement converted from the field measurements. This is probably because InSAR has a hard time resolving meter-level displacement on river banks, which are extremely small areas compared to the fault rupture zone mentioned previously in this chapter. The accurate phase unwrapping is impossible for these areas because the color fringes on the interferogram are compressed together. This issue will be discussed further in Chapter 4. One way to evaluate the quality of the interferogram is to check the coherence. The coherence in the areas along the Avon River for the 2010 Darfield earthquake co-seismic pair is generally ~ 0.3 , which is too low for reliable phase unwrapping. The occasional sign inconsistency between the theoretical results and the InSAR results is likely due to the vertical offsets that are ignored by assumption and some other noise. So, Differential InSAR analysis is not suitable for extracting meter-level lateral ground displacement induced by lateral spreading on river banks but it can be used as an indication of whether lateral spreading occurs along the river.

Liquefaction in Kaiapoi

Kaiapoi was one of the worst hit locations by the 2010 Darfield earthquake. This small town sits on the banks of the Kaiapoi River, that was once a branch of the Waimakariri River. This area has experienced liquefaction during past events and has been identified as highly susceptible to liquefaction [69]. Wotherspoon et al. 2012 discusses the correlation between former channels of the Waimakariri River and the areas having significant lique-

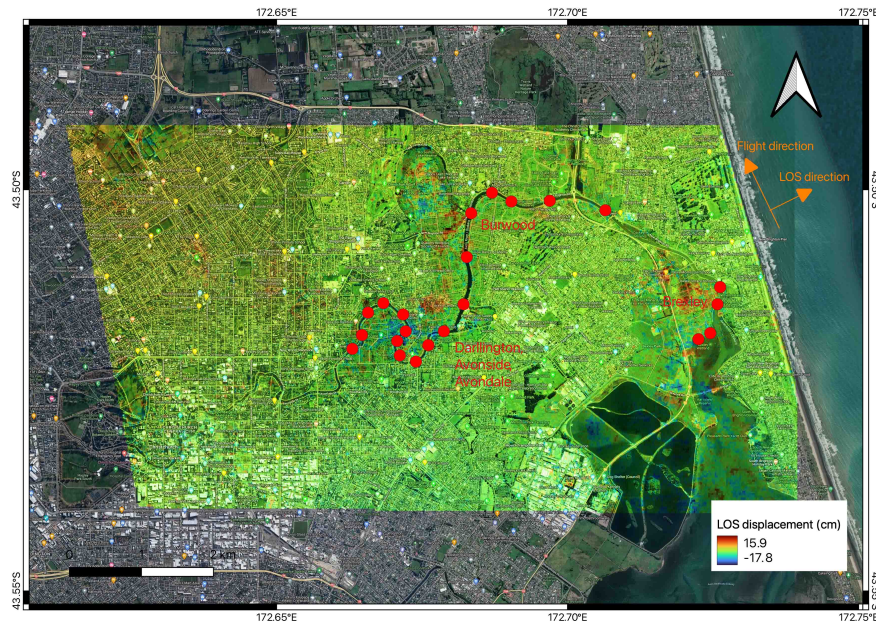


Figure 3.6: Locations with significant lateral spreading along Avon River in the 2010 Darfield earthquake [13].

faction damage following the 2010 Darfield earthquake [69] and gives a liquefaction map of Kaiapoi. Following the 2011 Christchurch earthquake, re-liquefaction occurred in Kaiapoi, but the impact of liquefaction was minor compared to the 2010 event due to farther epicentral distance [49]. The liquefaction map from Wotherspoon et al. 2012 [69] was overlain on the InSAR analysis results of both earthquakes and is shown in Figure 3.8. The areas with large LOS displacements coincide well with the liquefied zone for both earthquakes. This confirms that the InSAR results can reveal the liquefaction damage and re-liquefaction that occurred in the 2011 event. The south-western Kaiapoi showed no sign of liquefaction on the map and Kaiapoi is relatively far from the fault rupture for both events. Therefore, the InSAR analysis results for both events were referenced to this area.

Because the liquefaction damage in Kaiapoi is well-documented for the 2010 Darfield earthquake in Cubrinovski et al. 2012 [13], Wotherspoon et al. 2012 [69] and Robinson et al. 2011 [51], the InSAR results can be compared with these documented liquefaction damages. The locations where lateral ground movement due to lateral spreading were measured by Cubrinovski et al. 2012 [13] are overlaid on the InSAR results in Figure 3.9. The LOS displacements referenced to the points on the red lines (Field measurements of lateral ground movement were performed along those red lines.) that are farthest from the stream or river from Figure 3.9 are converted back into the lateral ground displacements in the red lines' direction assuming there is no vertical offset. The results are summarized in Figure 3.10. Compared to the 0.5-3.5 m and 0.2-3.1 m measured permanent lateral ground displacement in South Kaiapoi and North Kaiapoi in Table 3.2, the InSAR results are still not capable of

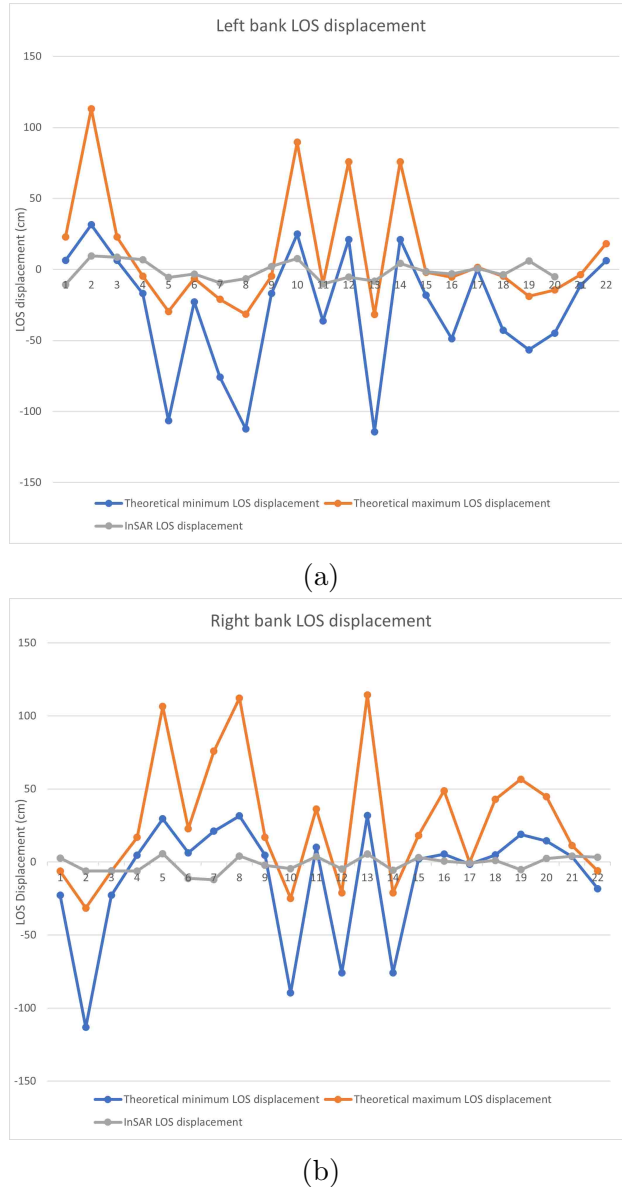


Figure 3.7: (a) Avon River left bank LOS displacement (b) Avon River right bank LOS displacement (The locations of these data points are marked from west to east along the Avon River in Figure 3.6). The theoretical minimum and maximum LOS displacements on both banks of the Avon River are converted from the field measurement in Table 3.2 assuming no vertical displacement.

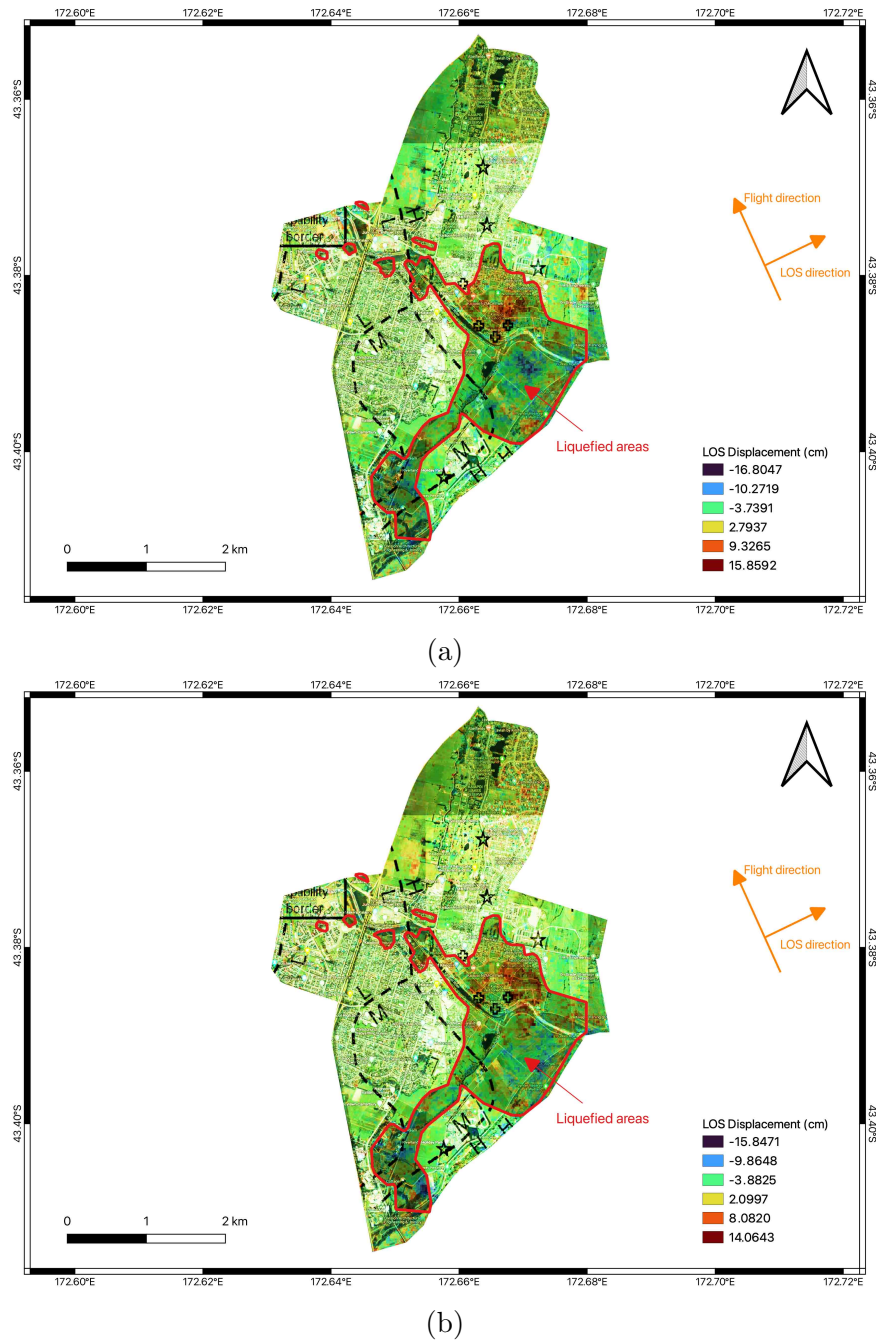


Figure 3.8: (a) 2010 Darfield earthquake liquefaction map overlay in Kaiapoi (b) 2011 Christchurch earthquake liquefaction map overlay in Kaiapoi [69]

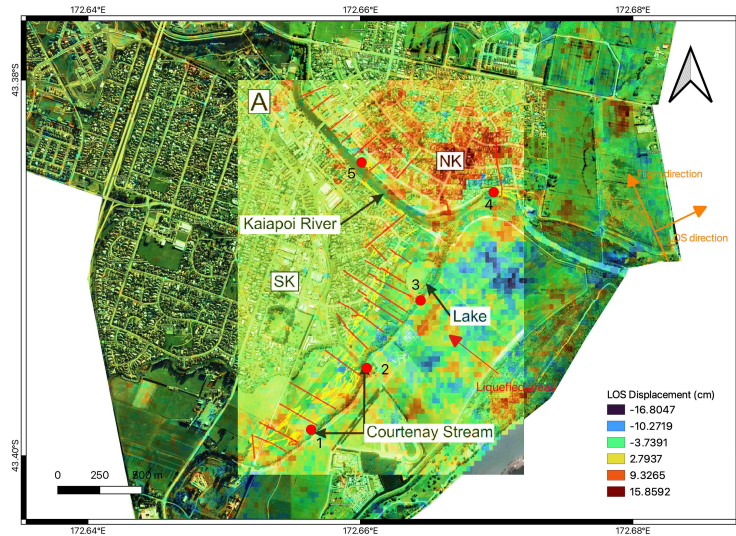


Figure 3.9: Lateral spreading in Kaiapoi following the 2010 Darfield earthquake. The red lines indicate where Cubrinovski et al. 2012 [13] measured lateral ground movement.

showing the meter-level lateral spreading displacement on river and stream banks in Kaiapoi just like the case along the Avon River.

Next, other liquefaction damage in different parts of Kaiapoi is compared to the InSAR results. In central Kaiapoi, the residential and commercial properties along Charles St and back to Cass St were damaged due to liquefaction induced settlement and ground cracking, with settlements of up to 400 mm [69]. The InSAR result for this area is shown in Figure 3.11. The residential and commercial buildings were removed, and the land was turned into parks. The red patches in Figure 3.11 represent 5.5-14.2 cm of LOS displacement moving away from the satellite, which can be converted into 7.1-18.4 cm of settlement assuming no lateral displacement. In western Kaiapoi, Wylie Park experienced widespread liquefaction with large areas of sand boils. In Murphy Park, on the other side of the river, there was a large volume of ejecta. The residential area south of the Murphy Park had the most severe liquefaction damage in the region [69]. The InSAR result for this area is shown in Figure 3.12. The blue patches in Murphy Park in Figure 3.12 represent about 5 cm of LOS displacement moving towards the satellite, which might be due to the large volume of ejecta there. The residential area south of the Murphy Park was removed and turned into a park. The red patches here represent 3.3-9.4 cm of LOS displacement moving away from the satellite, which indicates 4.3-12.2 cm of settlement in this area assuming no lateral displacement. In eastern Kaiapoi, the region north of the Kaiapoi river bend was the one the hardest hit due to liquefaction in the 2010 Darfield earthquake and many of the houses in these areas settled as a result of the liquefaction. The InSAR result for this area is shown in Figure 3.13. The residential buildings in this area were all removed and the land was turned into parks. The red patches in Figure 3.13 represent 3.6-15.8 cm of LOS displacement moving away from the

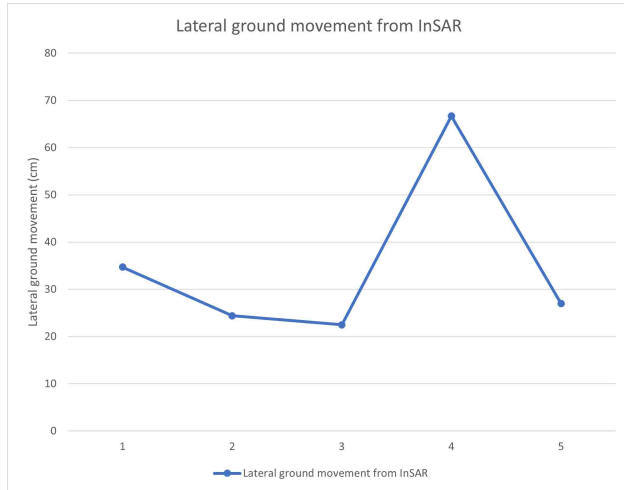


Figure 3.10: Converted lateral ground movement (in the direction perpendicular to the rivers or streams on the bank where lateral ground movement was measured in the field assuming no vertical displacement) from InSAR results (The locations of these data points are marked in Figure 3.9)

satellite, which indicates that the 4.7-20.5 cm settlement was caused by liquefaction in this region assuming no lateral displacement.

Liquefaction near Heathcote River

Heathcote River is located at the southern boundary of Christchurch. After the 2010 Darfield earthquake, there was very little evidence of ground distortion or liquefaction in this area, with only a few sand boils found [29]. However, after the 2011 Christchurch earthquake, significant ground distortions due to liquefaction were observed adjacent to Heathcote River [49]. The InSAR results near Heathcote River with the liquefaction map overlain on the 2011 event are shown in Figure 3.14. The impact of these two earthquakes shows huge difference in Figure 3.14 judging by the scale of the LOS displacement from the co-seismic interferograms of the two events. The areas with liquefaction damage near Heathcote river following the 2011 event are way more limited compared the liquefaction damaged areas near Avon River (Figure 3.5b) and there is no indication of lateral spreading (like the LOS displacement pattern along the Avon River in Figure 3.5b) along the Heathcote River as shown in Figure 3.14 (b).

The lower area along Wilson Road in St. Martins was one of the worst-hit liquefaction areas near Heathcote River [49]. The InSAR result for this area is shown in Figure 3.15. One thing to be cautious about when analyzing InSAR results in Christchurch following the 2011 Christchurch earthquake is removing tectonic displacement caused by fault rupture. The tectonic displacement in this area can be estimated with the preliminary fault model created

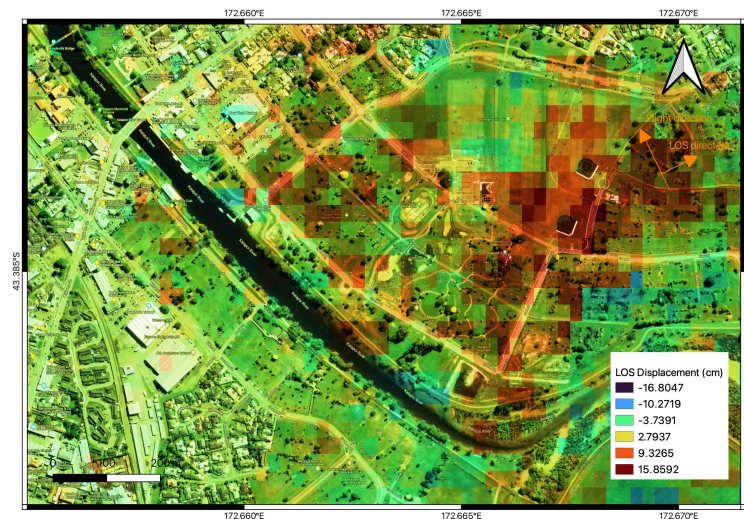


Figure 3.11: InSAR result in Kaiapoi along Charles St following the 2010 Darfield earthquake. (The google earth map is from 2022.) Red zones indicate 7.1-18.4 cm settlement caused by liquefaction.



Figure 3.12: InSAR result in western Kaiapoi following the 2010 Darfield earthquake. (The google earth map is from 2022.) The red zone south of Murphy park indicates 4.3-12.2 cm settlement caused by liquefaction.

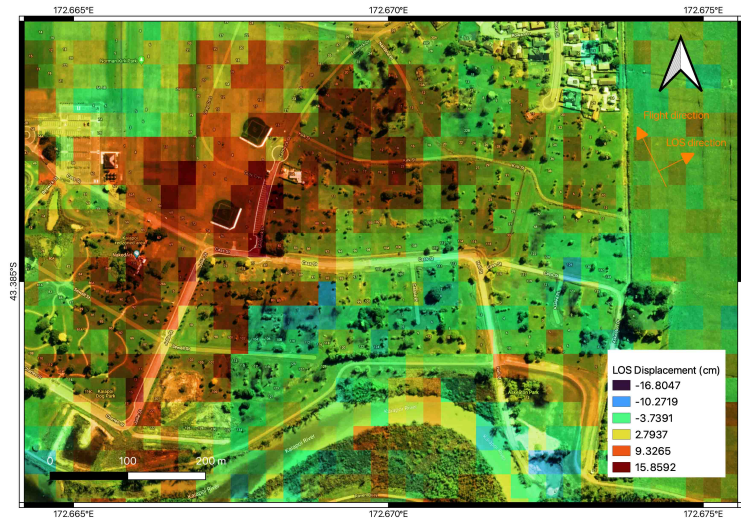


Figure 3.13: InSAR result in eastern Kaiapoi following the 2010 Darfield earthquake. (The google earth map is from 2022.) The red zone indicates 4.7-20.5 cm settlement caused by liquefaction.

by GNS as shown in Figure 3.16. The tectonic displacement in St. Martins was about 5 cm of settlement according to the fault slip model. After removing this tectonic settlement, the LOS displacement in Figure 3.15 ranges from 10.2 cm towards the satellite to 12.3 cm away from the satellite, which can be converted to 13.2 cm of ground uplift and 16 cm of ground settlement assuming no lateral displacement. Thus, the existence of ground distortions and differential settlement indicates significant liquefaction damage in this region.

Liquefaction in Christchurch CBD

As shown in Figure 3.17, the difference in damage caused by the two earthquakes in the CBD is significant judging by the scale of the LOS displacement. The key field observations made following the 2011 Christchurch earthquake regarding the effects of soil liquefaction on building performance in the CBD were summarized by Cubrinovski et al. 2011 [15]. This is an excellent case to test whether InSAR analysis is capable of revealing the differential settlement of buildings caused by liquefaction. Two case histories were taken from Cubrinovski et al. 2011 [15] to compare with the InSAR result in this case study.

The first case history is a mini-complex of three nearly identical apartment buildings and three nearly identical duplex homes built across an EW-trending geomorphic feature (Figure 3.18). This geomorphic feature is expressed here by a significant change in grade of the pavement between the northern and the middle buildings. The northern apartment building showed no evidence of cracking or distortion of the pavement surface. However, large sediment ejecta was found along the perimeter of the southern apartment building indicating

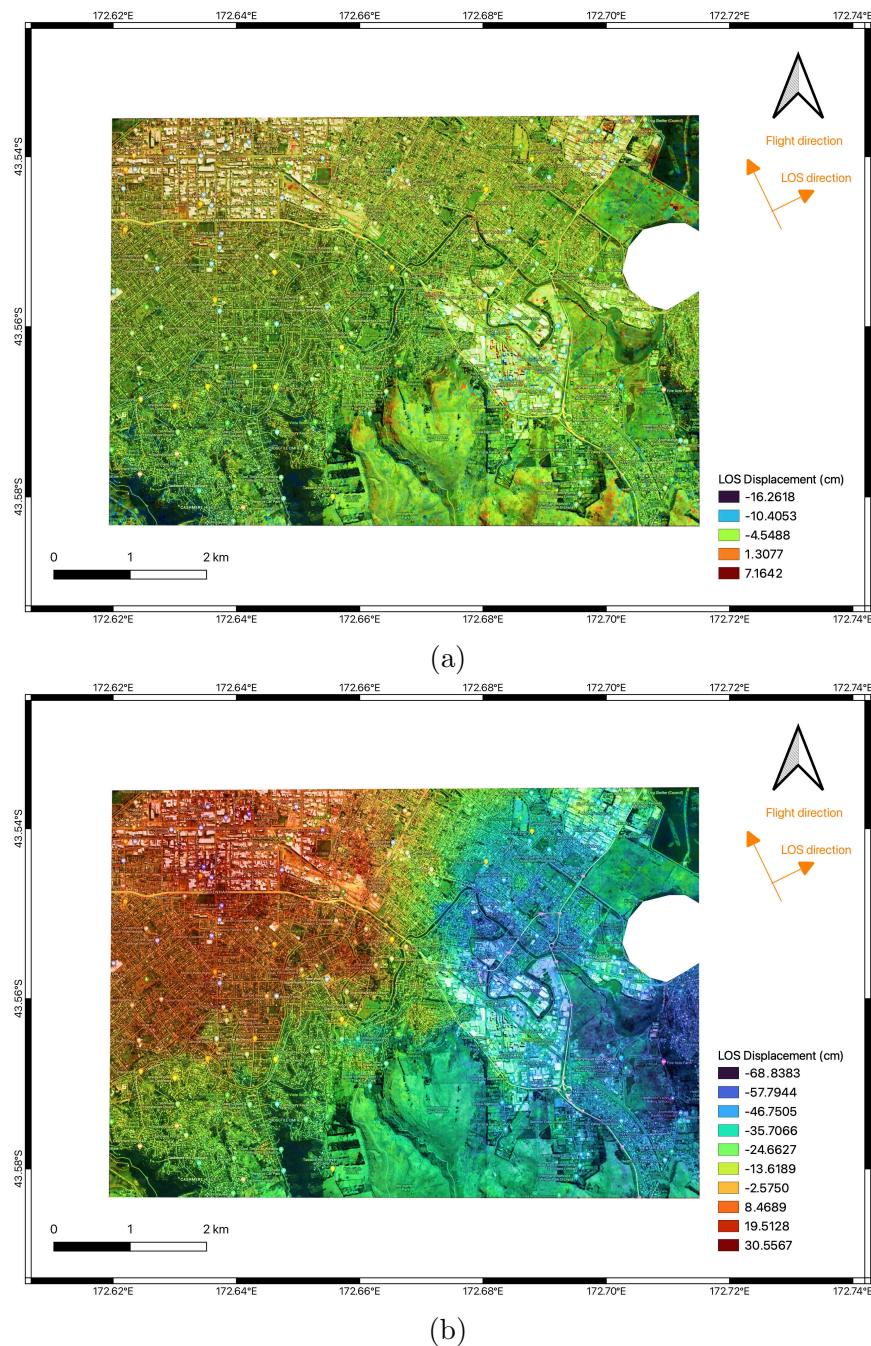


Figure 3.14: (a) 2010 Darfield earthquake liquefaction map overlay near Heathcote River (b) 2011 Christchurch earthquake liquefaction map overlay near Heathcote River

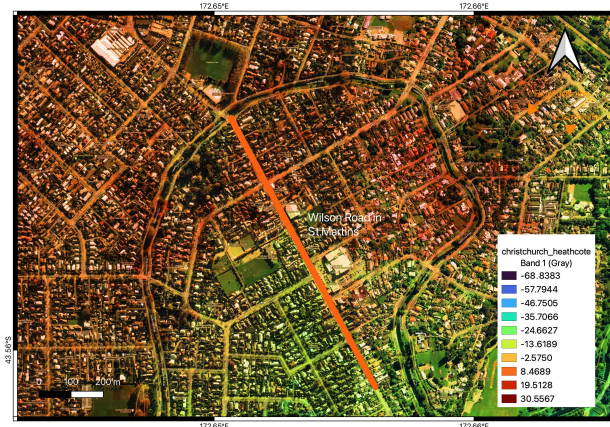


Figure 3.15: InSAR result in St. Martins following the 2011 Christchurch earthquake. (The google earth map is from 2022)



Figure 3.16: Preliminary model of the southeast-dipping fault (rectangular area) that ruptured across the southern part of Christchurch and northern Port Hills during the 2011 Christchurch earthquake. The red, green and yellow symbols show some of the GPS stations whose displacements were used to derive this fault slip model (GNS Media Release, April 2011).

severe liquefaction of its foundation soils (Figure 3.19B). Liquefaction features were also observed near the middle apartment building, but the resulting distress was significantly less than that of the southern apartment building. The southern apartment building suffered a differential settlement of about 40 cm and more than 3 degrees of tilt toward the west-southwest, which is visible in Figure 3.19A. Adjacent to these apartment buildings is another complex of three identical but structurally different (supported on different foundations) two-story duplex housings from the former set. Their locations relative to the geomorphic feature mentioned previously is identical to the three apartment buildings. Figure 3.20A shows the middle duplex housing with clear evidence of pavement distortion, cracking, and settlement of the surrounding ground. The settlement of the housing was likely not significant, but the ground settled about 20 cm, exposing the top of the foundation at the southwest corner (Figure 3.20B) [15]. The tectonic displacement in the Christchurch CBD was about 5 cm of settlement according to the preliminary fault model in Figure 3.16. After removing the tectonic displacement, the InSAR result at the location of this complex of buildings is shown in Figure 3.21. The LOS displacement difference is 7.04 cm between the west and the east of the southern apartment building. The southern apartment building has been removed according to the current satellite image. Assuming no horizontal displacement, this 7.04 cm of difference in the LOS direction can be converted to 9.11 cm of settlement difference, which is way smaller than the observed 40 cm of differential settlement at the southern apartment building. The LOS displacement at the middle duplex housing is 4.73 cm, which can be converted to 6.12 cm of settlement assuming no horizontal displacement. This 6.12 cm of settlement is also smaller than the observed 20 cm of ground settlement.

The second case history is at the intersection of Madras and Armagh streets where several buildings suffered significant liquefaction-induced differential settlements or lateral movements. The three-story building on shallow foundations in Figure 3.22 suffered severe differential settlement that tilted the building by about 1.8 degree. The building also uniformly moved laterally to the north by about 15 cm toward the area of significant liquefaction near the front of the building [15]. The six-story building on isolated footings with tie beams and perimeter grade beams in Figure 3.23 was located across the street to the north. The overall differential settlement across the whole building is about 29 cm [15]. The InSAR result at this location is shown in Figure 3.24. The differential settlement of the first building cannot be revealed by the InSAR result because the resolution of the LOS displacement map is too low that the entire area of the first building has the same LOS displacement. The lateral displacement to the north cannot be revealed by InSAR either because DInSAR is not sensitive to the displacement in the N-S direction. The LOS displacement difference across the area of the second building from north to south is 5.93 cm, which can be converted to 7.67 cm of settlement difference assuming no horizontal displacement. This is again way smaller than the observed 29 cm of differential settlement.

The InSAR result for this methodology failed to resolve the differential settlement of the buildings in both case histories. The differential settlements of the buildings are highly localized. The resolution of the InSAR results depends on the pixel size and pixel spacing of the ALOS-1 scene used in this case study. The pixel size of ALOS-1 scene is 9.37 m by 3.60

m. The pixel spacing is about 20 m judging by the scale bar on the LOS displacement maps in this section. Such resolution is not ideal for analysing highly localized displacements like the differential settlement of buildings caused by liquefaction.

3.4 Discussion

The co-seismic pair InSAR analysis in this case study shows the ability of identifying the fault rupture and the liquefaction damaged areas including the lateral spreading along rivers and ground distortion. However, InSAR was not capable of extracting the meter-level lateral ground displacement due to lateral spreading on the banks of Avon River and Kaiapoi River. This is likely due to phase unwrapping issues with decorrelation caused by the large displacements in a small area.

As discussed in Section 3.3, The InSAR result is not capable of resolving the differential settlements of the buildings caused by liquefaction. This is because the documented differential settlements of buildings are highly localized. The pixel size of an ALOS-1 scene is 9.37 m by 3.60 m and the pixel spacing is about 20 m. Such resolution is not well suited for analysing this type of displacements. The commercial SAR satellite TerraSAR-X launched in 2007 by DLR (the German Aerospace Center) with much higher resolution is more suitable for this purpose. However, TerraSAR-X data set is not free and unfortunately not accessible in this case study.

The InSAR analysis in this case study is greatly limited by the available ALOS-1 data set. Only one co-seismic pair is available in the ascending track for each earthquake. This makes the 3D decomposition of the LOS displacement and the coherence change-method impossible. As a result, the comparison between InSAR analysis results and field observations was performed either by projecting the displacement observed in field to the LOS direction or making assumptions on part of the three displacement components (East, North and Vertical). Pixel offset method is not included in this case study because the pixel offset analysis with ALOS-1 data set generates too many artifacts to recover any meaningful results. The application of these methods is discussed in the next two case studies.

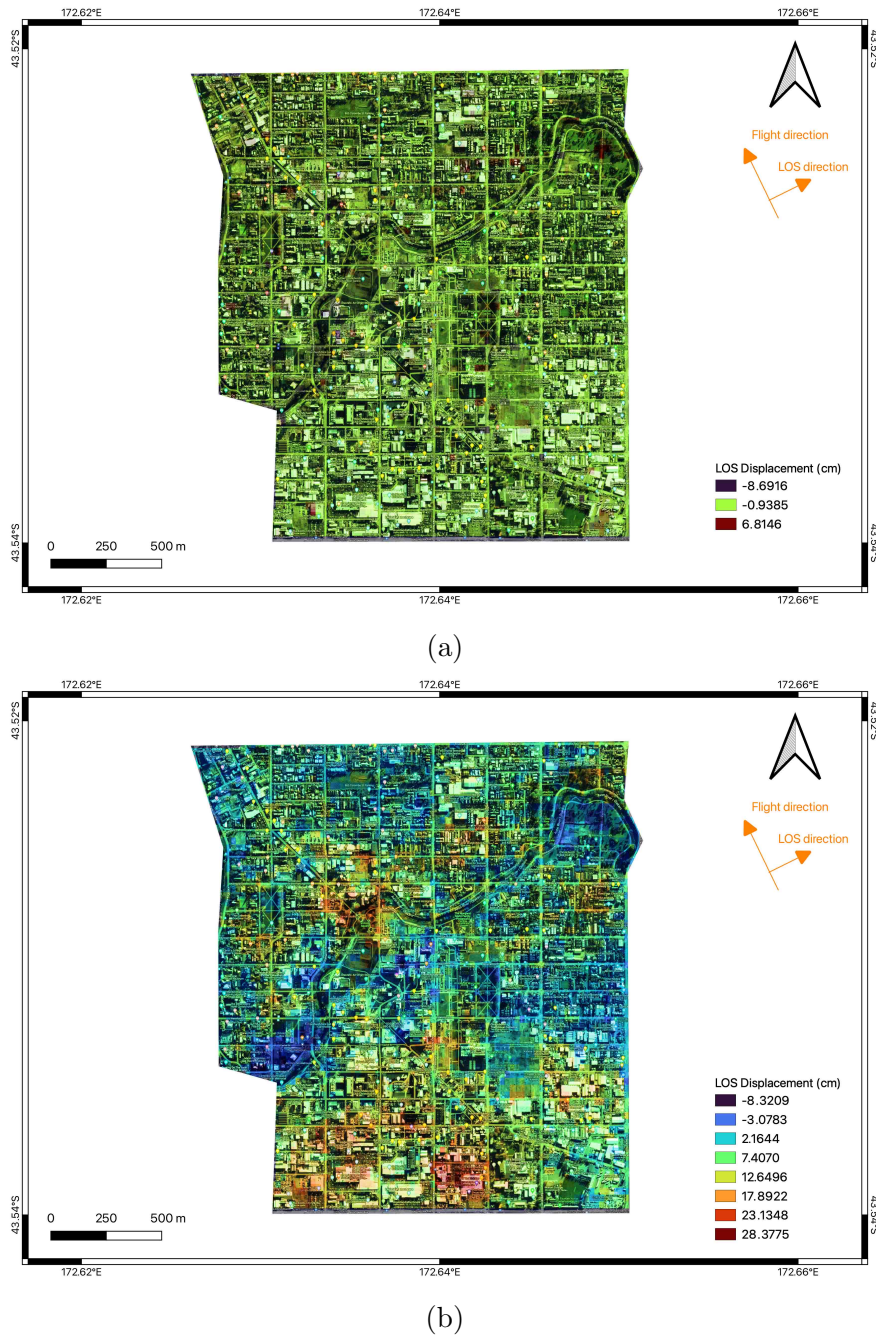


Figure 3.17: (a) InSAR result from the co-seismic pair of the 2010 Darfield earthquake in Christchurch CBD (b) InSAR result from the co-seismic pair of the 2011 Christchurch earthquake in Christchurch CBD

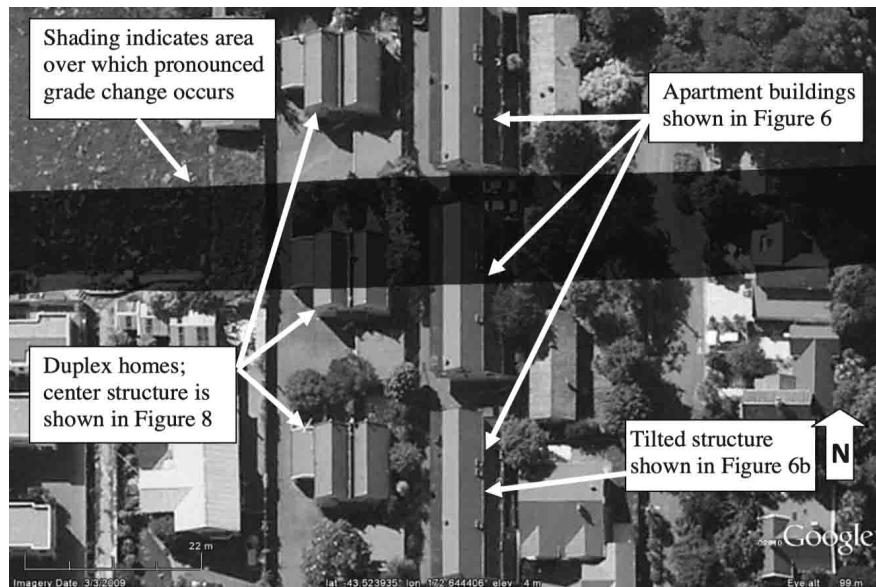


Figure 3.18: Location of geomorphic feature in area of apartment and duplex complexes north of Salisbury Street in CBD [15]. Figure 3.19 corresponds to Figure 6 and Figure 3.20 corresponds to Figure 8 in this figure.

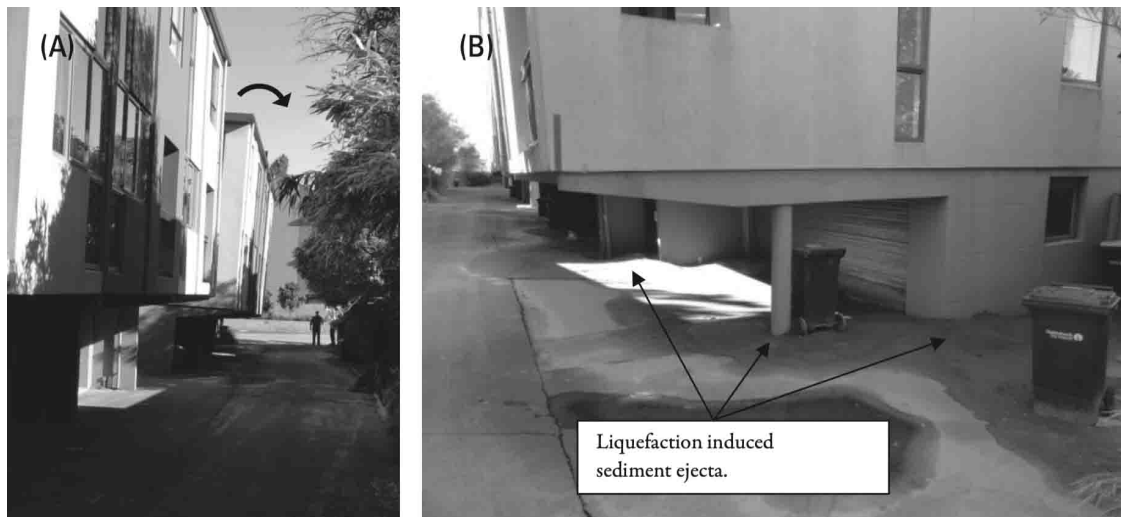


Figure 3.19: Apartment complex: A) looking south from northern building showing tilt of southern building, and B) looking north at liquefaction feature at edge of southern building (7 March 2011; S43.52434 E172.64432) [15].



Figure 3.20: Duplex housing complex: A) looking north at the center building, and B) close-up of ground settlement next to the center building (16 March 2011; S43.52399 E172.64417) [15].

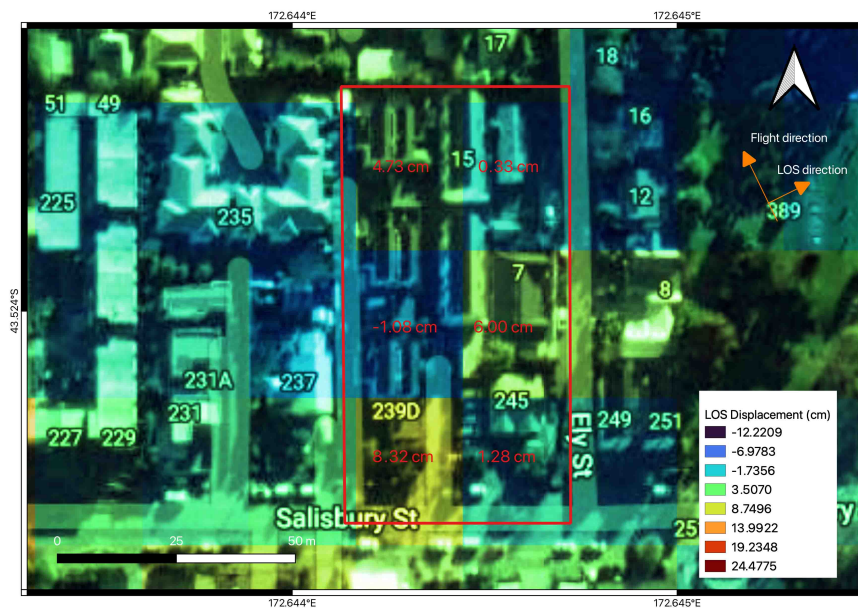


Figure 3.21: The InSAR result at the location of the building complex in Figure 3.18

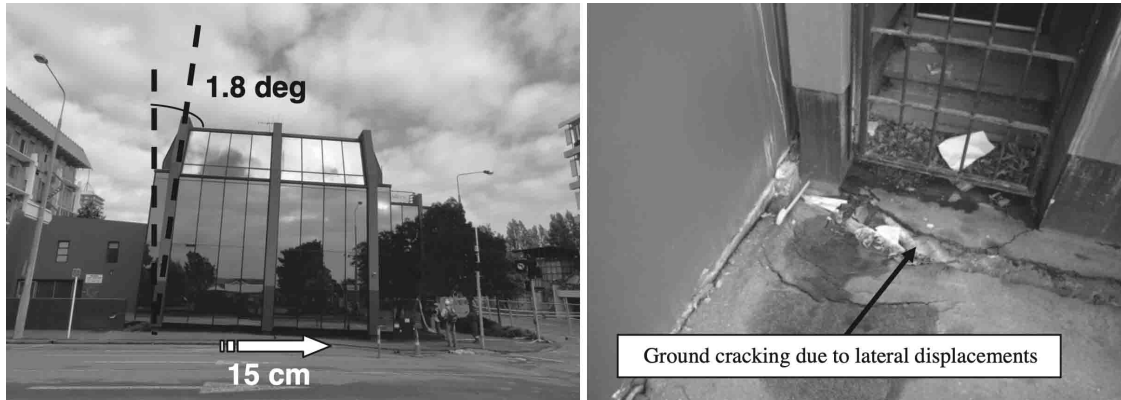


Figure 3.22: Liquefaction-induced differential settlement and sliding of building in the CBD (24 March 2011; S43.52878 E172.64252) [15].



Figure 3.23: Building undergoing significant liquefaction-induced differential settlement due to part of it being founded on the liquefaction feature in this area (24 March 2011; S43.52878 E172.64252) [15].

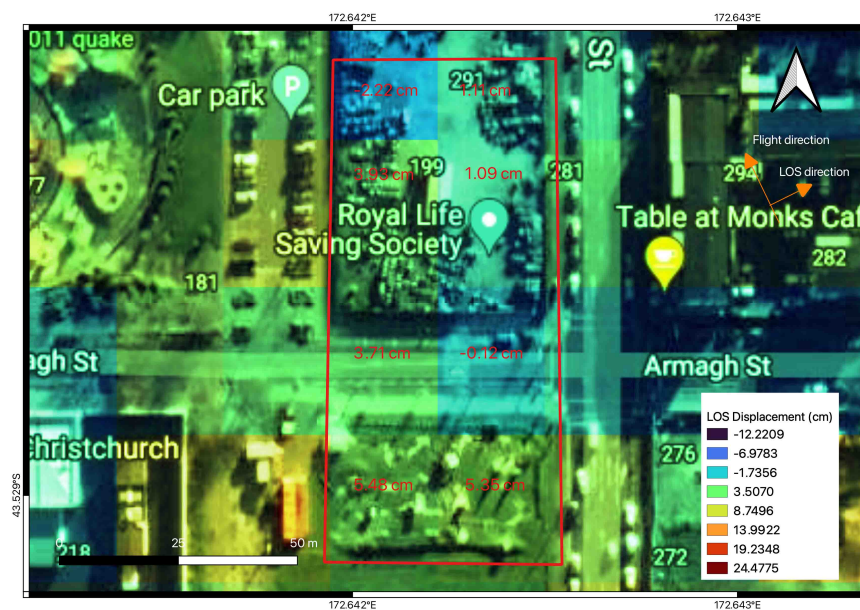


Figure 3.24: The InSAR result at the location of the two buildings in Figure 3.22 and Figure 3.23

Chapter 4

Kumamoto Earthquake Case Study

4.1 Introduction

The 2016 Kumamoto earthquakes are a series of earthquake events starting with a foreshock ($M_w = 6.2$) on the Hinagu fault at a depth of 11 kilometers on April 14th, 2016, followed by another foreshock with moment magnitude 6.0 on the same fault one day later and then the mainshock ($M_w = 7.0$) struck Kumamoto City on April 16th, 2016 at a depth of 10 kilometers on the Futagawa fault [41]. These are the strongest earthquakes recorded in Kyushu, Japan in modern era. Significant damage was caused by these earthquakes to the infrastructure, buildings, roads, slopes and river embankments due to earthquake induced landslides and debris flows. Surface fault rupture on the Hinagu and Futagawa fault produced damage to man-made structures on the ground. Researchers expected huge liquefaction damage after the analysis of optical images and the interpretation of local boring logs before the field reconnaissance. However, liquefaction only occurred in a limited number of locations along the Shirakawa River and the Midorikawa River, and on an artificial island to the west of Kumamoto city. As an exception, there are large liquefaction-induced non-tectonic surface displacements in the Aso Valley to the north east of Kumamoto City. These provide a great opportunity to apply different InSAR analysis methods and test their effectiveness in retrieving the surface displacements.

4.2 Local geology

Kumamoto is located on the Kyushu Island, the southern most among the four major islands of Japan. Kyushu is primarily composed of older, weathered volcanic soils named "shirasu" on the outer side along with marine sediments and weathered rocks. The soils on the inner side predominately originate from the massive Mount Aso Volcano [1]. Kumamoto City has high precipitation of 1000-1500 mm per year and high groundwater levels. The Shirakawa River flows through Kumamoto City from Mount Aso Caldera while the Midorikawa and Kase River flows through the southern portion of the city. The gravel beds of the Midorikawa

River are composed primarily of welded tuff, a volcanic deposit from the slopes of Mount Aso. A significant amount of sandstone sand along the river banks has also been identified and mapped [35]. The Shirakawa, Midorikawa and Kase River regularly flood and deposit suspended fine clay, silt, sand and organic matter on the Kumamoto Plain. Four massive pyroclastic flows occurred from 90,000 to 300 years ago and made up the bulk of the sediment on the Kumamoto Plain. The pyroclastic deposits and secondary alluvial sediments of the most recent pyroclastic flow 300 years ago formed the upper surface of the Kumamoto Plain.

Mount Aso Caldera formed 95,000 years ago and as a result a crater lake filled in with many tens of meters of fine-grained high void ratio sediment [41]. The central cone of the caldera broke through this crater lake and deposited another 10-meter of pyroclastic sediment near the modern surface. A late Pleistocene/Holocene event drained the crater lake through a western passage dissecting the Aso Caldera rim wall, flooding the Kumamoto Plain. The large liquefaction-induced surface displacements in the Aso Caldera is highly related to the soil conditions here.

4.3 InSAR analysis results compared to field observations

Faults ruptured in the 2016 Kumamoto earthquake

The Futagawa-Hinagu fault zone is driven both by the E-W compression derived from Philippine Sea plate subduction and the N-S extension of the Central Kyushu rift [48]. The predominant fault movement for both faults is right-lateral strike-slip, accompanied with the uplift of the Kyushu mountains in the south because of the normal fault movement.

The $M_w = 6.2$ foreshock on April 14th, 2016 happened on the northernmost segment of the Hinagu Fault. The $M_w = 6.0$ foreshock happened ~ 3 hours later on the southwestern extension of the previous foreshock area. The amount of co-seismic right-lateral strike-slip is estimated to be 1.1 m [40]. The $M_w = 7.0$ mainshock on April 16th, 2016 happened around the north-western tip of the foreshock area along the Futagawa fault. The mainshock triggered widespread seismicity along the northernmost section of the Hinagu Fault and the northeastern extension of the Futagawa Fault, including the north flank of Mount Aso volcano and the area around Oita [40]. The different fault segments that were ruptured are shown in Figure 4.1. The average right-lateral strike-slip along the longest fault segment A1 was estimated at 4.1 m. There was a normal slip component on this segment as well. Fault segment A2 is located within the Mount Aso Caldera. The average right-lateral strike-slip was estimated to be 3.8 m. Fault segment B is located at the northernmost segment of the Hinagu Fault. The estimated right-lateral strike-slip from both the foreshock and the mainshock was about 3 m [40].

The InSAR data sets used in this case study to compare with the GNSS observations shown in Figure 4.1 are summarized in Table 4.1. Pixel offset was selected to perform the InSAR analysis instead of the conventional differential InSAR method for two reasons:

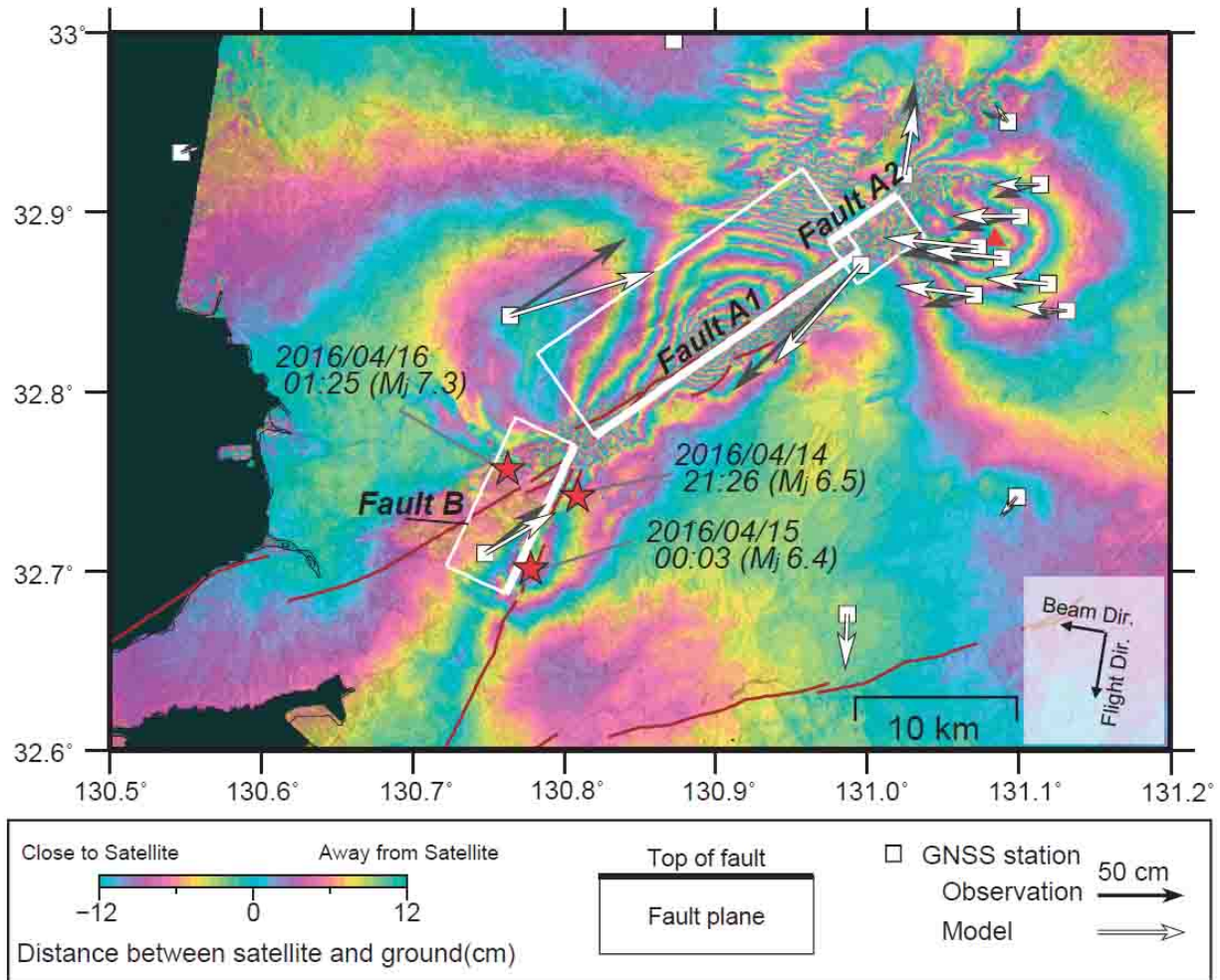


Figure 4.1: Source fault model for the hosts of both the foreshock and the mainshock. The three white rectangles denote fault planes projected onto the surface. Black and white arrows at each GNSS station indicate horizontal displacements observed and predicted from the source model. (Background interferogram is from the ALOS-2 co-seismic pair between March 7th, 2016 and April 18th, 2016 on descending track) [40]

| Satellite | Time | Flight Direction | Band | Wavelength (cm) |
|-------------|------------|------------------|--------|-----------------|
| ALOS-2 | 03/07/2016 | Descending | L-Band | 22.9 |
| ALOS-2 | 04/18/2016 | Descending | L-Band | 22.9 |
| Sentinel-1A | 04/08/2016 | Ascending | C-Band | 5.6 |
| Sentinel-1A | 04/20/2016 | Ascending | C-Band | 5.6 |
| Sentinel-1A | 03/27/2016 | Descending | C-Band | 5.6 |
| Sentinel-1A | 04/20/2016 | Descending | C-Band | 5.6 |

Table 4.1: SAR data sets used in the 2016 Kumamoto earthquake case study

1. the N-S component of the fault movement is large according to the fault trace. While differential InSAR is not sensitive to displacement in the azimuth direction, pixel offset method can reveal the displacement in both the azimuth and the range direction; and, 2. The meter-level fault movement caused decorrelation along the fault trace. As a result, reliable phase unwrapping cannot be performed in those areas. The range and azimuth pixel offset results from the ALOS-2 descending co-seismic pair, and the range pixel offset result from the Sentinel-1A ascending co-seismic pair were used to perform the 3D decomposition of the fault movement in the N-S, E-W and vertical directions. The results are shown in Figure 4.2, Figure 4.3, and Figure 4.4. At GNSS Location 1, the E-W displacement component is -1.31 m and the N-S displacement component is -0.9 m. The combined displacement is 1.59 m in the southwestern direction. The observed horizontal displacement from Figure 4.1 is 1.17 m. Using the same method, the fault movement at the north side of the Fault A2 is 1.6 m in the northeastern direction¹, and the fault movement at the south side of the Fault A2 is 2.05 m in the southwestern direction. The relative right-lateral strike slip is 3.65 m which is close to the 3.8 m estimation in Kato et al. 2016 [40]. At GNSS location 2, the E-W displacement component is 0.74 m and the N-S displacement component is 0.48 m. The combined displacement is 0.88 m in the northeastern direction. The observed horizontal displacement from Figure 4.1 is 1 m. With 2.14 m displacement in the northeastern direction at the north side of Fault A1 and 1.81 m in the southwestern direction at the south side, the relative right-lateral strike-slip is 3.95 m, which is also close to the 4.1 m estimation in Kato et al. 2016 [40]. The analysis of Fault B is not part of this case study because of the coverage of available ALOS-2 data sets.

Kato et al. 2016 [40] mentioned a significant normal slip component along the Fault A1 discovered from geodetic inversion and the northwestern side of the active fault trace subsided after the mainshock. The substantial vertical movement shown in Figure 4.4 can prove the existence of this normal slip component. But there is no estimate of this normal slip component in Kato et al. 2016 [40] and it is hard to determine whether this subsidence of the northwestern side of the fault is relative to the southeastern side of the fault. Therefore,

¹The N-S and E-W fault slip components mentioned in this section were average values along the fault trace output from QGIS.

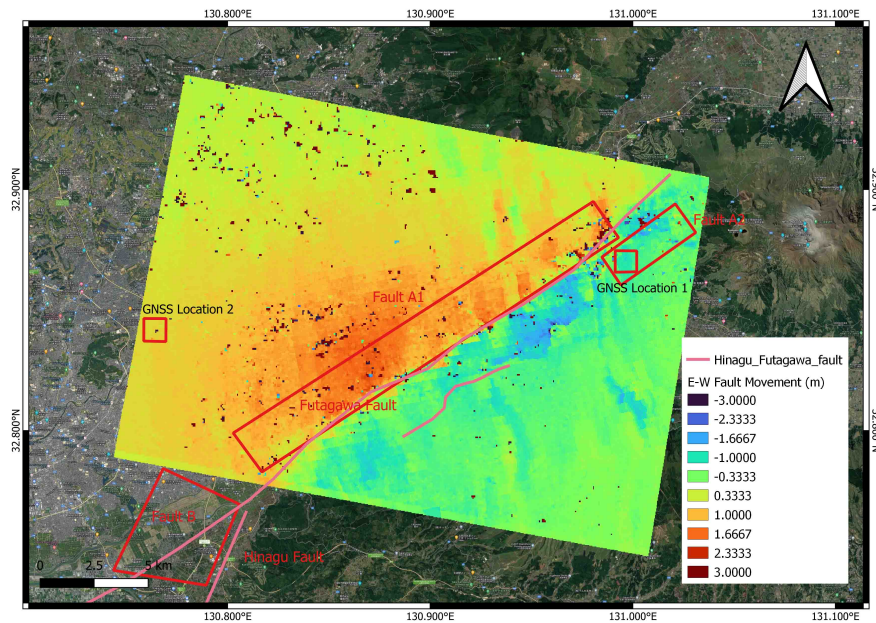


Figure 4.2: E-W fault movement map (East movement is positive.)

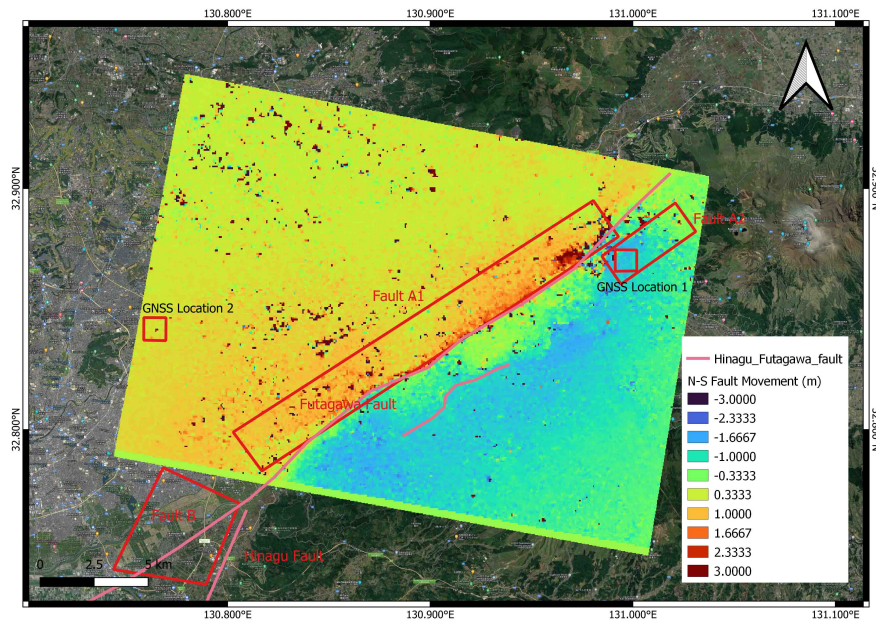


Figure 4.3: N-S fault movement map (North movement is positive.)

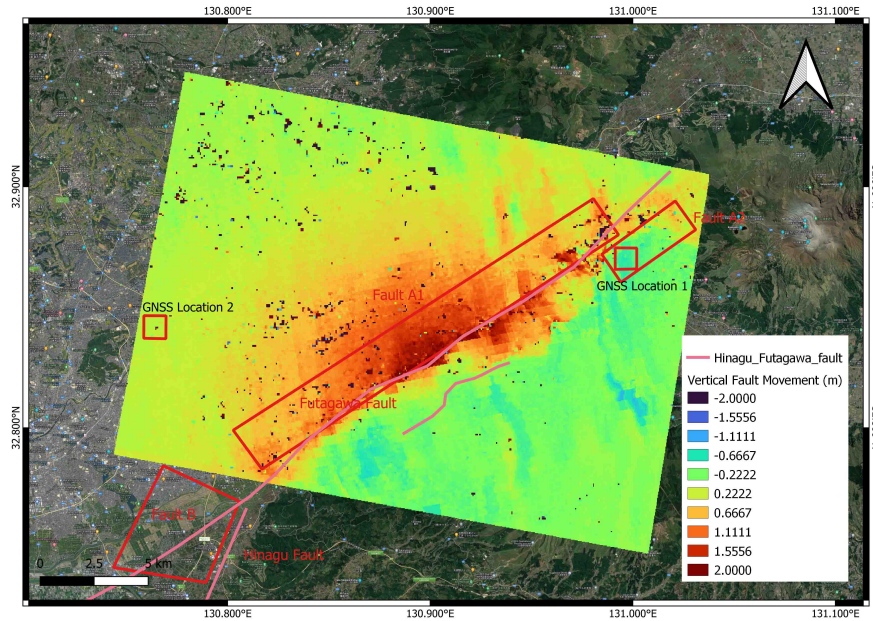


Figure 4.4: Vertical fault movement map (Uplift is positive.)

it is not possible to validate the vertical fault movement map in Figure 4.4.

Overall, the results from pixel offset analysis in this case study agree quite well with the estimations and GNSS observations in Kato et al. 2016 [40].

Liquefaction-induced surface displacements in the Aso Valley

The Aso valley is located in the northern part of the Mount Aso Caldera. It formed in a depression after the fourth Aso pyroclastic flow, and the valley floor was covered by lava and related deposits from Mount Aso and also by sediments of the Kuro-kawa River [30]. There was a lake in the western Aso Valley about 10,000 years ago, and the lake-bottom deposits with a thickness of approximately 50 m were found in a boring [30]. It was reported that casing pipe of the Uchinomaki hot springs was bent at the depth of about 50 m following the mainshock and a saturated silt layer was found at a depth of about 20 m in the Matoishi area [62]. Fujiwara et al. 2017 [23] suggested the liquefaction of these saturated lake-bottom deposits due to strong ground motions caused the large deformation due to lateral spreading.

Surface ruptures caused by liquefaction-induced lateral spreading in the Aso Valley interpreted from aerial photos are shown in Figure 4.5 [71]. The total horizontal displacement map on this figure is from Fujiwara et al. 2017 [23]. Fujiwara et al. 2017 [23] used the pixel offset method to get this total horizontal displacement map with only ALOS-2 data set. But since ALOS-2 data set is not free, it is meaningful to test whether pixel offset method with hybrid data sets (ALOS-2 and Sentinel-1) can reach the same result in this case study. Some photos taken from the field in the Matoishi area that show typical compression and exten-

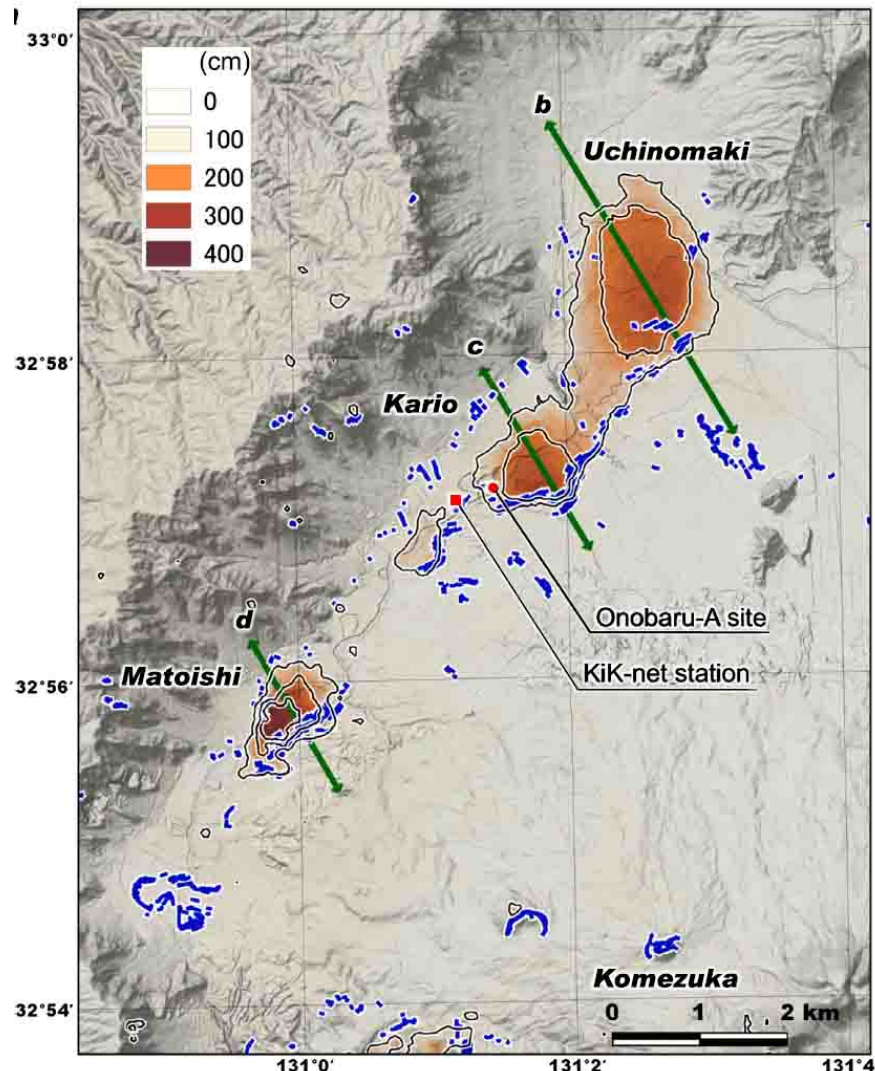


Figure 4.5: Irregular blue lines show surface ruptures caused by liquefaction-induced lateral spreading interpreted from aerial photos [71]. Total horizontal displacement map is from Fujiwara et al. 2017 [23].

sion surface features are presented in Figure 4.6 [23]. In this case study, the same InSAR data sets (as shown in Table 4.1) and the pixel offset method were used to generate the displacement maps in the E-W, N-S and vertical directions in the Aso Valley. The results from InSAR analysis were then compared with the field observations and the displacement map in Fujiwara et al. 2017 [23].

The displacement maps in the E-W, N-S and vertical directions from the InSAR analysis in the Aso Valley are shown in Figure 4.7, Figure 4.8, and Figure 4.9. The total horizontal displacement map is shown in Figure 4.10. Figure 4.10 shows large horizontal displacement in

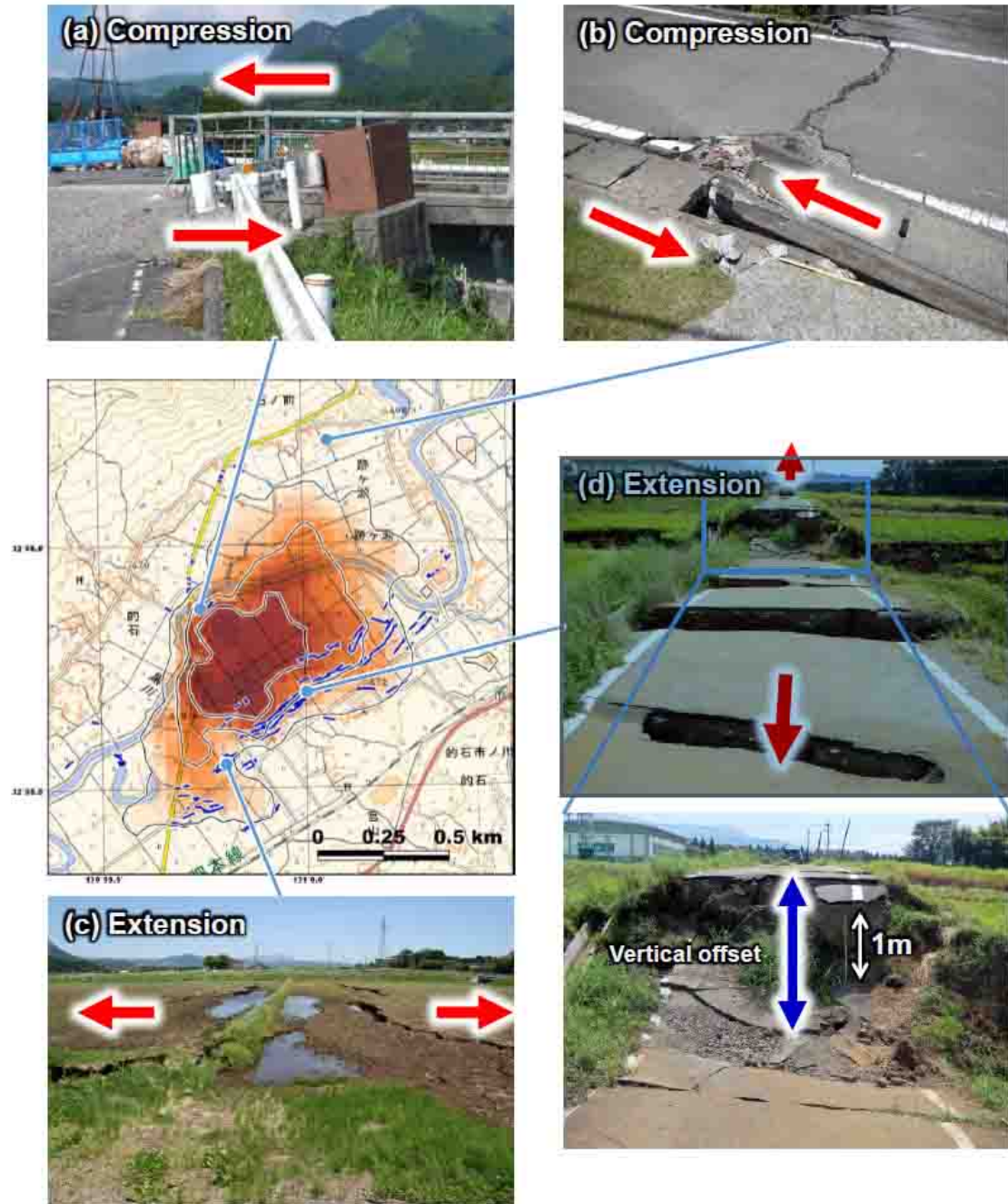


Figure 4.6: Photos of typical compression and extension surface features in the Matoishi area [23].

the Uchinomaki, Kario, and Matoishi area. Uchinomaki has famous hot springs. According to the displacement map of Uchinomaki shown in Figure 4.11, the largest horizontal displacement was 1.95 m to the NNW direction at the center of Uchinomaki, at the hot springs. The horizontal displacement is getting smaller when it is closer to the edge of Uchinomaki. There is also about 0.3 m of uplift at the center of Uchinomaki. The diameter of the deformed area here is about 2 km. The displacement map of Kario is shown in Figure 4.12. The largest horizontal displacement is 2.63 m to the NNW direction at the southern Kario. There is about 0.7 m of uplift at this location. Again the displacement is getting smaller when it is closer to the edge of Kario. The displacement map of Matoishi is shown in Figure 4.13. The largest horizontal displacement is 4.37 m to the NNW at the northwestern Matoishi. There is also about 0.7 m of uplift at this location. To compare the InSAR result with the four field observations presented in Figure 4.6, the E-W displacement at these four locations are analyzed as shown in Figure 4.14. In this case, the E-W displacement shows the relative displacement on different sides of each location better than the N-S displacement when the N-S displacement is large and does not vary a lot in this area. Location (a) and (b) showed compression feature in the field. The west and east side of these two locations are both getting closer with 0.76 m and 0.44 m of relative displacement as shown in Figure 4.14. Location (c) and (d) showed extension feature in the field. As shown in Figure 4.14, the west and east side of these two locations are both moving apart with 0.15 m and 0.49 m of relative displacement, respectively. Location (c) showed about 1 m of vertical offset. The uplift on west and east side of location (c) are 0.72 m and 0.18 m from the InSAR result. Only 0.54 m of vertical offset can be resolved at this location. This is because this vertical offset is highly localized. The horizontal scale of this rupture is likely smaller than the 45 m pixel spacing of ALOS-2 data set [23], which means pixel offset method with ALOS-2 data set cannot reveal this vertical offset.

The InSAR analysis results in this case study discussed previously are generally consistent with the results from Fujiwara et al. 2017 [23] (Table 4.2). The large horizontal displacement also happened at the locations with visible surface ruptures on aerial photos (Figure 4.5). The relative displacements at the locations of these four field observations are also consistent with the compression or extension surface feature observed in the field. Therefore, the InSAR analysis results with pixel offset method using hybrid data sets (ALOS-2 and Sentinel-1) are on par with the pixel offset method with only ALOS-2 data set in Fujiwara et al. 2017 [23] in revealing the lateral ground displacement caused by liquefaction in the Aso Valley.

Liquefaction in Kumamoto City

There were only a limited number of sites with liquefaction damage in Kumamoto City. The overestimation of liquefaction damage caused by the 2016 Kumamoto earthquake is an interesting topic. Anderson et al. 2022 [1] came to the conclusion that this overestimation is due to the misinterpretation of Japanese boring log and aerial photographs, and the volcanic soil in Kumamoto City is more resistant to liquefaction than current liquefaction triggering analysis procedures suggest. Post-liquefaction settlement was observed on the artificial island

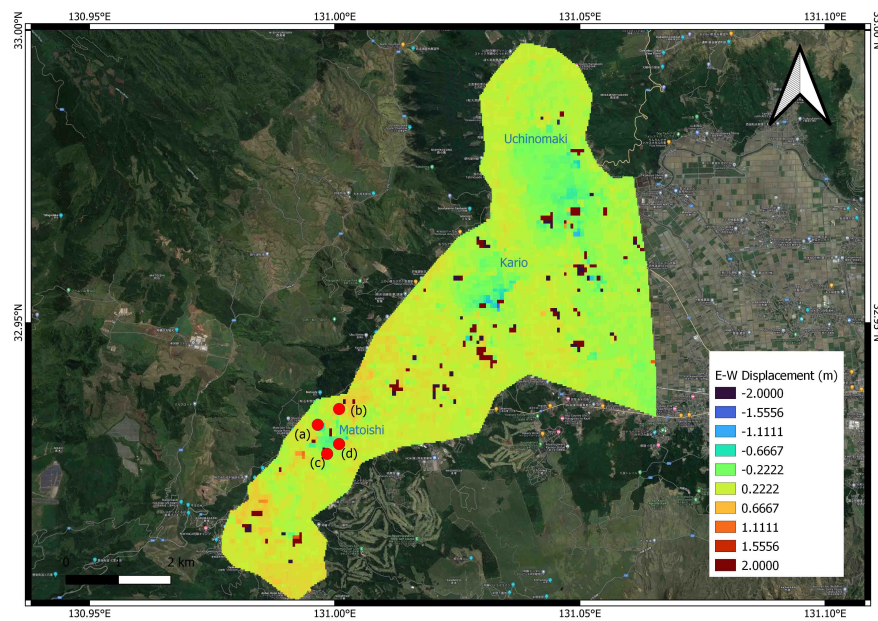


Figure 4.7: E-W displacement map in the Aso Valley (East movement is positive.)

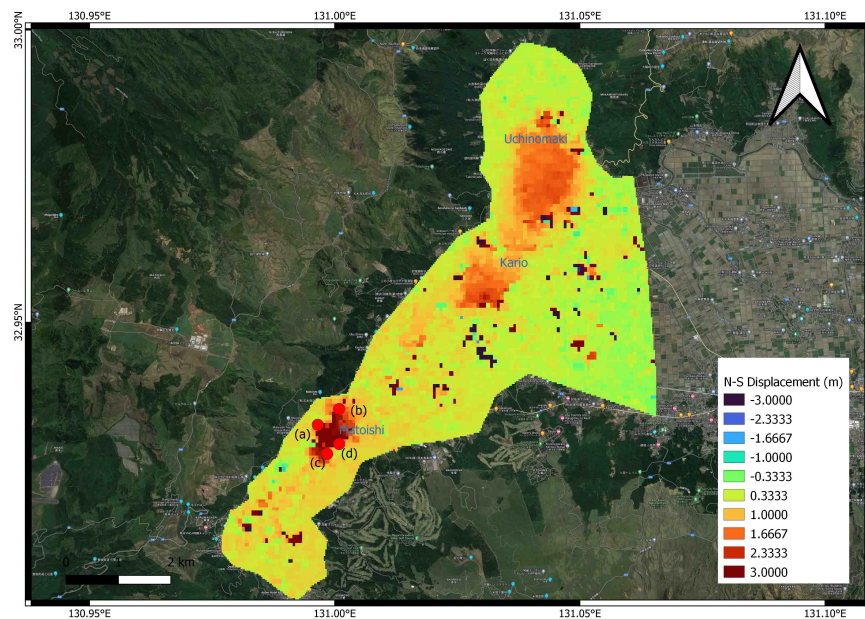


Figure 4.8: N-S displacement map in the Aso Valley (North movement is positive.)

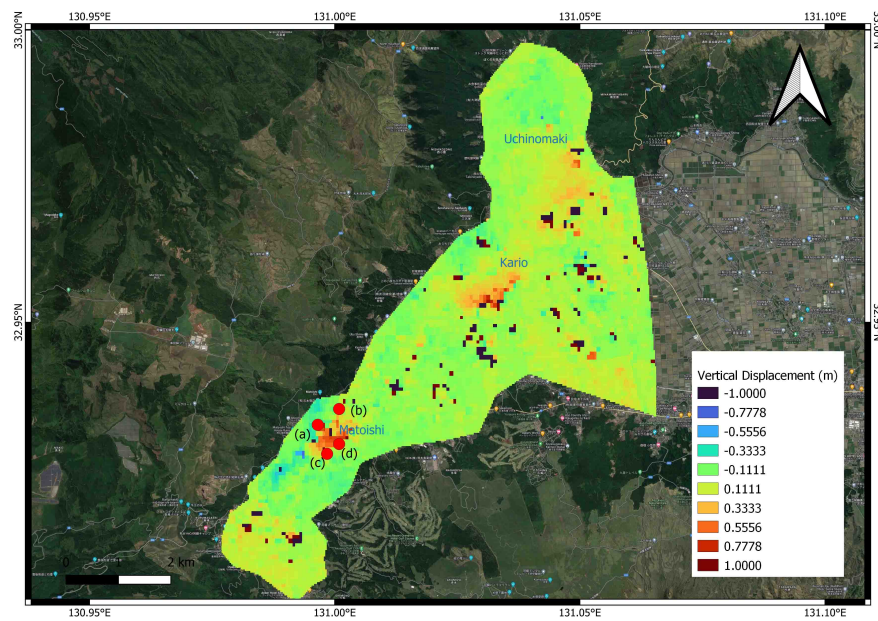


Figure 4.9: Vertical displacement map in the Aso Valley (Uplift is positive.)

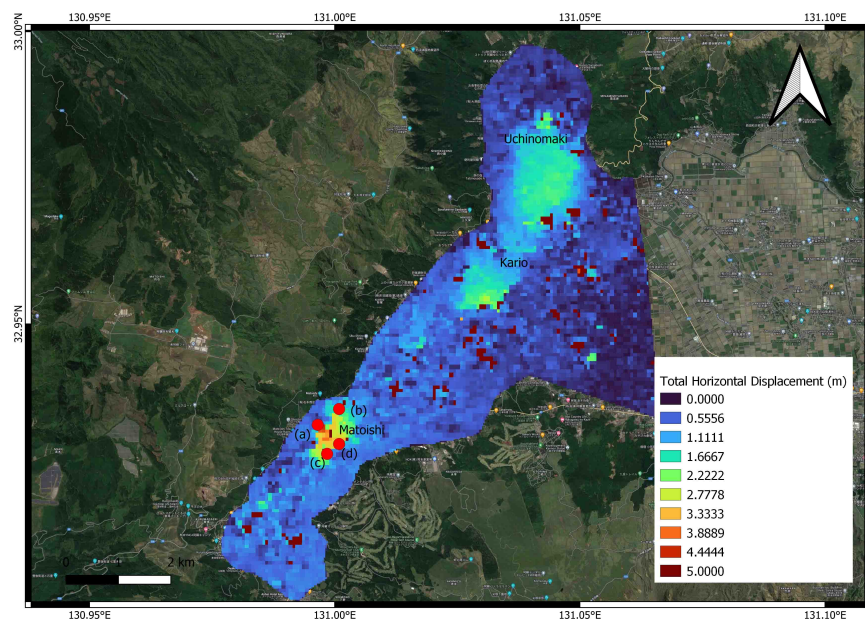


Figure 4.10: Total Horizontal displacement map in the Aso Valley

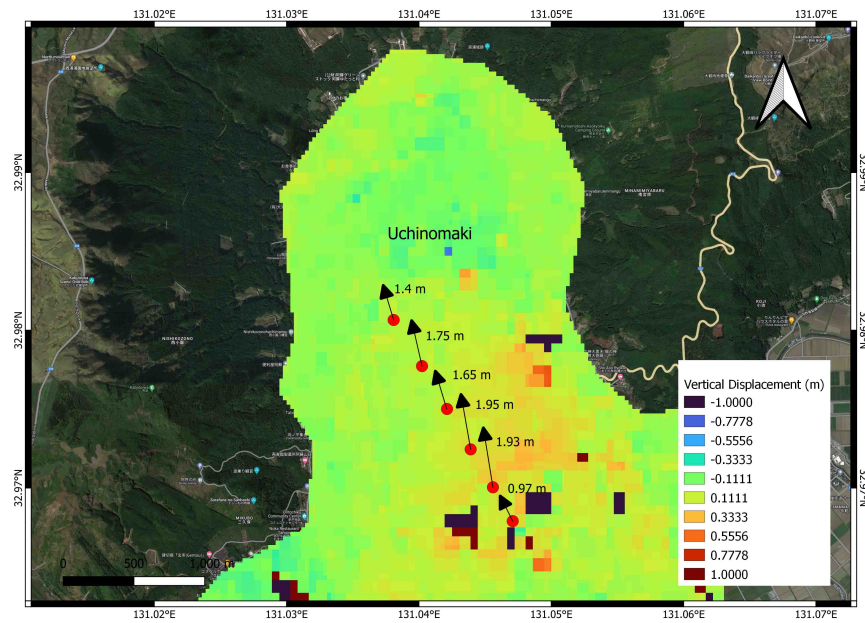


Figure 4.11: Displacement map in Uchinomaki

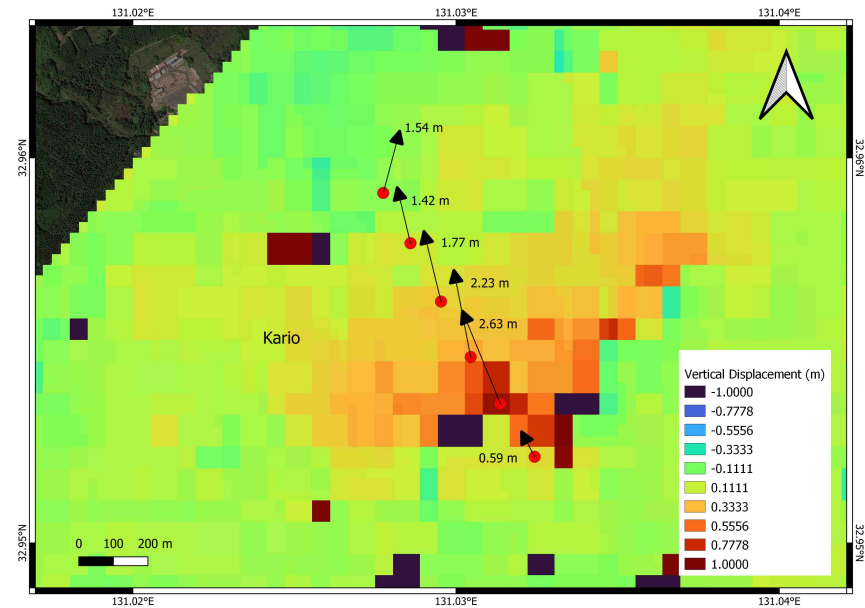


Figure 4.12: Displacement map in Kario

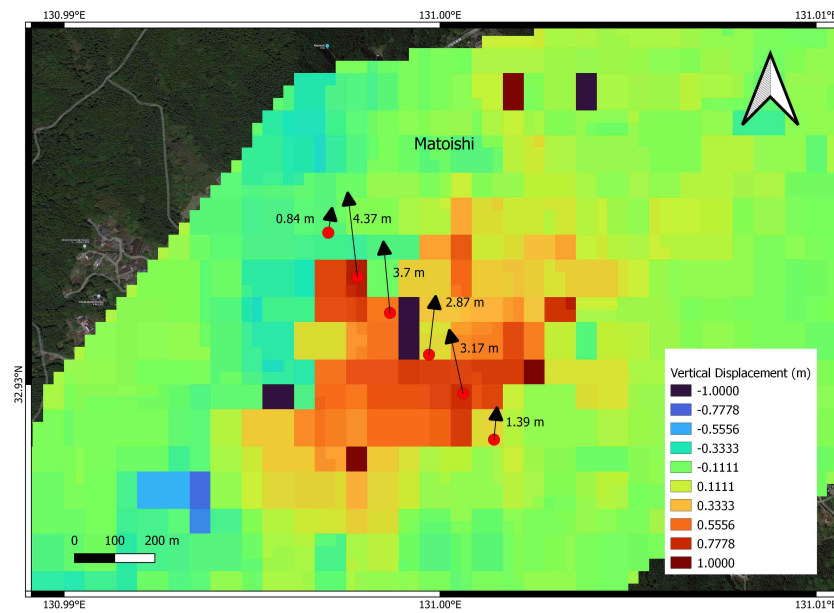


Figure 4.13: Displacement map in Matoishi

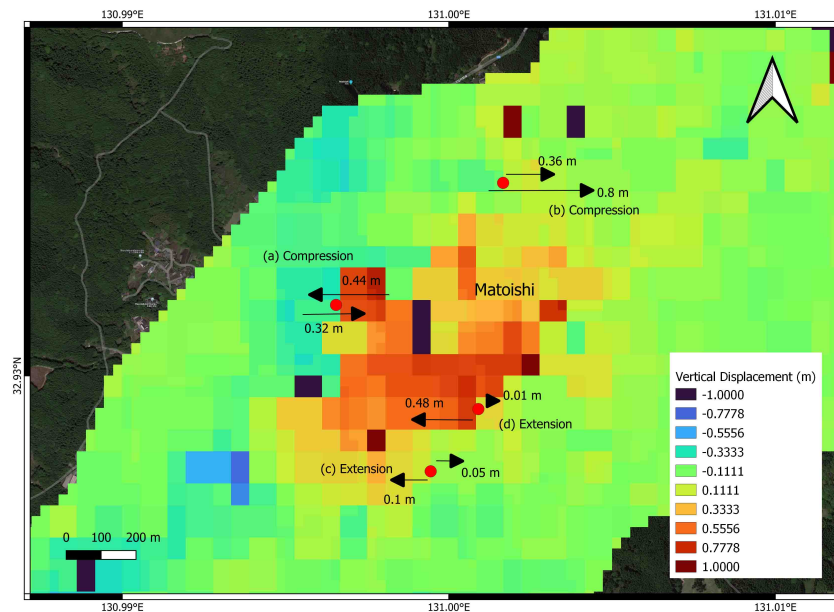


Figure 4.14: E-W displacement at the locations of four field observations

| Area | Max Horizontal Disp | Vertical Disp |
|------------|---------------------|----------------------------------|
| Uchinomaki | 2.6 m to NNW | 25 cm uplift to 10 cm subsidence |
| Kario | 2.8 m to NNW | 40 cm uplift to 40 cm subsidence |
| Matoishi | 3.4 m to NNW | 50 cm uplift to 50 cm subsidence |

Table 4.2: The maximum horizontal displacement and the vertical displacement range along the cross sections b, c and d in Figure 4.5 from the InSAR analysis results in Fujiwara et al. 2017 [23]

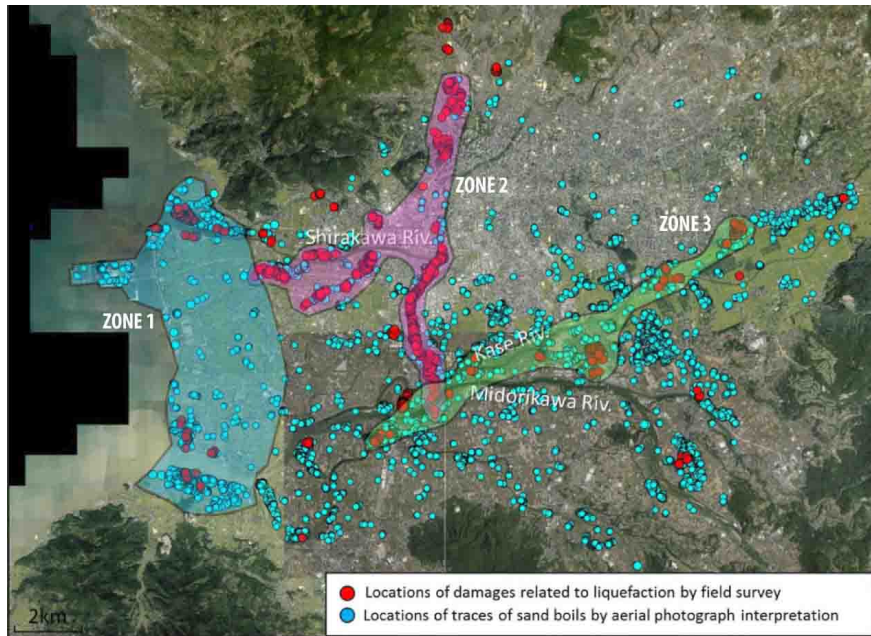


Figure 4.15: Liquefaction map in Kumamoto City

to the west of Kumamoto City with localized settlements up to 60 cm at some locations [41]. In the south-east corner of the Shirakawa River, settlement and tilting of the buildings in this neighborhood due to liquefaction was observed [41, 55, 60, 4]. One lateral spreading case was observed by Kayen et al. 2016 [41] adjacent to a bridge crossing a tributary of the Midorikawa River at the east of Kumamoto City. A liquefaction map of Kumamoto City with liquefaction damaged locations observed in field surveys is shown in Figure 4.15 [2]. Because the conventional DInSAR method with L-Band ALOS-1 data sets could not resolve the lateral spreading displacements along the rivers or the settlement and tilting of the buildings within the Christchurch CBD in Chapter 3, and the pixel offset method does not have enough resolution to detect those localized damages in urban areas. Therefore, coherence-change method was selected in this case study.

The SAR data sets used for coherence-change analysis are listed in Table 4.3. Scenes

| Satellite | Time | Flight Direction | Band | Wavelength (cm) |
|-------------|------------|------------------|--------|-----------------|
| Sentinel-1A | 02/20/2016 | Ascending | C-Band | 5.6 |
| Sentinel-1A | 04/08/2016 | Ascending | C-Band | 5.6 |
| Sentinel-1A | 04/20/2016 | Ascending | C-Band | 5.6 |

Table 4.3: SAR data sets used in the coherence change method

from 2/20/2016 and 04/08/2016 were used to calculate the pre-seismic coherence. Scenes from 04/08/2016 and 04/20/2016 were used to calculate the co-seismic coherence. The normalized coherence change was then calculated based on Equation 2.3. Larger normalized coherence change means larger coherence decrease after the earthquake strikes. Watanabe et al. 2016 [64] suggested a normalized coherence change threshold of 0.3 for identifying liquefaction damaged areas in the 2015 Gorkha earthquake. However, since the data set used by Watanabe et al. 2016 [64] is from ALOS-2, this threshold might not be usable for Sentinel-1A data set in the Kumamoto City case study. Therefore, the normalized coherence change threshold needed to be calibrated. Because the liquefaction induced lateral displacement in the Aso Valley has been analyzed in detail as already discussed, it was used to find the optimum threshold. The areas with normalized coherence change larger than 0.4 are shown in Figure 4.16. Those areas (white, bluish dots) are generally located within the three areas with large horizontal displacements: Uchinomaki, Kario and Matoishi. After trial and error, 0.4 was picked as the normalized coherence change threshold for liquefaction damage identification in this case study. The normalized coherence change map in Kumamoto City with the same 0.4 threshold is shown in Figure 4.17. Apart from the areas with field observed liquefaction damage, many other areas on the map also has greater than 0.4 of normalized coherence change. This indicates that the 0.4 threshold might not be high enough for urban areas. After raising the threshold to 0.45, the updated map is shown in Figure 4.18. This time the areas with normalized coherence change larger than 0.45 shows much better correlation to the areas with field observed liquefaction damage. Zoom in on the liquefaction damaged areas mentioned previously in this section. The artificial island to the west of Kumamoto City, the neighborhood at the south-east corner of Shirakawa River, and the bridge crossing a tributary of the Midorikawa River at the east of Kumamoto City all have concentrations of large normalized coherence change area as shown in Figure 4.19 to Figure 4.21. Therefore, with the proper normalized coherence change threshold, coherence-change method works well for liquefaction detection.

4.4 Discussion

Pixel offset method shows the ability of resolving the Futagawa-Hinagu fault rupture displacement and the lateral ground movement caused by liquefaction in the Aso Valley. The pixel offset method using hybrid data sets (ALOS-2 and Sentinel-1) performs on par with



Figure 4.16: Normalized coherence change in Aso Valley

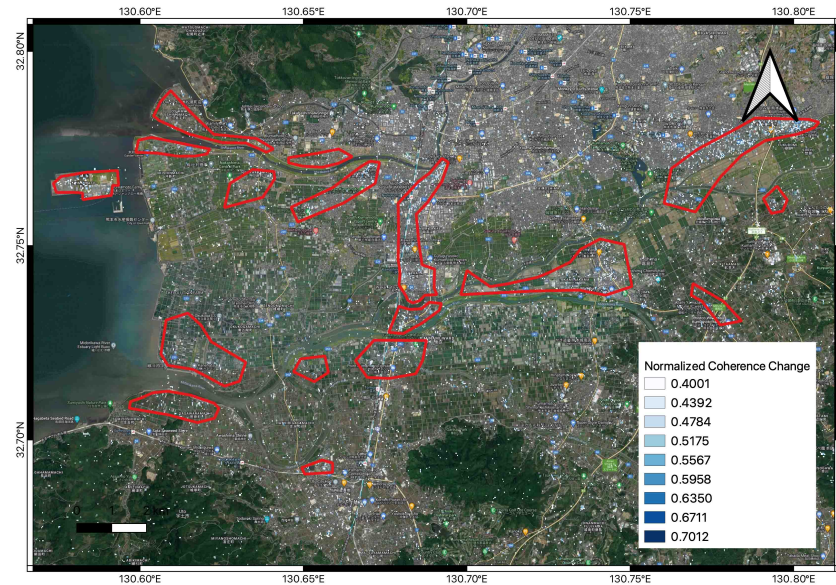


Figure 4.17: Normalized coherence change in Kumamoto City with liquefaction damaged areas bounded by red lines

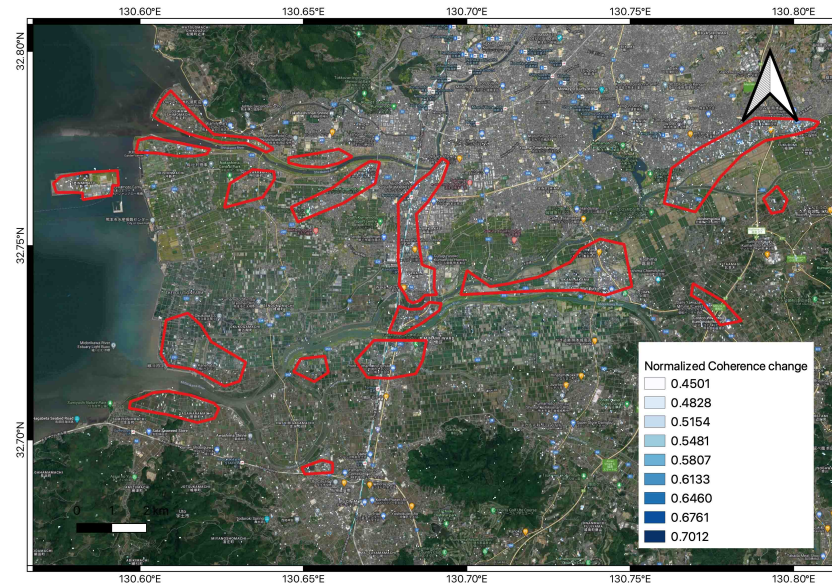


Figure 4.18: Updated normalized coherence change in Kumamoto City with liquefaction damaged areas bounded by red lines



Figure 4.19: Normalized coherence change at the artificial island to the west of Kumamoto City

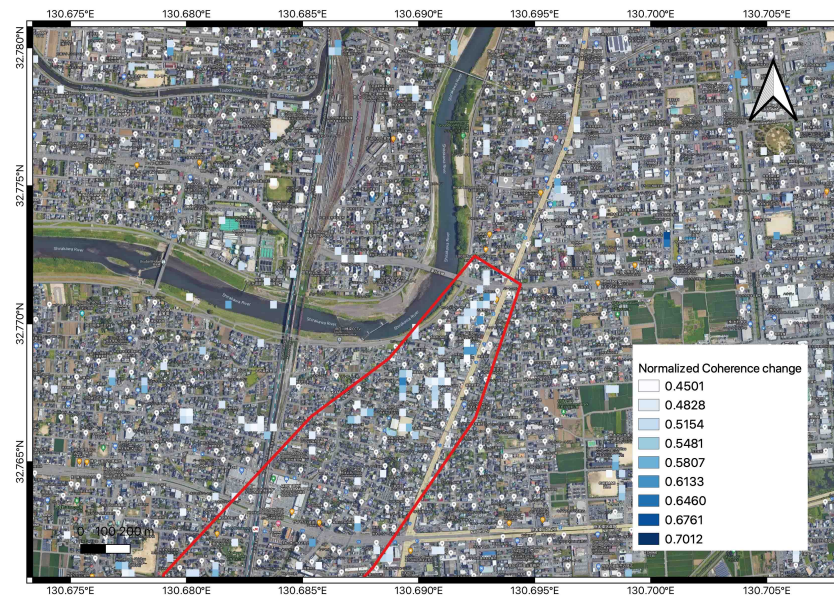


Figure 4.20: Normalized coherence change at the south-east corner of Shirakawa River

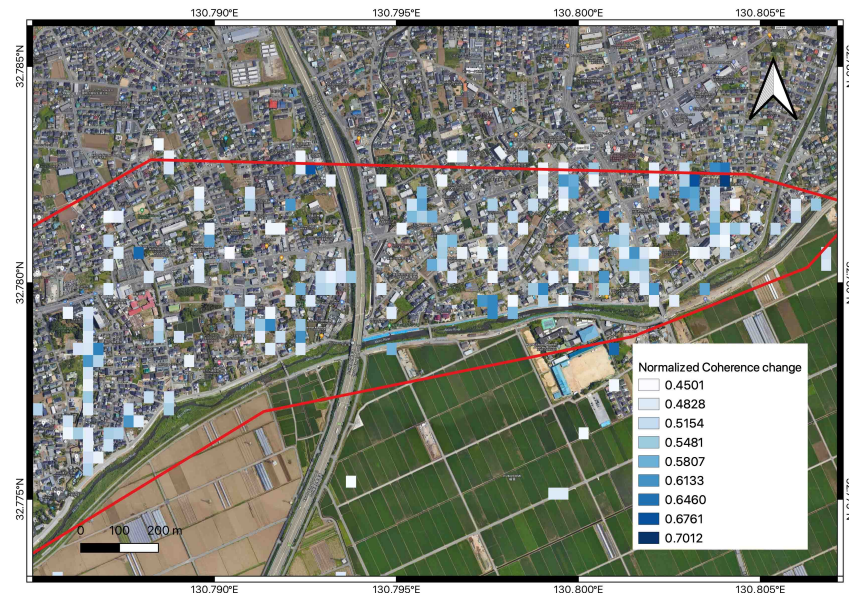


Figure 4.21: Normalized coherence change at the bridge crossing a tributary of the Midorikawa River at the east of Kumamoto City

the pixel offset method using only ALOS-2 data set in Fujiwara et al. 2017 [23]. The N-S component of the horizontal displacements in the Aso Valley is dominant compared to the E-W component and the vertical displacements. As a result, conventional DInSAR method with either ALOS-2 or Sentinel-1A data set is not suitable for revealing the displacements here because InSAR has low sensitivity on the ground displacement in the N-S direction, which is too close to the azimuth direction.

The coherence-change method achieved great result with 0.4 as the normalized coherence change threshold in the Aso Valley. However, in Kumamoto City with the same threshold, the method no longer worked because many areas without field observed liquefaction damage also have normalized coherence change greater than 0.4. After raising the threshold to 0.45, the method successfully detected liquefaction damage. Thus, the normalized coherence change threshold is the key to the coherence-change method and the optimum threshold may vary with InSAR data set from different satellites and at different locations.

Chapter 5

Hokkaido Eastern Iburi Earthquake Case Study

5.1 Introduction

The $M_w = 6.6$ Hokkaido Eastern Iburi earthquake struck the central eastern part of the Iburi area on the northernmost major island of Japan on September 6th, 2018 at a depth of approximately 37 km. This earthquake occurred after a large amount of precipitation in August 2018 and the arrival of Typhoon No. 21 Jebi. It caused a large loss of life, and significant damage to residential areas, farmlands, infrastructure, and lifelines over a wide area of Hokkaido [36]. Widespread slope failures occurred in the mountainous areas composed of pyroclastic fall deposit in Atsuma and Abira near the epicenter [36]. A flow failure caused by liquefaction was observed in a residential community district of Kiyota ward in Sapporo [42]. It was, therefore, meaningful to test whether InSAR analysis can detect the various types of the ground failures that occurred in this earthquake.

5.2 Local Geology

Hokkaido Island is located in one of the most tectonically active regions [77]. It is subject to westward subduction of the Pacific Plate and convergence between the North American and Eurasian Plates [59]. Modern Hokkaido was shaped primarily by Miocene age submarine volcanism. From west to east, Hokkaido Island consists of the Yufustu basin (home to Sapporo, Chitose, and Tomakomai), the Hidaka Collision Zone, and the eastern highlands shaped by a sequence of Himalayan Orogeny plutons and metamorphism at the Hidaka Collision Zone [42].

The surface soil layers in Atsuma and Abira, where widespread landslides occurred, are composed of pyroclastic tephra deposits mainly derived from Tarumae Caldera [77]. The depth of the pyroclastic tephra deposits is approximately 4-5 m [70]. The high precipitation in August, 2016 ahead of the arrival of Typhoon Jebi, which caused high saturation of the

surface soil in the region, greatly contributed to the occurrence of landslides during the 2018 Hokkaido earthquake [77].

5.3 InSAR analysis results compared to field observations

Fault ruptured in the 2018 Hokkaido earthquake

The westward subduction of the Pacific Plate formed many eastward dipping thrust faults on the western side of the Hidaka Mountains [38]. The 2018 Hokkaido earthquake occurred at the west edge of this thrust fault system [44]. There is an active fault zone located close to the epicenter of this earthquake named Ishikari-Teichi-Toen fault zone (ITTFZ). It is controversial whether the 2018 Hokkaido earthquake occurred on a fault that is part of the ITTFZ system. Kobayashi et al. 2019 [44] determined that the fault plane where the earthquake occurred does not connect to any known surface traces of the ITTFZ and constructed a reverse fault model dipping eastward at 74 degrees with a 15 km deep fault top by inverting ALOS-2 and GNSS data sets. Figure 5.1 shows the displacement maps in the vertical and E-W direction derived from ALOS-2 data sets and the fault model [44]. Both the InSAR analysis and fault model show up to 8-10 cm of uplift and 4 cm of eastward displacement on the east side of the fault. Since the ALOS-2 data set in this region was not accessible for this case study, Sentinel 1A/B data set was used. The Sentinel 1A/B data set used in this case study is summarized in Table 5.1. As C-Band data set, Sentinel-1 A/B has low coherence in Japan especially in the mountainous area around the fault where this earthquake occurred. Reliable phase unwrapping was not possible for the conventional DInSAR method.

A slightly modified Persistent Scatterer analysis with StaMPS was used in this case study. PS analysis was performed for the ascending and descending track separately. The 09/01/2018 scene was selected as the master image for ascending track and the 09/05 scene was selected as the master image for descending track. However, instead of getting the average LOS velocity map during the time span, the value from 08/20/2018 and 09/13/2018 for ascending track, 08/24/2018 and 09/17/2018 for descending track were extracted from the time series plots to get the co-seismic LOS displacement for all persistent scatterers. This is a workaround when phase unwrapping for the entire co-seismic interferogram is not possible. The co-seismic LOS displacement result for persistent scatterers on the descending track in the area near the fault is shown in Figure 5.2. One downside of this method is that the persistent scatterers from the ascending track and descending track are not at the same location, which makes 3D decomposition of the LOS displacement tricky. In this case study, the persistent scatters closest to the 12 locations in Figure 5.2 were picked manually for the ascending and descending track, and then 3D decomposition was performed at each location with the LOS displacement values of these persistent scatterers assuming there is no N-S displacement component. The vertical and E-W displacement components at these

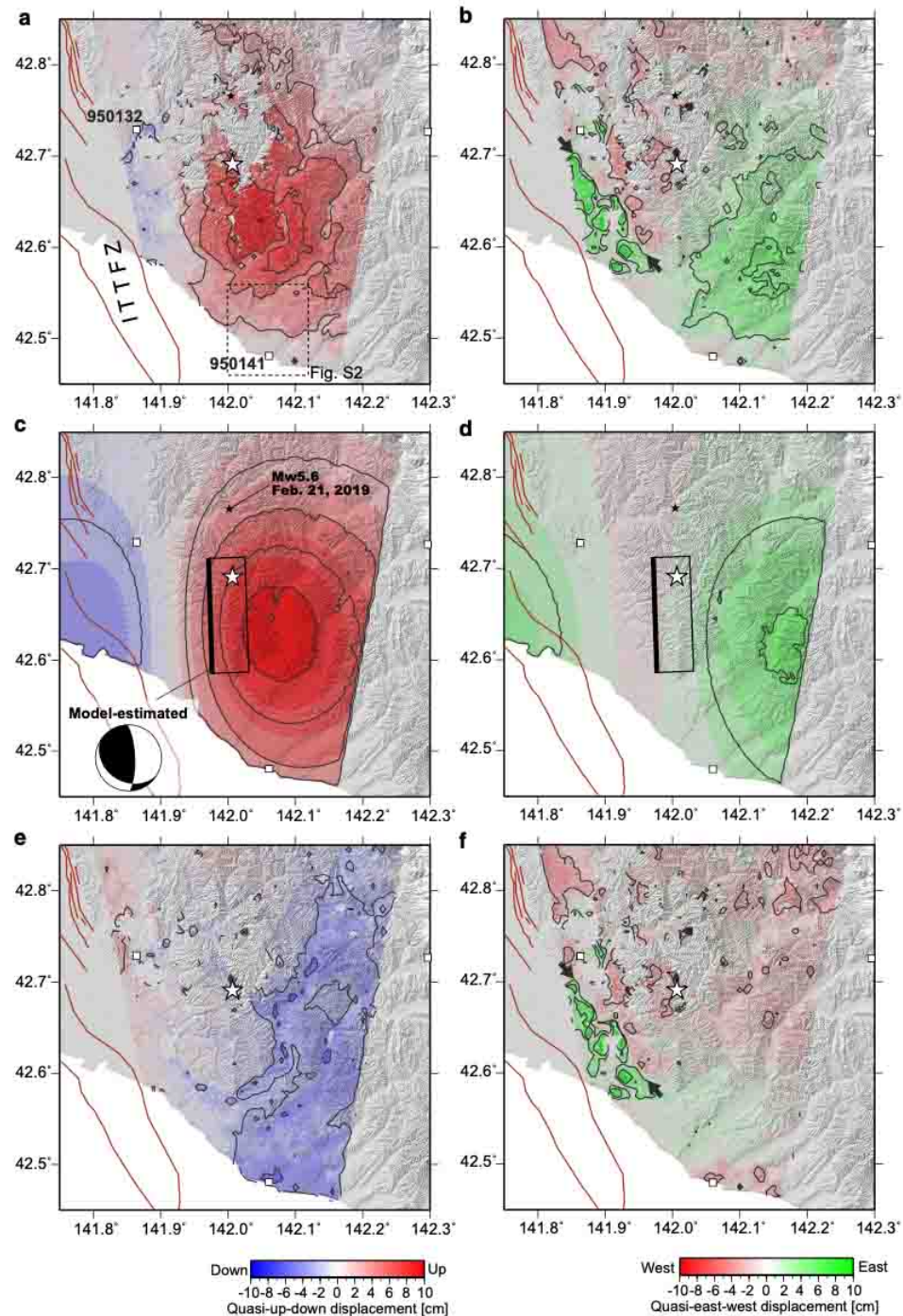


Figure 5.1: a and b show the vertical and E-W displacement maps derived from ALOS-2 data set. c and d show the vertical and E-W displacement maps predicted by the fault model. e and f show the residuals of the two displacement components. [44]

| Satellite | Time | Flight Direction | Band | Wavelength (cm) |
|-------------|------------|------------------|--------|-----------------|
| Sentinel-1B | 07/15/2018 | Ascending | C-Band | 5.6 |
| Sentinel-1B | 08/08/2018 | Ascending | C-Band | 5.6 |
| Sentinel-1B | 08/20/2018 | Ascending | C-Band | 5.6 |
| Sentinel-1B | 09/01/2018 | Ascending | C-Band | 5.6 |
| Sentinel-1B | 09/13/2018 | Ascending | C-Band | 5.6 |
| Sentinel-1B | 09/25/2018 | Ascending | C-Band | 5.6 |
| Sentinel-1B | 10/07/2018 | Ascending | C-Band | 5.6 |
| Sentinel-1B | 10/19/2018 | Ascending | C-Band | 5.6 |
| Sentinel-1B | 10/31/2018 | Ascending | C-Band | 5.6 |
| Sentinel-1B | 11/24/2018 | Ascending | C-Band | 5.6 |
| Sentinel-1A | 08/12/2018 | Descending | C-Band | 5.6 |
| Sentinel-1A | 08/24/2018 | Descending | C-Band | 5.6 |
| Sentinel-1A | 09/05/2018 | Descending | C-Band | 5.6 |
| Sentinel-1A | 09/17/2018 | Descending | C-Band | 5.6 |
| Sentinel-1A | 10/11/2018 | Descending | C-Band | 5.6 |
| Sentinel-1A | 10/23/2018 | Descending | C-Band | 5.6 |
| Sentinel-1A | 11/04/2018 | Descending | C-Band | 5.6 |

Table 5.1: SAR data sets used in the 2018 Kumamoto earthquake case study

12 locations are summarized in Table 5.2 and the plots are shown in Figure 5.3. Apart from location 6 that has slightly large vertical and E-W displacements, the results are consistent with the results derived from ALOS-2 data set and the fault model in Kobayashi et al. 2019 [44]. Therefore, this method indeed extracted useful information from the Sentinel-1A/B data set even with low coherence.

Liquefaction at the Port of Tomakomai

The JGS survey team observed sand boils at landfills, the uneven subsidence of road, and inclined sea revetment due to liquefaction everywhere at the outer periphery of the Tomato-Atsuma Thermal Electric Power Plant located in Tomakomai [36] (Figure 5.4). But the civil engineering structures inside the power plant had little serious damage due to the counter-measures against liquefaction taken at the foundation. [36]. The GEER field reconnaissance team observed minor settlement (typically 10 cm or less) and sand boils surrounding a light tower at the East Tomakomai Port after the largest section of liquefaction-damaged port facility pavement was removed [42] (Figure 5.5). The undeveloped field adjacent to the port facility had widespread sand boils noted via UAV surveying [42](Figure 5.5b). Sand boils were also observed on an undeveloped field where the Tomato-Atsuma Thermal Electric Power Plant was in sight (Figure 5.6).

Due to the lack of persistent scatterer in the area where sand boils due to liquefaction

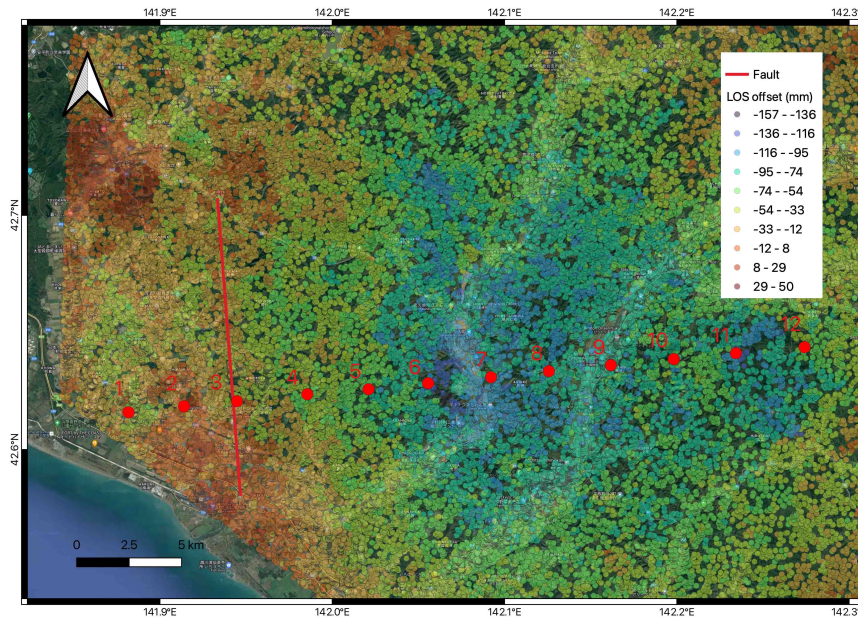


Figure 5.2: The co-seismic LOS displacement map for persistent scatterers on descending track (Positive displacement is moving away from the satellite.)

| Location | ASC LOS (mm) | DES LOS (mm) | Vertical (cm) | E-W (cm) |
|----------|--------------|--------------|---------------|----------|
| 1 | -31.4 | -26.9 | 3.66 | -0.47 |
| 2 | -14.6 | -11.6 | 1.64 | 0.30 |
| 3 | -11.8 | -26.3 | 2.44 | 1.13 |
| 4 | -26.5 | -68.6 | 6.11 | 3.30 |
| 5 | -54.9 | -86.5 | 9.00 | 2.29 |
| 6 | -46.6 | -149.0 | 12.67 | 8.00 |
| 7 | -23.9 | -97.6 | 7.92 | 5.79 |
| 8 | -22.6 | -88.6 | 7.26 | 5.15 |
| 9 | -12.4 | -83.9 | 6.36 | 5.64 |
| 10 | -9.8 | -74.7 | 5.61 | 5.11 |
| 11 | -37.9 | -111.3 | 9.72 | 5.58 |
| 12 | -35.6 | -59.7 | 6.11 | 1.64 |

Table 5.2: Co-seismic Vertical and E-W displacement from 3D decomposition at the 12 location in Figure 5.2 (Positive displacement is uplift and eastward displacement.)

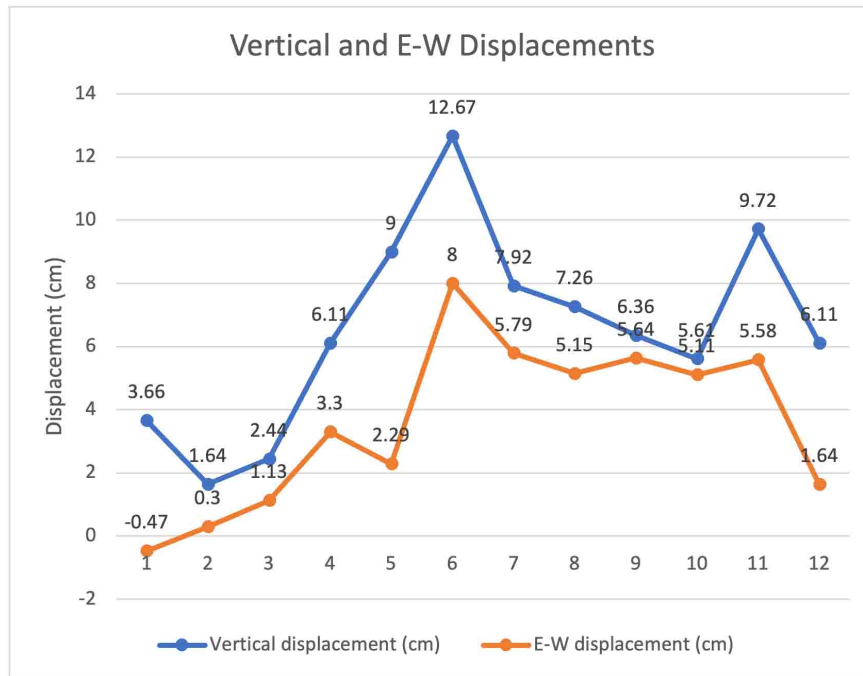


Figure 5.3: Co-seismic Vertical and E-W displacement plots from 3D decomposition at the 12 location in Figure 5.2 (Positive displacement is uplift and eastward displacement.)



Figure 5.4: Uneven subsidence of road due to liquefaction with sand boiling in Tomakomai (photo taken by Watabe, Y., Hokkaido Univ.)



(a)



(b)

Figure 5.5: (a) Minor settlement of concrete slabs. (b) Sand boils surrounding a light tower. Sand boils near the southern seawall and in the container backyard. Sand boils in the undeveloped area between the marine container facility and the HEPCO coal plant.(photos taken by the GEER field reconnaissance team [42])

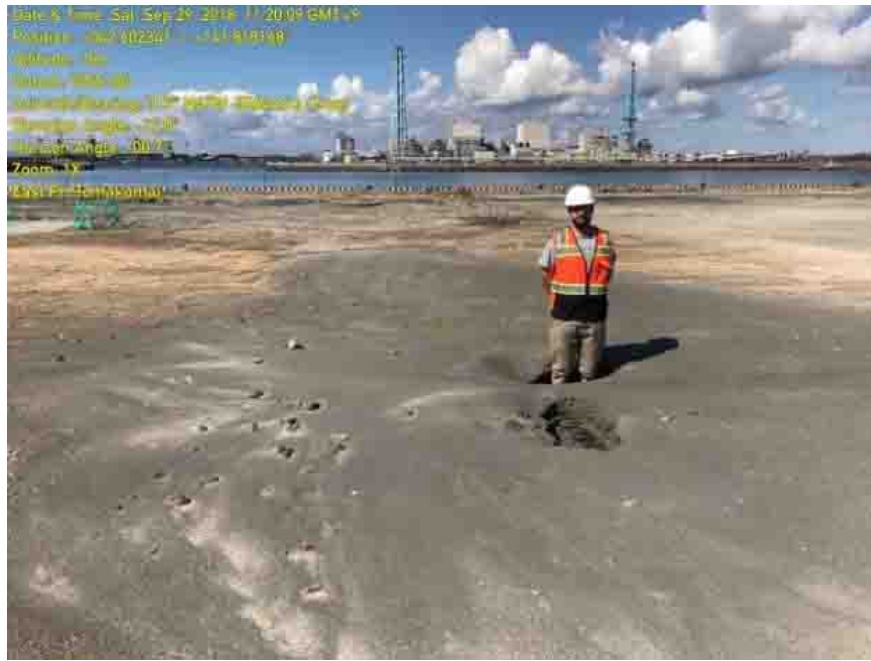


Figure 5.6: Sand boils in an undeveloped area where Tomato-Atsuma Thermal Electric Power Plant is in sight (photo taken by the GEER field reconnaissance team [42])

occurred, coherence-change method was selected to analyze liquefaction in this case study. The Sentinel-1A data set used for the coherence-change analysis is summarized in Table 5.3. As discussed in Chapter 4, the key to coherence-change method is the normalized coherence change threshold. 0.35 was set as the threshold for the study in Tomakomai and the normalized coherence change map in Tomakomai is shown in Figure 5.7. The area circled in blue circle at the bottom left of the map is where the minor settlement and sand boils in Figure 5.5 were observed. The undeveloped field bounded in red lines adjacent to the port facility on the map is where widespread sand boils were found by UAV surveying. The Tomato-Atsuma Thermal Electric Power Plant on the map does not have pixel with normalized coherence change larger than 0.35, which is consistent with the field observation that little serious damage occurred to the civil engineering structure in the power plant. The three areas with large normalized coherence change on the road adjacent to the power plant and the coal plant are where the sand boils and uneven road settlement shown in Figure 5.4 occurred. The blue circle at the bottom right of the map again shows large normalized coherence change in the area where sand boils in Figure 5.6 occurred. Overall, the results from the coherence-change method are consistent with the field observations at the port of Tomakomai.

| Satellite | Time | Flight Direction | Band | Wavelength (cm) |
|-------------|------------|------------------|--------|-----------------|
| Sentinel-1A | 08/24/2018 | Descending | C-Band | 5.6 |
| Sentinel-1A | 09/05/2018 | Descending | C-Band | 5.6 |
| Sentinel-1A | 09/17/2018 | Descending | C-Band | 5.6 |

Table 5.3: SAR data sets used in the coherence-change analysis

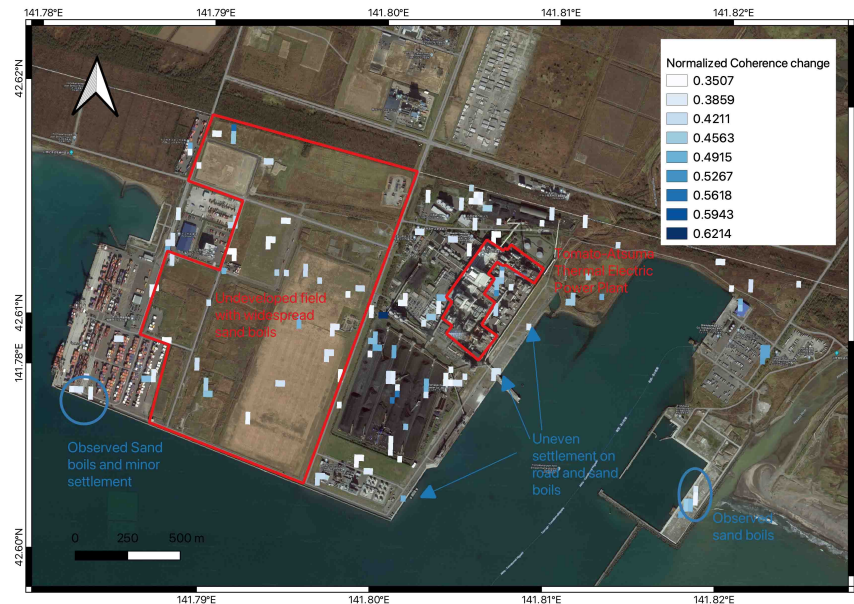


Figure 5.7: Normalized coherence change map in Tomakomai

Liquefaction of levees near Mukawa Town

The GEER field reconnaissance team observed blue tarps on top of the flood control levees north of Mukawa along the river that covered longitudinal cracks and vertical offsets [42]. Japanese researchers identified sand boils along the levee on the river side (Figure 5.8).

Coherence-change method was used in this case as well. The normalized coherence change map in Mukawa is shown in Figure 5.9. 0.35 was selected as the normalized coherence change threshold again. The area in orange circle is where the Japanese researchers observed sand boils. The areas in blue circles are consistent with the locations of the blue tarps found on the aerial photo taken in September 2018 in Google Earth (Figure 5.10). However, there are areas with large normalized coherence change in the Mukawa town to the west of the Mukawa River and the agricultural fields to the east of the Mukawa River. These areas are generally covered by vegetation without evidence of liquefaction in the field. Therefore, the vegetation affects the effectiveness of coherence-change method in identifying liquefaction damaged areas near the Mukawa River.



Figure 5.8: Sand boils observed by Japanese researchers (left). Blue tarps on top of the flood control levee (right). (photos taken by the GEER field reconnaissance team [42])

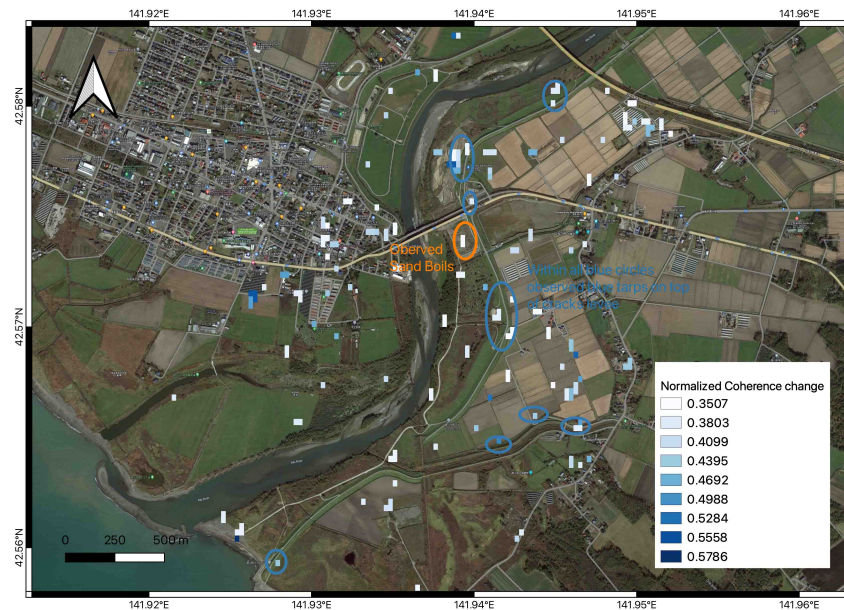


Figure 5.9: Normalized coherence change map in Mukawa

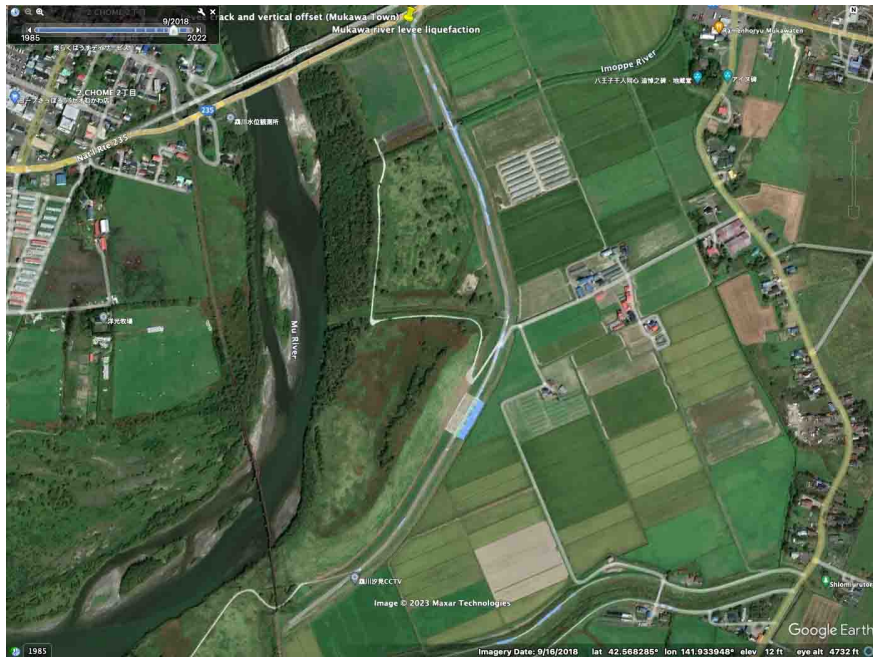


Figure 5.10: Blue tarps on top of the levee found on Google Earth image taken in September 2018

Flow liquefaction in Satozuka, Sapporo City

Volumetric collapse or liquefaction of pumice backfill below the area of Satozuka in Sapporo City led to a destructive flow slide [42]. The GEER field reconnaissance team observed widespread evidence of vertical displacements, damages to structures, roadways, and pipelines even though most of the flow-failure deposits had been removed by the time of the reconnaissance (Figure 5.11) [42]. Apart from the flow failure in Satozuka, the JGS survey team also found liquefaction damage in Kiyota 6-7 and Utsukushigaoka [36].

The three areas with liquefaction damage are marked on the normalized coherence change map in Figure 5.12. Unlike the liquefaction case study in Kumamoto City, the normalized coherence change is considerably smaller in Sapporo City. As a result, the normalized coherence change threshold can be lowered from 0.35 to 0.3. The coherence-change method really shines in this case study because the area with flow-failure in Satozuka and the other two areas with liquefaction damage in Kiyota and Utsukushigaoka have significant larger normalized coherence change than their surrounding neighborhoods.

Liquefaction damage along subway lines in Sapporo City

The JGS survey team observed severe liquefaction induced settlement of the road above the Namboku subway line around Kita 34 Station and the Toho subway line along the Higashi



(a)



(b)

Figure 5.11: (a) Head scarp of the flow-failure (b) Older building with mat foundation on the left and contemporary building with pile foundation on the right. Structures' performance highly depends on foundation design. (photos taken by the GEER field reconnaissance team [42])



Figure 5.12: Normalized coherence change map in Sapporo City where flow-failure occurred (Liquefaction-damaged areas bounded in blue lines are from Ishikawa et al. 2021 [36])

15-chome Tonden street in Sapporo City [36]. The liquefaction damaged area above the Namboku subway line is shown in Figure 5.13. The photos taken at the numbered locations in Figure 5.13 two days after the earthquake are shown in Figure 5.15. Majority of the damage was ground settlement on the Sapporo Shindo drive above the Namboku subway line. The liquefaction damage situation along the Higashi 15-chome Tonden street above the Toho subway line is shown in Figure 5.14. The photos taken at the numbered location in Figure 5.14 two days after the earthquake are shown in Figure 5.16. At location 5 and 6, large-scale road settlement was observed with up to 1 m of settlement and exposed buried structure. At location 7, medium-scale road settlement and long cracks along the road were observed. At location 8-10, large-scale road collapse and inclination of road signs were observed. There were also traces of sand boils. Further to the south, small-scale road settlement and sand boils were observed [36]. In general, the liquefaction damage along the Higashi 15-chome Tonden street above the Toho subway line includes road settlement at different scales and sand boils. Ishikawa et al. 2021 [36] proposed that the damage on the roads was caused by the liquefaction of the backfill soil (purchased clean sand) that was used for the subway construction based on the shallow ground water level (less than 3 m) and the column diagrams near the affected area from the Geological and Geotechnical Information Database G-Space II in Japan.

The normalized coherence change map in this area with field observed liquefaction-damaged areas bounded by blue rectangles is shown in Figure 5.17. Normalized coherence change larger than 0.3 is present at all locations with field observed liquefaction damage,

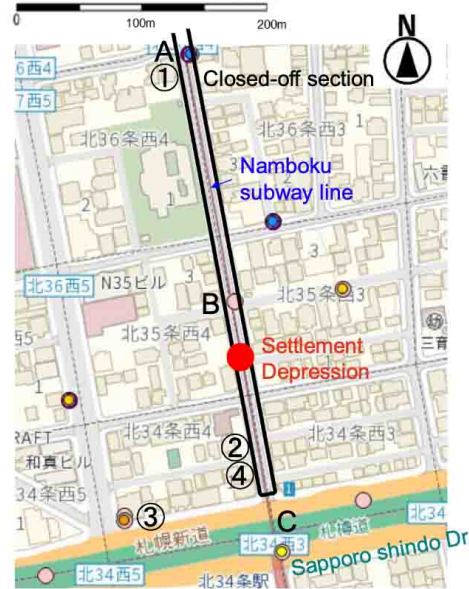


Figure 5.13: Liquefaction damaged area above the Namboku subway line [36])

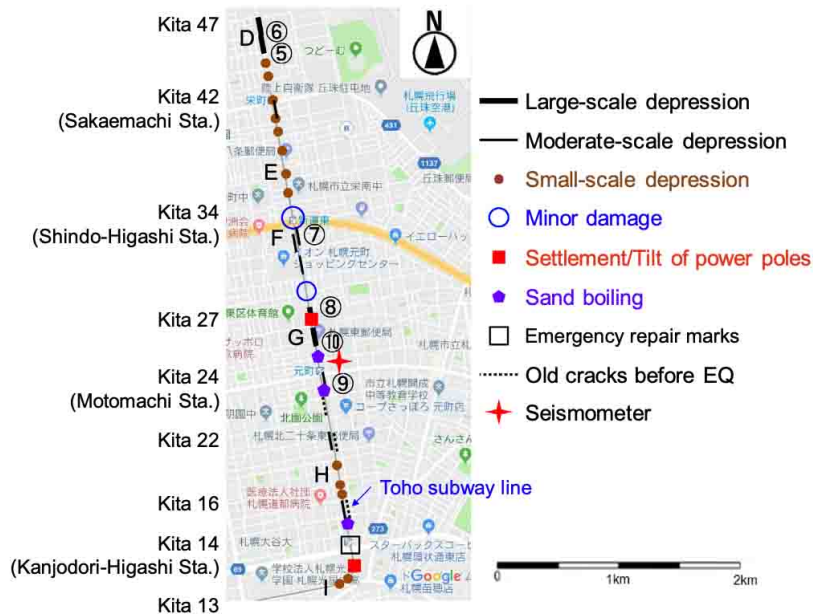


Figure 5.14: Liquefaction damaged area above the Toho subway line [36])

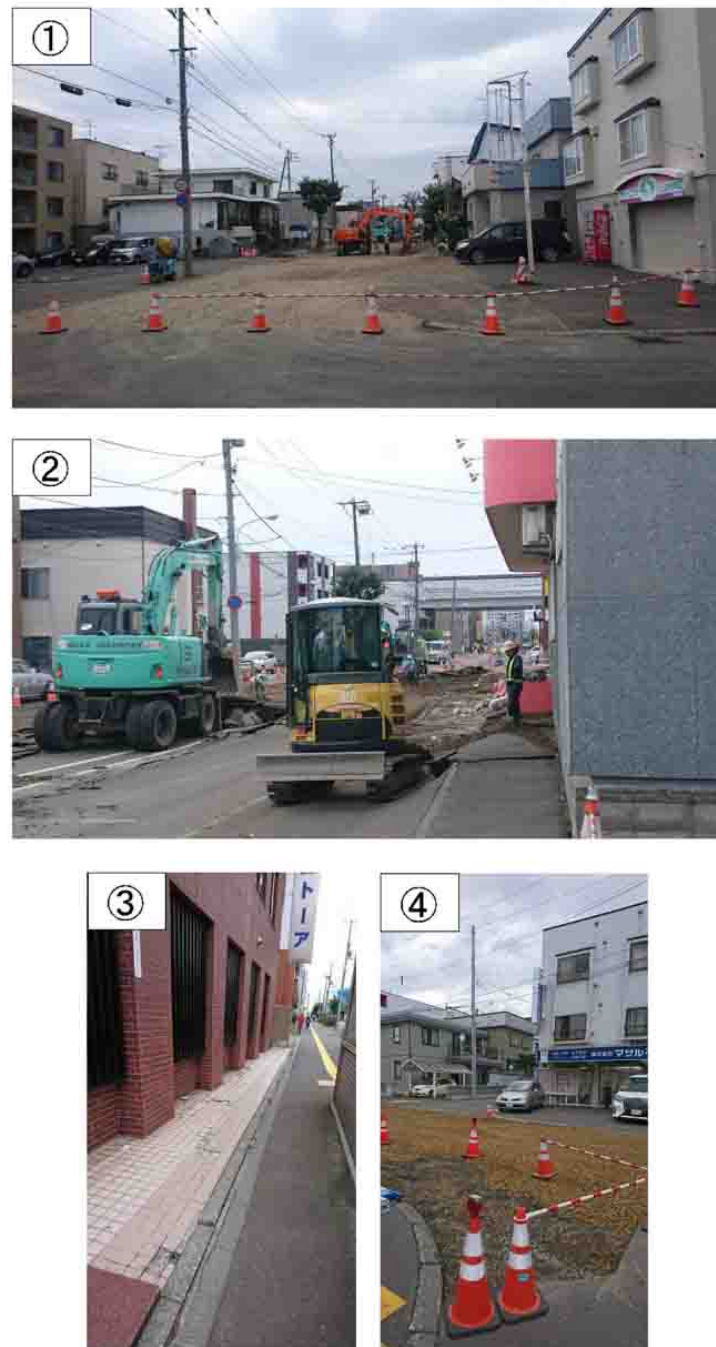


Figure 5.15: Situation near Kita 34 Station two days after the earthquake (location corresponds to the number in Figure 5.13) [36]

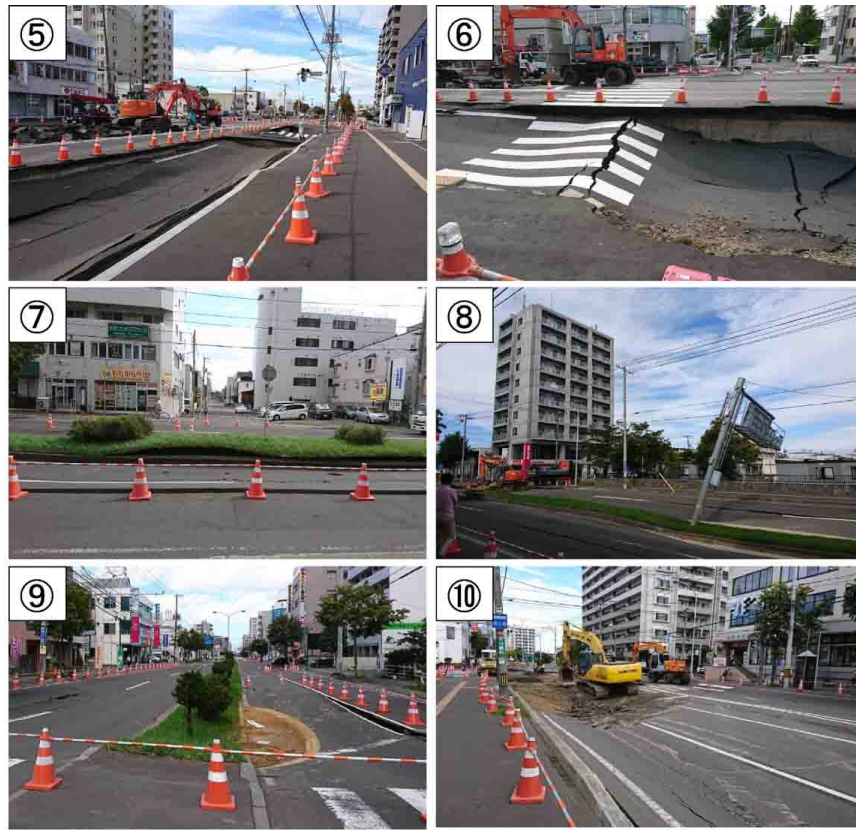


Figure 5.16: Situation along the Higashi 15-chome Tonden street two days after the earthquake (location corresponds to the number in Figure 5.14) [36])

which further proves the effectiveness of coherence-change method at identifying liquefaction damage. There is one more question about this case, can the PS analysis result reveal the road settlement above the subway lines when persistent scatter density is sufficient in urban area? The vertical displacements from 3D decomposition at the locations with settlement in Figure 5.13 and Figure 5.14 are summarized in Table 5.4. Two cm of settlement is way smaller than the smallest scale settlement observed in this area. Therefore, PS analysis with Sentinel-1A/B data set is not suitable for resolving localized settlements on the road.

Landslides in Atsuma and Abira

The 2018 Hokkaido earthquake triggered over 6000 landslides in Atsuma and Abira, and 36 human lives were lost due to those landslides [70, 78]. As discussed in Chapter 4, the pixel (dense) offset method is useful for revealing large displacement in a short period of time. However, since ALOS-2 data set was not accessible for this case study, C-Band Sentinel-1A/b data set was used to perform the pixel offset analysis. There is one problem for

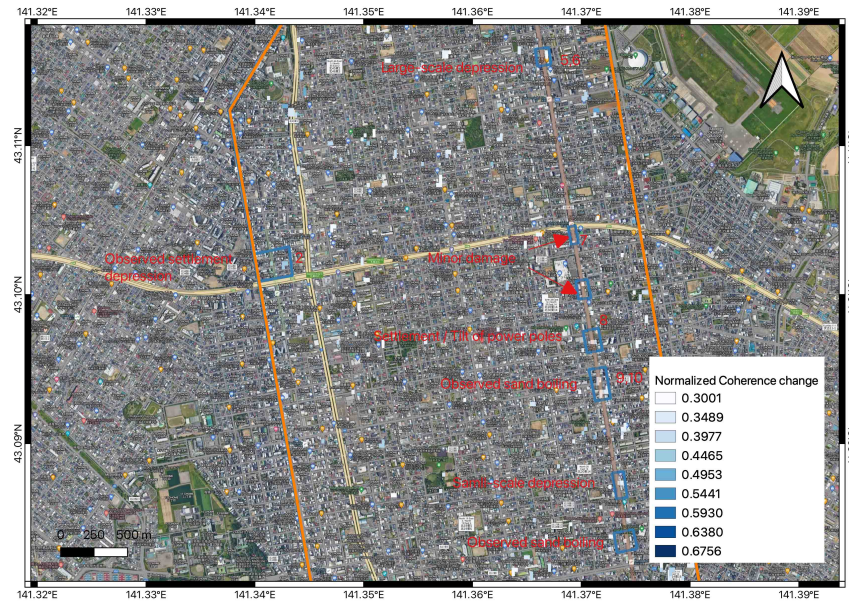


Figure 5.17: Normalized coherence change map of the area with liquefaction damage on roads above subway lines

| Location | ASC LOS (mm) | DES LOS (mm) | Vertical (cm) |
|-------------------|--------------|--------------|---------------|
| Kita 34 | 24.6 | 4.7 | -1.83 |
| Kita 47 - Kita 42 | 19.7 | 9 | -1.81 |
| Kita 42 - Kita 34 | 23.7 | 6.1 | -1.87 |
| Kita 34 - Kita 27 | 18.2 | 6.3 | -1.54 |
| Kita 27 - Kita 24 | 24.2 | 6.2 | -1.90 |
| Kita 16 | 28.0 | 2.4 | -1.89 |
| Kita 13 | 20.1 | 2.5 | -1.41 |

Table 5.4: Vertical displacement from the PS analysis result at the locations with settlement in Figure 5.13 and Figure 5.14 (Settlement is negative.)

the Sentinel-1A/B data set in this analysis. The pixel width in the azimuth direction is 14 m for Sentinel-1A/B compared to the 2.34 m for ALOS-2, which means Sentinel-1A/B has significantly worse resolution in the azimuth direction than ALOS-2. The pixel offset analysis for Kumamoto case study in Chapter 4 has ALOS-2 data set on descending track available. Therefore, azimuth pixel offset with Sentinel-1A data set is not required for the 3D decomposition of the displacement. But for Hokkaido, at least one azimuth pixel offset with Sentinel-1A/B data set on either ascending track or descending track is required. This is not ideal because even small azimuth offset can cause huge change in the N-S displacement component. The landslides in Yoshino village and Tomisato village were selected to test whether the pixel offset method with Sentinel-1A/B data set works in mapping landslides caused by the earthquake.

The landslide in the south of Yoshino village is shown in Figure 5.18a. The sliding body buried the houses at the foot of the slope and caused the death of 36 residents. The elevation of the slope was about 60 m with a 27-degree slope angle. The width of the translational earth slide was 300 m and the surface soil was approximately 3 m of pumice. The deposit soil at the foot of the slope has a high water content close to saturation [78]. The landslide in the north of Yoshino village shown in Figure 5.18b caused no casualties but structures and roads were buried. The mechanism of this landslide is similar to that at the south of Yoshino village with a sliding width of 700 m [78]. The landslide at a water treatment plant in Tomisato village is shown in Figure 5.18c. The elevation of the slope was about 50 m with a 21-degree slope angle. The water tower and buildings of the water treatment plant were buried by the deposit but did not collapse, which indicates the impact force of the slide mass was not significant [78].

The vertical displacement map derived from the pixel offset analysis is shown in Figure 5.19. Horizontal and vertical displacements at ten locations on the sliding surface are marked on the map (Vertical displacements are in parentheses.). The horizontal and vertical displacements at these 10 locations cannot represent the movement of the sliding body or the change of slope surface. This means not only the azimuth pixel offset from Sentinel-1A/B data set makes the N-S displacement component unstable, the large displacement of the sliding body also makes finding matching pixels between the co-seismic pair of satellite images by cross-correlation overly difficult. As a result, the pixel offset method with Sentinel-1A/B data set is not suitable for mapping landslides displacements caused by the 2018 Hokkaido earthquake.

5.4 Discussion

Persistent Scattering analysis with low coherence Sentinel-1A/B data set is capable of revealing the centimeter-scale ground displacement near the fault ruptured in the 2018 Hokkaido earthquake. This is because the displacement in this region is relatively small (within 10 cm) and the StaMPS method can achieve decent persistent scatterer density in mountainous areas. However, PS analysis cannot show the localized road settlement above the subway

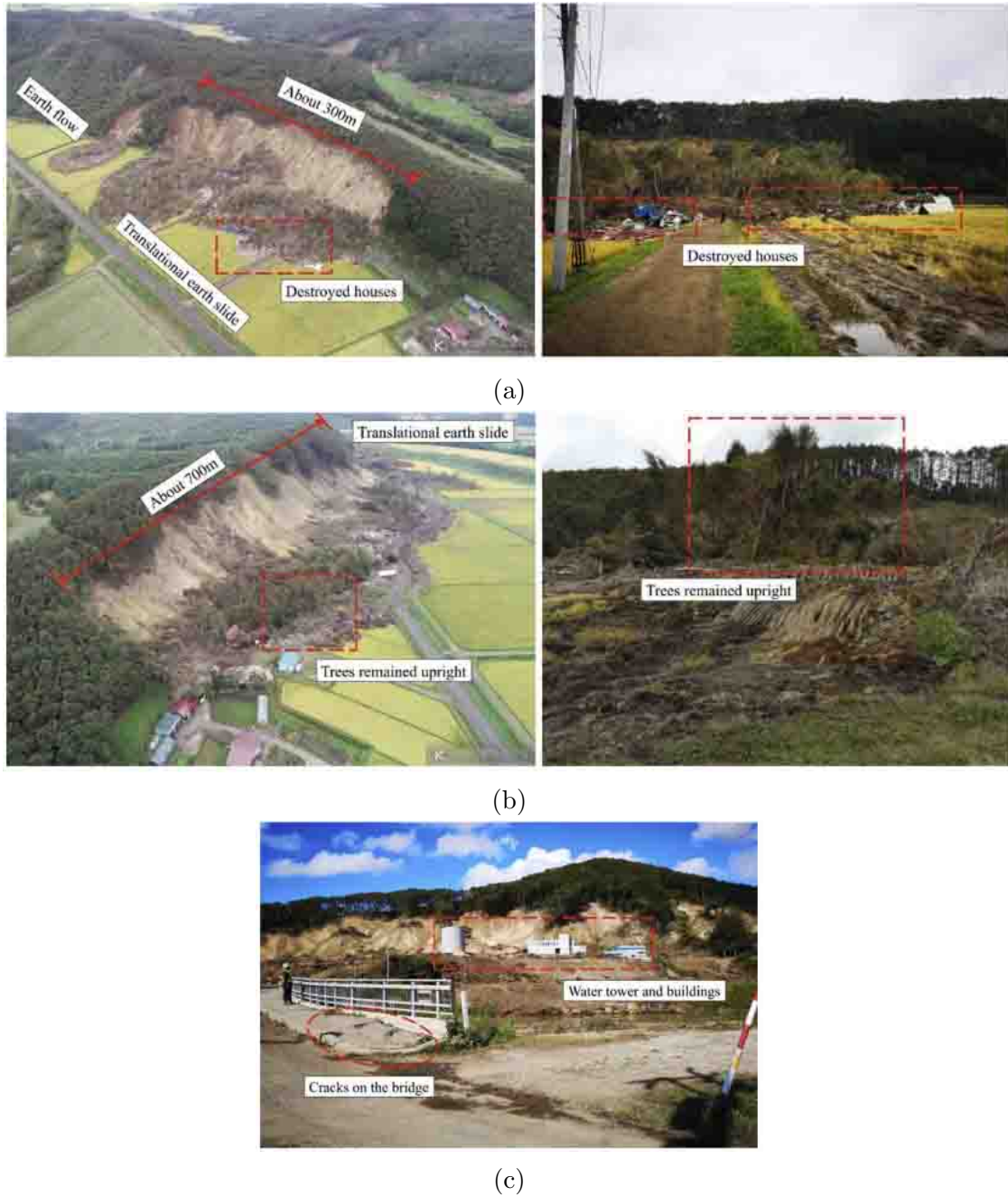


Figure 5.18: (a) Landslide in Yoshino village (south) (b) Landslide in Yoshino village (north) (c) Landslide in Tomisato village (water treatment plant [78])

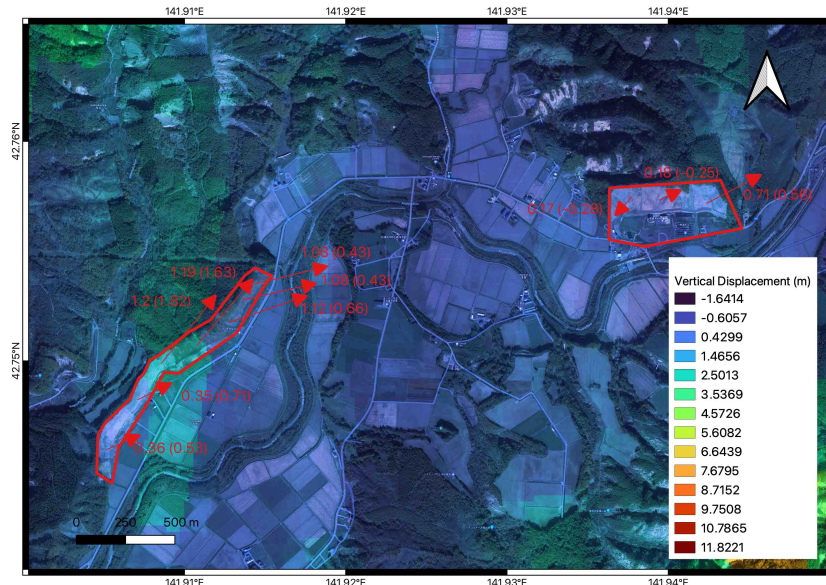


Figure 5.19: Vertical displacement map derived from the pixel offset analysis of Yoshino village and Tomisato village (Horizontal displacement and vertical displacement in parentheses are labeled at 10 locations on the sliding surface.)

lines in Sapporo City. Because the PS analysis result does not have enough resolution due to the small persistent scatterer density on the road. Also the up to 1 m vertical offset at some locations is way too large for C-Band radar with 5.6 cm wavelength.

Coherence-change method performs well in identifying the sand boils in Tomakomai, the liquefaction damage on the flood control levee in Mukawa, the flow liquefaction in Satozuka, and the liquefaction induced settlement and sand boils along the roads above subway lines in Sapporo City. However, the coherence-change method is not suitable for identifying liquefaction damage in Mukawa due to the fact that some other areas with vegetation also have large normalized coherence change even though there is no evidence of liquefaction in the field. Different normalized coherence change thresholds were used in Sapporo City, and the rural areas like Tomakomai and Mukawa. Which further proves the importance of finding the optimum threshold for different locations and data sets.

Pixel offset method with Sentinel-1A/B data set completely fails at mapping the displacement of landslides caused by the earthquake. There are two possible reasons: 1. The low resolution of the azimuth pixel offset result from Sentinel-1A/B data set makes the N-S displacement component derived from the pixel offset result unstable; and, 2. It is too difficult for cross correlation method to find matching pixels on the sliding body of shallow landslides between the co-seismic pair of satellite images.

Chapter 6

Conclusion and future work

6.1 Conclusions on the effectiveness of the four InSAR analysis methods on earthquake-induced liquefaction analysis

After testing the four InSAR analysis methods introduced in Chapter 2 in the three case studies, the following conclusions can be drawn regarding the effectiveness of each method:

- The effectiveness of the conventional Differential InSAR (DInSAR) method highly depends on the characteristics of the displacement it tries to recover. The meter scale Greendale fault movement and the decimeter scale Port Hills fault movement in the Canterbury case study (Chapter 3) can be successfully revealed by DInSAR method with L-Band ALOS-1 data set (22.9 cm wavelength) for two reasons: 1. The Greendale fault movement is almost in the E-W direction and the majority of the Port Hills fault movement is in the vertical direction. DInSAR method has low sensitivity to the displacement in N-S direction because it cannot detect the displacement in the azimuth direction without additional operations. Therefore, the Futagawa fault rupture and the lateral displacement in Aso Valley in the Kumamoto case study (Chapter 4) are not ideal to analyse with DInSAR method because both displacements have large components in the N-S direction; and, 2. The scale of the displacement and the size of the region where the displacement occurred are within the capability of L-Band ALOS-1 data set. The length of the Greendale fault and the Port Hills fault traces are both over 10 km, which means the width of the color fringes that represent meter scale displacement with L-Band data set on the interferogram is big enough to be recognized by phase unwrapping algorithms. Thus, correct displacement in the LOS direction can be recovered. The lateral spreading displacement along the Avon River and in Kaiapoi (Chapter 3) are in the meter scale on river banks that are less 500 m wide. The color fringes in these areas on the interferogram are compressed and then the detailed fringes will be smoothed out by the filtering of the interferogram before

phase unwrapping. As a result, much smaller LOS displacement will be output from phase unwrapping algorithms. Even worse, large displacement in a small area can cause decorrelation, which makes phase unwrapping impossible. In addition, DInSAR method is not suitable for analyzing overly localized displacement like the differential settlements of the buildings in the Christchurch CBD caused by the 2011 Christchurch earthquake (Chapter 3). Because the DInSAR analysis result does not have enough resolution due to the pixel spacing and the pixel size of the SAR image.

- The pixel offset method is excellent for analysing large displacement in a short period of time. And it can output displacement in two directions (the range and azimuth direction), which makes the 3D decomposition of displacements much easier because one pixel offset result on the ascending track and another on the descending track can provide 4 known displacement components that are more than enough to solve the three unknown displacement components in the E-W, N-S and vertical direction. There is one downside of this method: pixel offset method can only output displacement in the unit of pixel. Therefore, the resolution of pixel offset method highly depends on the pixel size of SAR images. ALOS-2 has pixel size of 1.43 m by 2.34 m in the range and azimuth direction. Sentinel-1A/B has pixel size of 2.5 m by 14 m in the range and azimuth direction. The general consensus is that pixel offset method has resolution up to 1/10th of a pixel. ALOS-2 data set is great for pixel offset analysis due to the high resolution in both range and azimuth direction. However, the azimuth offset from Sentinel-1A/B data set should be avoided. The hybrid pixel offset analysis with range offset from Sentinel-1A on ascending track, range and azimuth offset from ALOS-2 on descending track is capable of revealing the Futagawa fault offset and the lateral displacement in Aso Valley in the Kumamoto case study (Chapter 4). However, the pixel offset analysis using only Sentinel-1A/B data set completely failed in mapping the displacement of landslides caused by the 2018 Hokkaido earthquake (Chapter 5). On the one hand, small azimuth offset with Sentinel-1A/B data set can heavily affect the N-S component of the displacement. On the other hand, the huge and chaotic landslides displacement might create a big challenge for cross correlation method to find matching pixels between the co-seismic pair of SAR images.
- The coherence-change method is a great option for identifying liquefaction damage, because sand boils, lateral spreading, ground settlement and flow failures can all cause large coherence loss from a pre-seismic interferogram to a co-seismic interferogram. It also requires the least amount of computing resources because no phase unwrapping of interferogram or template matching with cross correlation is needed. Coherence-change method achieved excellent results in both rural areas (Aso Valley in Chapter 4, and Port of Tomakomai, Mukawa in Chapter 5) and urban areas (Kumamoto City in Chapter 4 and Sapporo City in Chapter 5). The key to coherence-change method is the normalized coherence change threshold. This threshold can vary at different locations and with difference SAR data sets. For the case studies in this thesis, the threshold

is calibrated based on the field observed liquefaction-damaged areas. However, it can be tricky to find the optimum threshold in real life application when prior information about field observed liquefaction is not available. One potential solution is to find some locations with liquefaction damage in high probability by the identification of liquefaction signs (sand boils, ground cracks parallel to rivers etc.) on aerial images and the existing liquefaction triggering analysis ahead of the field reconnaissance, and then the normalized coherence change threshold can be calibrated based on these locations. The coherence-change analysis result can then provide useful guidance to field reconnaissance teams on where to find liquefaction damage.

- The persistent scattering analysis can generate time series displacement plots for persistent scatterers when the coherence is too low for phase unwrapping the entire interferogram. Persistent scattering analysis with Sentinel-1A/B data set revealed the ground displacement near the epic center of the 2018 Hokkaido earthquake (Chapter 5) where the vertical and E-W displacement on the ground surface were less than 10 cm. However, the same analysis failed to recover the server road settlement on top of the Namboku and Toho subway lines in Sapporo City (Chapter 5). First of all, PS analysis cannot recover displacement beyond the capability of C-Band Sentinel-1A/B data set. Phase unwrapping algorithms cannot count the fringes between persistent scatterers on interferograms if the density of the persistent scatterers is not high enough, which causes the underestimate of displacements. Secondly, large local deformation can cause the absence of persistent scatterers due to low coherence and phase instability. In addition, the 3D decomposition of displacements with PS analysis is tricky because the locations of persistent scatterers are different between the ascending track and the descending track. Now, with ARIA tool and MintPy gaining popularity, short baseline method (SBAS) is preferred for time series analysis when high quality SAR data set is available. But neither of the two Japan case studies in this thesis has ARIA GUNW product available. That is why PS analysis was selected for the Hokkaido case study (Chapter 5).

6.2 InSAR workflow for analysing earthquake-induced liquefaction

Based on the conclusions of these studies, the InSAR workflow for earthquake induced liquefaction analysis was constructed as shown in Figure 6.1. The details on how to perform these analysis are included in Appendix A.

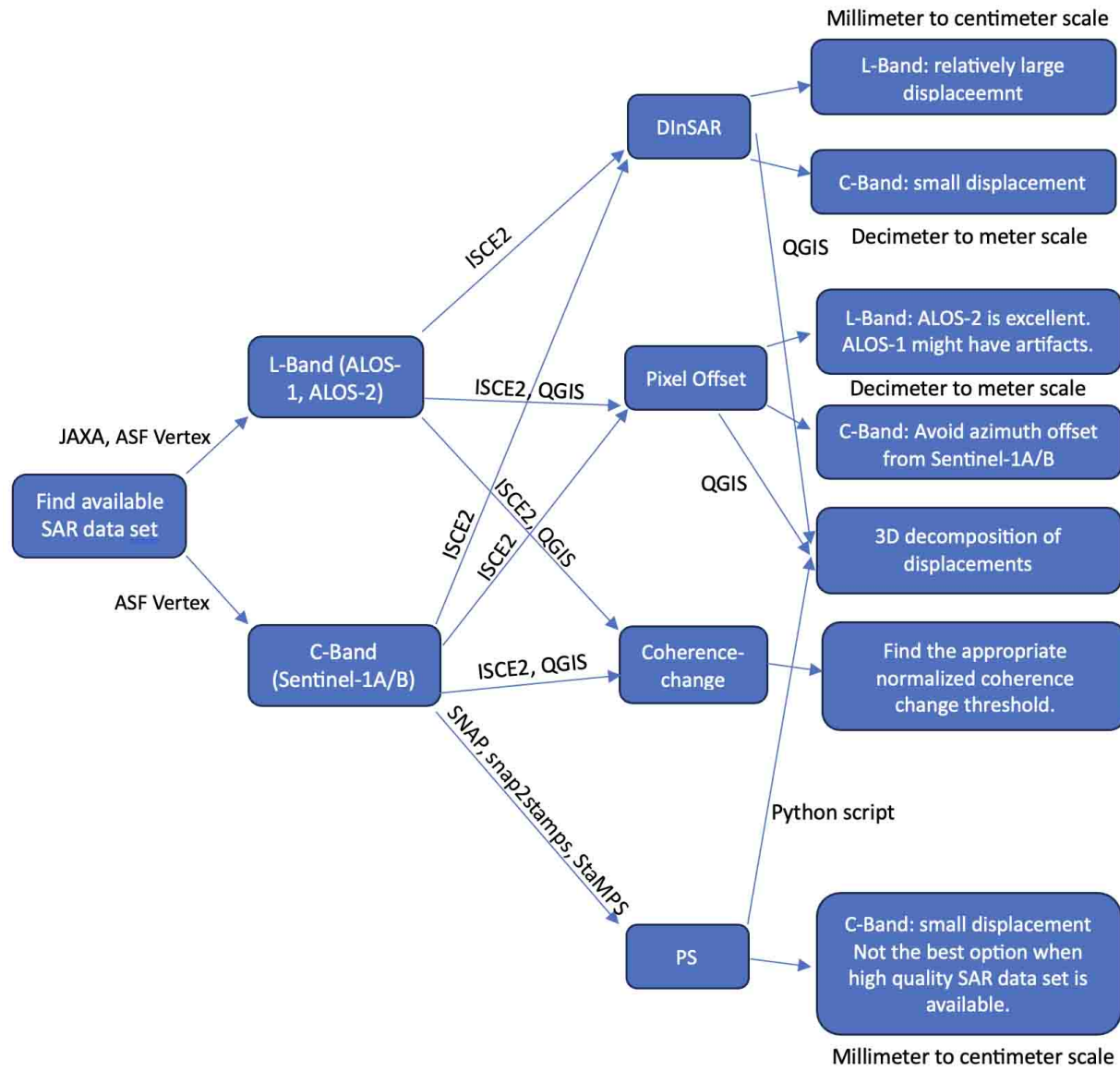


Figure 6.1: InSAR workflow for earthquake induced liquefaction analysis (ISCE2 is the second iteration of the InSAR Scientific Computing Environment developed by JPL.)

6.3 Future work

The biggest shortcoming of this thesis is that the short baseline time series analysis (SBAS) with ARIA tool and MintPy was not tested for earthquake induced liquefaction analysis because the ARIA GUNW product is not available for either the Kumamoto case study or the Hokkaido case study. ARIA GUNW product is an open-source standardized InSAR displacement product derived from Sentinel-1 SAR data and packaged as netCDF4 files [3]. Its compact size solves the memory issue of time-series analysis with a large number of interferograms. Since it is already a displacement product of SAR image pairs, no InSAR processing is required for time series analysis. ARIA tool provides the functionality of downloading and processing ARIA GUNW products and generates outputs that are compatible with third-party time-series InSAR packages like "Miami InSAR Time-series software in Python" (MintPy) [7]. MintPy is an open-source package for InSAR time-series analysis with small baseline method (SBAS) [75]. Both ARIA tool and MintPy are designed to work within the InSAR Scientific Computing Environment (ISCE). Therefore, it is recommended as a good practice to analyse an earthquake with liquefaction damage using the ARIA GUNW products available in the near future.

The NASA-ISRO SAR (NISAR) Mission is planned to launch in 2024 (Figure 6.2). As the next chapter of SAR mission, NISAR has the following advantages:

- It will be the first radar in space to have two radar frequencies (L-Band: 24 cm wavelength operated by NASA, S-Band: 9 cm wavelength operated by ISRO) which is excellent for monitoring ground displacements in different scales.
- It will observe Earth, land and ice-covered surfaces globally with 12-day return period on both the ascending track and the descending track.
- All of its data sets will be free and open.

Currently, the third iteration of InSAR Scientific Computing Environment (ISCE3) to work with NISAR products is in the works. This marks the standardization of InSAR analysis workflow in the near future. Which means it will be easier to learn by researchers with different backgrounds globally. NISAR will certainly bring new life to InSAR research. It is exciting to look forward to work with NISAR data sets and the new ISCE3 framework starting from next year.



Figure 6.2: Artist Rendering of NISAR from NISAR official website

Bibliography

- [1] Donald J. Anderson et al. “The Over-Prediction of Seismically Induced Soil Liquefaction during the 2016 Kumamoto, Japan Earthquake Sequence”. en. In: *Geosciences* 13.1 (Jan. 2023). Number: 1 Publisher: Multidisciplinary Digital Publishing Institute, p. 7. ISSN: 2076-3263. DOI: 10 . 3390/geosciences13010007. URL: <https://www.mdpi.com/2076-3263/13/1/7>.
- [2] Donald Jared Anderson. “Understanding Soil Liquefaction of the 2016 Kumamoto Earthquake”. MA thesis.
- [3] David P. Bekaert et al. “Development of open-access Standardized InSAR Displacement Products by the Advanced Rapid Imaging and Analysis (ARIA) Project for Natural Hazards”. In: *AGU fall meeting abstracts*. Vol. 2019. 2019, G23A-04.
- [4] S. Bhattacharya et al. “Geotechnical and infrastructural damage due to the 2016 Kumamoto earthquake sequence”. en. In: *Soil Dynamics and Earthquake Engineering* 104 (Jan. 2018), pp. 390–394. ISSN: 0267-7261. DOI: 10 . 1016 / j . soildyn . 2017 . 11 . 009. URL: <https://www.sciencedirect.com/science/article/pii/S0267726116304067>.
- [5] L. J. Brown et al. “Geology of Christchurch, New Zealand”. In: *Environmental and Engineering Geoscience* 1.4 (1995). Publisher: GeoScienceWorld, pp. 427–488.
- [6] Lennard James Brown and John Howard Weeber. “Geology of the Christchurch urban area”. In: (1992).
- [7] Brett Buzzanga et al. “Toward Sustained Monitoring of Subsidence at the Coast Using InSAR and GPS: An Application in Hampton Roads, Virginia”. en. In: *Geophysical Research Letters* 47.18 (2020), e2020GL090013. ISSN: 1944-8007. DOI: 10 . 1029 / 2020GL090013. URL: <https://onlinelibrary.wiley.com/doi/abs/10.1029/2020GL090013>.
- [8] Curtis W. Chen and Howard A. Zebker. “Network approaches to two-dimensional phase unwrapping: intractability and two new algorithms”. In: *JOSA A* 17.3 (2000). Publisher: Optica Publishing Group, pp. 401–414.

- [9] Curtis W. Chen and Howard A. Zebker. "Phase unwrapping for large SAR interferograms: Statistical segmentation and generalized network models". In: *IEEE Transactions on Geoscience and Remote Sensing* 40.8 (2002). Publisher: IEEE, pp. 1709–1719.
- [10] Curtis W. Chen and Howard A. Zebker. "Two-dimensional phase unwrapping with use of statistical models for cost functions in nonlinear optimization". In: *JOSA A* 18.2 (2001). Publisher: Optica Publishing Group, pp. 338–351.
- [11] Brady R. Cox et al. "Liquefaction at strong motion stations and in Urayasu City during the 2011 Tohoku-Oki earthquake". In: *Earthquake Spectra* 29.1_suppl (2013). Publisher: SAGE Publications Sage UK: London, England, pp. 55–80.
- [12] Michele Crosetto et al. "Deformation monitoring using remotely sensed radar interferometric data". In: *11th FIG Symposium on Deformation Measurements, Patras Univ., Santorini, Greece*. 2003.
- [13] M Cubrinovski et al. "Lateral spreading and its impacts in urban areas in the 2010–2011 Christchurch earthquakes". In: *New Zealand Journal of Geology and Geophysics* 55.3 (Sept. 2012), pp. 255–269. ISSN: 0028-8306. DOI: 10.1080/00288306.2012.699895.
- [14] M. Cubrinovski. "Geotechnical Reconnaissance of the 2011 Christchurch, New Zealand Earthquake". In: (2011). Publisher: GEER Association. DOI: 10.18118/G68G65. URL: http://geerassociation.org/component/geer_reports/?view=geerreports&id=41&layout=default.
- [15] Misko Cubrinovski et al. "Soil Liquefaction Effects in the Central Business District during the February 2011 Christchurch Earthquake". In: *Seismological Research Letters* 82.6 (Nov. 2011), pp. 893–904. ISSN: 0895-0695. DOI: 10.1785/gssrl.82.6.893. URL: <https://doi.org/10.1785/gssrl.82.6.893>.
- [16] Jin Fang et al. "The 2018 Mw 7.5 Palu Earthquake: A Supershear Rupture Event Constrained by InSAR and Broadband Regional Seismograms". en. In: *Remote Sensing* 11.11 (Jan. 2019). Number: 11 Publisher: Multidisciplinary Digital Publishing Institute, p. 1330. ISSN: 2072-4292. DOI: 10.3390/rs11111330. URL: <https://www.mdpi.com/2072-4292/11/11/1330>.
- [17] Heresh Fattah, Mark Simons, and Piyush Agram. "InSAR Time-Series Estimation of the Ionospheric Phase Delay: An Extension of the Split Range-Spectrum Technique". In: *IEEE Transactions on Geoscience and Remote Sensing* 55.10 (Oct. 2017). Conference Name: IEEE Transactions on Geoscience and Remote Sensing, pp. 5984–5996. ISSN: 1558-0644. DOI: 10.1109/TGRS.2017.2718566.
- [18] A. Ferretti, C. Prati, and F. Rocca. "Nonlinear subsidence rate estimation using permanent scatterers in differential SAR interferometry". In: *IEEE Transactions on Geoscience and Remote Sensing* 38.5 (Sept. 2000). Conference Name: IEEE Transactions on Geoscience and Remote Sensing, pp. 2202–2212. ISSN: 1558-0644. DOI: 10.1109/36.868878.

- [19] A. Ferretti, C. Prati, and F. Rocca. “Permanent scatterers in SAR interferometry”. In: *IEEE Transactions on Geoscience and Remote Sensing* 39.1 (Jan. 2001). Conference Name: IEEE Transactions on Geoscience and Remote Sensing, pp. 8–20. ISSN: 1558-0644. DOI: 10.1109/36.898661.
- [20] Eric Jameson Fielding et al. “Surface deformation related to the 2019 M $w\ 7.1$ and 6.4 Ridgecrest earthquakes in California from GPS, SAR interferometry, and SAR pixel offsets”. In: *Seismological Research Letters* 91.4 (2020). Publisher: Seismological Society of America, pp. 2035–2046.
- [21] Africa Ixmeca Flores-Anderson et al. *The SAR Handbook: Comprehensive Methodologies for Forest Monitoring and Biomass Estimation*. Apr. 2019. URL: <https://ntrs.nasa.gov/citations/20190002563>.
- [22] Michael Foumelis et al. “ESA SNAP-StaMPS integrated processing for Sentinel-1 persistent scatterer interferometry”. In: *IGARSS 2018-2018 IEEE International Geoscience and Remote Sensing Symposium*. IEEE, 2018, pp. 1364–1367.
- [23] Satoshi Fujiwara et al. “Non-tectonic liquefaction-induced large surface displacements in the Aso Valley, Japan, caused by the 2016 Kumamoto earthquake, revealed by ALOS-2 SAR”. en. In: *Earth and Planetary Science Letters* 474 (Sept. 2017), pp. 457–465. ISSN: 0012-821X. DOI: 10.1016/j.epsl.2017.07.001.
- [24] Andrew K. Gabriel, Richard M. Goldstein, and Howard A. Zebker. “Mapping small elevation changes over large areas: Differential radar interferometry”. en. In: *Journal of Geophysical Research: Solid Earth* 94.B7 (1989), pp. 9183–9191. ISSN: 2156-2202. DOI: 10.1029/JB094iB07p09183.
- [25] R. M. Goldstein and H. A. Zebker. “Interferometric radar measurement of ocean surface currents”. en. In: *Nature* 328.6132 (Aug. 1987). Number: 6132 Publisher: Nature Publishing Group, pp. 707–709. ISSN: 1476-4687. DOI: 10.1038/328707a0. URL: <https://www.nature.com/articles/328707a0>.
- [26] Richard M. Goldstein, Howard A. Zebker, and Charles L. Werner. “Satellite radar interferometry: Two-dimensional phase unwrapping”. In: *Radio science* 23.4 (1988). Publisher: AGU, pp. 713–720.
- [27] Giorgio Gomba et al. “Toward Operational Compensation of Ionospheric Effects in SAR Interferograms: The Split-Spectrum Method”. In: *IEEE Transactions on Geoscience and Remote Sensing* 54.3 (Mar. 2016). Conference Name: IEEE Transactions on Geoscience and Remote Sensing, pp. 1446–1461. ISSN: 1558-0644. DOI: 10.1109/TGRS.2015.2481079.
- [28] Leroy C. Graham. “Synthetic interferometer radar for topographic mapping”. In: *Proceedings of the IEEE* 62.6 (1974). Publisher: IEEE, pp. 763–768.

- [29] R. A. Green. “Geotechnical Reconnaissance of the 2010 Darfield (New Zealand) Earthquake”. In: (2010). Publisher: GEER Association. DOI: 10 . 18118 / G6D59F. URL: http://geerassociation.org/administrator/components/com_geer_reports/geerfiles/GEER_Darfield_2010_11-14-2010.pdf.
- [30] *Hase: Change of sedimentary facies and topographic... - Google Scholar.*
- [31] A. Hooper, P. Segall, and H. Zebker. “Persistent scatterer interferometric synthetic aperture radar for crustal deformation analysis, with application to Volcán Alcedo, Galápagos”. en. In: *Journal of Geophysical Research: Solid Earth* 112.B7 (2007). _eprint: <https://onlinelibrary.wiley.com/doi/pdf/10.1029/2006JB004763>. ISSN: 2156-2202. DOI: 10 . 1029 / 2006JB004763. URL: <https://onlinelibrary.wiley.com/doi/abs/10.1029/2006JB004763>.
- [32] Andrew Hooper. “A multi-temporal InSAR method incorporating both persistent scatterer and small baseline approaches”. en. In: *Geophysical Research Letters* 35.16 (2008). _eprint: <https://onlinelibrary.wiley.com/doi/pdf/10.1029/2008GL034654>. ISSN: 1944-8007. DOI: 10 . 1029 / 2008GL034654. URL: <https://onlinelibrary.wiley.com/doi/abs/10.1029/2008GL034654>.
- [33] Andrew Hooper et al. “Recent advances in SAR interferometry time series analysis for measuring crustal deformation”. en. In: *Tectonophysics* 514-517 (Jan. 2012), pp. 1–13. ISSN: 0040-1951. DOI: 10 . 1016 / j . tecto . 2011 . 10 . 013. URL: <https://www.sciencedirect.com/science/article/pii/S0040195111004343>.
- [34] Andrew John Hooper. “Persistent scatter radar interferometry for crustal deformation studies and modeling of volcanic deformation”. English. ISBN: 9780542706905. Ph.D.
- [35] M. Ideue and S. A. Watanabe. “Study on the River-Bed Gravel of Midori River in Kumamoto as Materials for Teaching Science—A Link between Elementary Science Teaching Materials with a Welded Tuff as a Key; University of Kumamoto Repository”. In: *Natural Science Department: Kumamoto, Japan* (2012), pp. 47–56.
- [36] Tatsuya Ishikawa et al. “Reconnaissance report on geotechnical damage caused by 2018 Hokkaido Eastern Iburi earthquake with JMA seismic intensity 7”. en. In: *Soils and Foundations* 61.4 (Aug. 2021), pp. 1151–1171. ISSN: 0038-0806. DOI: 10 . 1016 / j . sandf . 2021 . 06 . 006. URL: <https://www.sciencedirect.com/science/article/pii/S003808062100086X>.
- [37] Kazuya Ishitsuka, Takeshi Tsuji, and Toshifumi Matsuoka. “Detection and mapping of soil liquefaction in the 2011 Tohoku earthquake using SAR interferometry”. en. In: *Earth, Planets and Space* 64.12 (Dec. 2012). Number: 12 Publisher: SpringerOpen, pp. 1267–1276. ISSN: 1880-5981. DOI: 10 . 5047 / eps . 2012 . 11 . 002. URL: <https://earth-planets-space.springeropen.com/articles/10.5047/eps.2012.11.002>.
- [38] T. Ito. “Active faulting, lower crustal delamination and ongoing Hidaka arc-arc collision, Hokkaido, Japan”. In: *Seismotectonics in Convergent Plate Boundary* (2002). Publisher: Terrapub, pp. 219–224.

- [39] Bert M. Kampes. "Displacement parameter estimation using permanent scatterer interferometry". In: (2005).
- [40] *Kato: The 2016 Kumamoto earthquake sequence - Google Scholar.*
- [41] R. Kayen. "Geotechnical Aspects of the 2016 MW 6.2, MW 6.0, and MW 7.0 Kumamoto Earthquakes". In: (2016). Publisher: GEER Association. DOI: 10.18118/G6JS3M. URL: http://geerassociation.org/administrator/components/com_geer_reports/geerfiles/GEER_Kumamoto_V1_07_13_2016.pdf.
- [42] R. Kayen. *Seismological, Geological, and Geotechnical Engineering Aspects of the 2018 MW 6.6 Hokkaido Eastern Iburi Earthquake*. 2019. DOI: 10.18118/G6CM1K. URL: http://www.geerassociation.org/component/geer_reports/?view=geerreports&id=87&layout=build.
- [43] T. Kobayashi et al. "Liquefaction area associated with the 2011 off the Pacific coast of Tohoku earthquake inferred from interferometric SAR coherence change". In: *J Geosp Inf Auth Jpn* 122 (2011), pp. 143–151.
- [44] Tomokazu Kobayashi, Kyonosuke Hayashi, and Hiroshi Yarai. "Geodetically estimated location and geometry of the fault plane involved in the 2018 Hokkaido Eastern Iburi earthquake". en. In: *Earth, Planets and Space* 71.1 (May 2019), p. 62. ISSN: 1880-5981. DOI: 10.1186/s40623-019-1042-6. URL: <https://doi.org/10.1186/s40623-019-1042-6>.
- [45] Steven Lawrence Kramer. *Geotechnical earthquake engineering*. Pearson Education India, 1996.
- [46] Suzanne Lyons and David Sandwell. "Fault creep along the southern San Andreas from interferometric synthetic aperture radar, permanent scatterers, and stacking". In: *Journal of Geophysical Research: Solid Earth* 108.B1 (2003). Publisher: Wiley Online Library.
- [47] B. Mason. "The 28 September 2018 M7.5 Palu-Donggala, Indonesia Earthquake". In: (2019). Publisher: GEER Association (Report - 61). DOI: 10.18118/G63376. URL: http://www.geerassociation.org/administrator/components/com_geer_reports/geerfiles/GEER_Palu_Version_1.pdf.
- [48] Koji Okumura. "Earthquake geology of the April 14 and 16, 2016 Kumamoto earthquakes". In: *Kumamoto earthquake investigation: a preliminary report*. http://janet-dr.com/11_saigaiji/The%20Kumamoto%20Earthquake%20Investigation-%20A%20Preliminary%20Report.pdf. Accessed 11 (2016).
- [49] R. P. Orense et al. "Comparison of liquefaction Features observed during the 2010 and 2011 Canterbury earthquakes". In: *Seismological Research Letters* 82.6 (Nov. 2011), pp. 905–918. ISSN: 0895-0695. DOI: 10.1785/gssrl.82.6.905. URL: <https://doi.org/10.1785/gssrl.82.6.905>.

- [50] Bryan Riel, Brent Minchew, and Ian Joughin. “Observing traveling waves in glaciers with remote sensing: New flexible time series methods and application to Sermeq Kujalleq (Jakobshavn Isbræ), Greenland”. In: (2020). Publisher: EarthArXiv.
- [51] K. Robinson et al. “Field measurements of lateral spreading following the 2010 Darfield earthquake”. In: *Proceedings of the Ninth Pacific Conference on Earthquake Engineering*. Vol. 14. 2011, p. 16.
- [52] P. A. Rosen et al. “The InSAR scientific computing environment (isce): a python framework for earth science”. In: *Agu fall meeting abstracts*. Vol. 2015. 2015, IN11C–1789.
- [53] Paul A. Rosen et al. “The InSAR scientific computing environment”. In: *EUSAR 2012; 9th European Conference on Synthetic Aperture Radar*. Apr. 2012, pp. 730–733.
- [54] Paul A. Rosen et al. “The InSAR Scientific Computing Environment 3.0: A Flexible Framework for NISAR Operational and User-Led Science Processing”. In: *IGARSS 2018 - 2018 IEEE International Geoscience and Remote Sensing Symposium*. ISSN: 2153-7003. July 2018, pp. 4897–4900. DOI: 10.1109/IGARSS.2018.8517504.
- [55] Hendra Setiawan et al. “Structural damage to houses and buildings induced by liquefaction in the 2016 Kumamoto Earthquake, Japan”. en. In: *Geoenvironmental Disasters* 4.1 (Apr. 2017), p. 13. ISSN: 2197-8670. DOI: 10.1186/s40677-017-0077-x. URL: <https://doi.org/10.1186/s40677-017-0077-x>.
- [56] A. Singleton et al. “Evaluating sub-pixel offset techniques as an alternative to D-InSAR for monitoring episodic landslide movements in vegetated terrain”. en. In: *Remote Sensing of Environment* 147 (May 2014), pp. 133–144. ISSN: 0034-4257. DOI: 10.1016/j.rse.2014.03.003. URL: <https://www.sciencedirect.com/science/article/pii/S0034425714000686>.
- [57] Anne Socquet et al. “Evidence of supershear during the 2018 magnitude 7.5 Palu earthquake from space geodesy”. en. In: *Nature Geoscience* 12.3 (Mar. 2019). Number: 3 Publisher: Nature Publishing Group, pp. 192–199. ISSN: 1752-0908. DOI: 10.1038/s41561-018-0296-0. URL: <https://www.nature.com/articles/s41561-018-0296-0>.
- [58] Luyi Sun and Jan-Peter Muller. “Evaluation of the Use of Sub-Pixel Offset Tracking Techniques to Monitor Landslides in Densely Vegetated Steeply Sloped Areas”. en. In: *Remote Sensing* 8.8 (Aug. 2016). Number: 8 Publisher: Multidisciplinary Digital Publishing Institute, p. 659. ISSN: 2072-4292. DOI: 10.3390/rs8080659. URL: <https://www.mdpi.com/2072-4292/8/8/659>.
- [59] Machiko Tamaki, Shigekazu Kusumoto, and Yasuto Itoh. “Formation and deformation processes of late Paleogene sedimentary basins in southern central Hokkaido, Japan: paleomagnetic and numerical modeling approach”. In: *Island Arc* 19.2 (2010). Publisher: Wiley Online Library, pp. 243–258.

- [60] Noppawan Tamkuan and Masahiko Nagai. "Fusion of Multi-Temporal Interferometric Coherence and Optical Image Data for the 2016 Kumamoto Earthquake Damage Assessment". en. In: *ISPRS International Journal of Geo-Information* 6.7 (July 2017). Number: 7 Publisher: Multidisciplinary Digital Publishing Institute, p. 188. ISSN: 2220-9964. DOI: 10.3390/ijgi6070188. URL: <https://www.mdpi.com/2220-9964/6/7/188>.
- [61] M. Tamura and T. El-Gharbawi. "Mapping damage in Ishinomaki city due to the 2011 Tohoku Earthquake using". In: *SAR coherence change, proceedings of the 58th spring conference of the remote sensing society of Japan*. 2015, pp. 29–30.
- [62] Takeshi Tsuji et al. "Horizontal sliding of kilometre-scale hot spring area during the 2016 Kumamoto earthquake". In: *Scientific reports* 7.1 (2017). Publisher: Nature Publishing Group UK London, p. 42947.
- [63] Yongzhe Wang et al. "Source Characteristics of the 28 September 2018 Mw 7.4 Palu, Indonesia, Earthquake Derived from the Advanced Land Observation Satellite 2 Data". en. In: *Remote Sensing* 11.17 (Jan. 2019). Number: 17 Publisher: Multidisciplinary Digital Publishing Institute, p. 1999. ISSN: 2072-4292. DOI: 10.3390/rs11171999. URL: <https://www.mdpi.com/2072-4292/11/17/1999>.
- [64] Manabu Watanabe et al. "Detection of damaged urban areas using interferometric SAR coherence change with PALSAR-2". In: *Earth, Planets and Space* 68.1 (July 2016), p. 131. ISSN: 1880-5981. DOI: 10.1186/s40623-016-0513-2. URL: <https://doi.org/10.1186/s40623-016-0513-2>.
- [65] Ian M. Watkinson and Robert Hall. "Impact of communal irrigation on the 2018 Palu earthquake-triggered landslides". en. In: *Nature Geoscience* 12.11 (Nov. 2019). Number: 11 Publisher: Nature Publishing Group, pp. 940–945. ISSN: 1752-0908. DOI: 10.1038/s41561-019-0448-x. URL: <https://www.nature.com/articles/s41561-019-0448-x>.
- [66] Urs Wegmüller et al. "Reformulating the Split-Spectrum Method to Facilitate the Estimation and Compensation of the Ionospheric Phase in SAR Interferograms". en. In: *Procedia Computer Science*. CENTERIS 2018 - International Conference on ENTERprise Information Systems / ProjMAN 2018 - International Conference on Project MANagement / HCist 2018 - International Conference on Health and Social Care Information Systems and Technologies, CENTERIS/ProjMAN/HCist 2018 138 (Jan. 2018), pp. 318–325. ISSN: 1877-0509. DOI: 10.1016/j.procs.2018.10.045. URL: <https://www.sciencedirect.com/science/article/pii/S1877050918316788>.
- [67] Charles Werner et al. "Interferometric point target analysis for deformation mapping". In: *IGARSS 2003. 2003 IEEE International Geoscience and Remote Sensing Symposium. Proceedings (IEEE Cat. No. 03CH37477)*. Vol. 7. IEEE, 2003, pp. 4362–4364.
- [68] Carl A. Wiley. "Synthetic aperture radars". In: *IEEE Transactions on Aerospace and Electronic Systems* 3 (1985). Publisher: IEEE, pp. 440–443.

- [69] Liam M. Wotherspoon, Michael J. Pender, and Rolando P. Orense. “Relationship between observed liquefaction at Kaiapoi following the 2010 Darfield earthquake and former channels of the Waimakariri River”. en. In: *Engineering Geology* 125 (Jan. 2012), pp. 45–55. ISSN: 0013-7952. DOI: 10.1016/j.enggeo.2011.11.001. URL: <https://www.sciencedirect.com/science/article/pii/S0013795211002808>.
- [70] Hiromitsu Yamagishi and Fumiaki Yamazaki. “Landslides by the 2018 Hokkaido Iburi-Tobu Earthquake on September 6”. In: *Landslides* 15.12 (2018). Publisher: Springer, pp. 2521–2524.
- [71] K. Yoshida, T. Sekiguchi, and T. Nakano. “Mapping of surface cracks derived from the 2016 Kumamoto earthquake”. In: *J Geospatial Info Auth Jpn* 128 (2016), pp. 201–206.
- [72] Chen Yu, Zhenhong Li, and Nigel T. Penna. “Interferometric synthetic aperture radar atmospheric correction using a GPS-based iterative tropospheric decomposition model”. en. In: *Remote Sensing of Environment* 204 (Jan. 2018), pp. 109–121. ISSN: 0034-4257. DOI: 10.1016/j.rse.2017.10.038. URL: <https://www.sciencedirect.com/science/article/pii/S0034425717305011>.
- [73] Chen Yu, Nigel T. Penna, and Zhenhong Li. “Generation of real-time mode high-resolution water vapor fields from GPS observations”. en. In: *Journal of Geophysical Research: Atmospheres* 122.3 (2017), pp. 2008–2025. ISSN: 2169-8996. DOI: 10.1002/2016JD025753.
- [74] Chen Yu et al. “Generic Atmospheric Correction Model for Interferometric Synthetic Aperture Radar Observations”. en. In: *Journal of Geophysical Research: Solid Earth* 123.10 (2018), pp. 9202–9222. ISSN: 2169-9356. DOI: 10.1029/2017JB015305.
- [75] Zhang Yunjun, Heresh Fattah, and Falk Amelung. “Small baseline InSAR time series analysis: Unwrapping error correction and noise reduction”. In: *Computers & Geosciences* 133 (2019). Publisher: Elsevier, p. 104331.
- [76] Howard A. Zebker and Richard M. Goldstein. “Topographic mapping from interferometric synthetic aperture radar observations”. en. In: *Journal of Geophysical Research: Solid Earth* 91.B5 (1986), pp. 4993–4999. ISSN: 2156-2202. DOI: 10.1029/JB091iB05p04993.
- [77] Shuai Zhang et al. “Characteristics of landslides triggered by the 2018 Hokkaido Eastern Iburi earthquake, Northern Japan”. en. In: *Landslides* 16.9 (Sept. 2019), pp. 1691–1708. ISSN: 1612-5118. DOI: 10.1007/s10346-019-01207-6. URL: <https://doi.org/10.1007/s10346-019-01207-6>.
- [78] Hanxu Zhou et al. “Investigation and mechanism analysis of disasters under Hokkaido Eastern Iburi earthquake”. In: *Geomatics, Natural Hazards and Risk* 12.1 (Jan. 2021). Publisher: Taylor & Francis .eprint: <https://doi.org/10.1080/19475705.2020.1856201>, pp. 1–28. ISSN: 1947-5705. DOI: 10.1080/19475705.2020.1856201. URL: <https://doi.org/10.1080/19475705.2020.1856201>.

Appendix A

Manual for InSAR Liquefaction Analysis Workflow

A.1 Find SAR data set

The most commonly used website for accessing SAR data set is ASF Vertex Data Search (<https://search.asf.alaska.edu/>). The screenshot of the website is shown in Figure A.1. From this website Sentinel-1A/B, part of the ALOS-1, ERS and some other SAR data sets can be searched and downloaded. The area of interest, time span and the SAR product type need to be specified for data search. For InSAR time series analysis with ARIA tools and MintPy, the ARIA GUNW products are also hosted by Alaska Satellite Facility (ASF).

If the SAR data set for the research cannot be found on ASF's website, there are other websites as well. For example, ENVISAT data set can be accessed from European Space Agency (ESA)'s website, and ALOS-1, ALOS-2 data set can be purchased from JAXA if the cost fits the budget. Note that the common file types for InSAR analysis are Level 1.0 raw product and Level 1.1 single look complex (SLC) product.

A.2 ISCE2 workflow

InSAR Scientific Computing Environment (ISCE2) developed by NASA Jet Propulsion Laboratory (JPL) is the most mature InSAR processing package at present. The best way to access ISCE2 is using the docker image built by Alaska Satellite Facility (ASF). The tutorial of installing this docker image can be found from ASF OpenSARLab's GitHub (<https://github.com/ASFOpenSARlab/opensarlab-docker/tree/main/unavco2022>). Note that this docker image does not support Mac system with Apple silicon at the moment.

ISCE2 has stripmap and tops mode processing built in. It is also built to work with ARIA tools and MintPy for SBAS time series analysis. Since ISCE2 is implemented in Python, there are other Python scripts for generating interferogram stacks contributed by community members. The atmospheric phase correction and pixel offset method are built

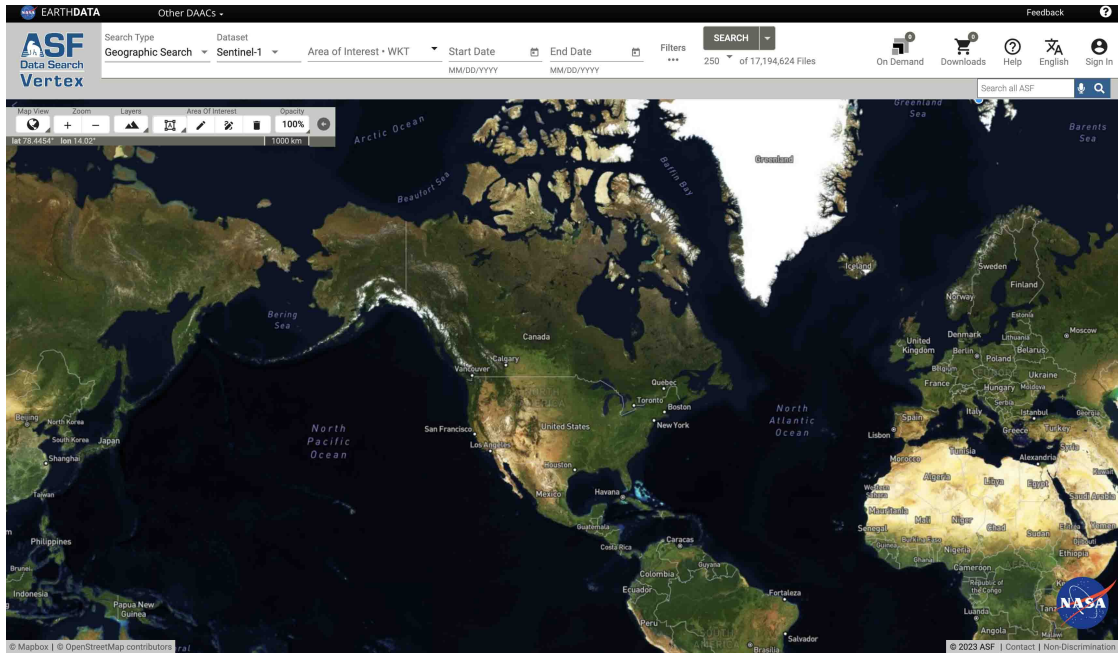


Figure A.1: ASF Vertex Data Search Website

in ISCE2 that need to be activated in the configuration file (.xml file). There is a free short InSAR processing course hosted by UNAVCO every year (<https://www.unavco.org/event/2022-short-course-insar-processing-analysis-isce/>). This is a great start for learning how to use ISCE2. The video recordings of the past courses can be found at UNAVCO’s YouTube channel (<https://www.youtube.com/@unavcovideos>). It is recommended to watch the videos of the past courses and work through the Jupyter notebooks on Geo-SInC’s GitHub (<https://github.com/parosen/Geo-SInC/tree/main/UNAVC02022>) before participating the short course.

ISCE2 is open source and easy to use with Jupyter notebook. But there are several points to be careful about when using ISCE2:

- Be careful about the configuration file for SAR images. Different satellites may have different formats.
- Check the result after ionosphere phase correction. If the result does not make sense, tune the parameters within the configuration file.
- Tune the parameters of pixel offset method to get better results even though the result with default parameters is usually decent. But there is one downside, the pixel offset method built within the StripMapApp.py does not have geocoding functionality. Geocoding needs to be done manually afterwards in post processing softwares.

- Check the connected component product generated by phase unwrapping to have a better understanding on the quality of phase unwrapping. This is a crucial step before using the phase unwrapping results for displacement analysis.
- Relative displacement is more useful for InSAR analysis. Select the appropriate reference points for different areas of interest. The rule of thumb is that the reference point must be stable and relatively close to the area of interest. The reference point is also crucial for getting rid of local tectonic displacements.

A.3 PS analysis workflow

After downloading the SAR data sets for PS analysis (Note that this workflow only works with Sentinel-1A/B data sets at the moment.), the pre-processing is performed in the SAR processing software named SNAP created by ESA (<https://step.esa.int/main/download/snap-download/>). SNAP2STAMPS (<https://github.com/mdelgadoblasco/snap2stamps>) is a useful package for automating the preprocessing within SNAP and generating the products that are compatible with StaMPS. Manual preprocessing in SNAP is only needed for the master image selected by the "InSAR Stack Overview" function of SNAP. Afterwards, the preprocessing of other SAR images can be done automatically with the python scripts in SNAP2STAMPS. The final output of SNAP2STAMPS should contain four folders: rslc, diff0, geo and dem.

StaMPS (<https://github.com/dbekaert/StaMPS>) is implemented to work within MATLAB. Before feeding the output of SNAP2STAMPS to StaMPS, the mt_prep_snap script must be run first to finish the final preparation before the StaMPS analysis. Follow the steps 1 to 7 of StaMPS, and then the average velocity map of all the persistent scatterers in mm/yr can be generated with the command: ps_plot('v-do'. 'ts'). The LOS displacement time series plot of a certain location can be generated by clicking on the map. Note that the reference point must be set before this step.

The tutorial on how to prepare the environment for StaMPS analysis and the detailed processing steps is created by a community contributor named Gijs on the step forum (<https://forum.step.esa.int/t/documentation-on-snap-stamps-workflow/17775>). Apart from the content of this tutorial, there are some extra points to be careful about on this workflow:

- It is recommended to perform this entire workflow on Linux. Ubuntu 20.04 LTS is the best option for Linux because it is the latest version without leading to errors related to C compiler version.
- Remember to make the change shown in Figure A.2 before using SNAP2STAMPS.
- To avoid issues related to the version of packages, Conda is a useful tool for creating appropriate processing environments in different scenarios.

Try to change

```
<useSuppliedShifts>false</useSuppliedShifts>
to
<useSuppliedRangeShift>false</useSuppliedRangeShift>
<useSuppliedAzimuthShift>false</useSuppliedAzimuthShift>
```

in coreg_ifg_computation.xml file

Figure A.2: Modification required before using SNAP2STAMPS

- It is important to check whether the result of StaMPS makes sense. If not, get rid of the problematic scenes and re run the analysis.

A.4 Post-processing in QGIS workflow

QGIS is a free open source GIS software (<https://qgis.org/en/site/>). QGIS' functionality is on the same level as ArcGIS but the operation in QGIS has more freedom because it is open source. All the post-processing work of this research was done by QGIS. The key step is to convert the products from ISCE2 and StaMPS to the format that is compatible with QGIS.

All the outputs from ISCE2 (coherence, unwrapped phase, LOS displacements, incidence angle etc.) can be converted to GeoTIFF format with the gdal_translate function in the GDAL package (<https://gdal.org/>). Then the GeoTIFF file can be read by QGIS by adding raster layer.

As stated in Chapter 5, some modifications was made to the StaMPS analysis in this research. To output the co-seismic LOS displacement of all persistent scatterers in CSV format, the MATLAB script shown in Figure A.3 was used. Note that the indices of the co-seismic scenes need to be adjusted in different projects. QGIS can then read the CSV file by adding delimited text layer.

Within QGIS, the calculation with raster data set is performed with raster calculator and the calculation with vector data set is performed with field calculator. the combination of different tools within QGIS can realize many powerful functions like the 3D decomposition of LOS displacements. It is also important to learn how to create maps with QGIS since it is the best way to present the final results.

The 3D decomposition of LOS displacements in PS analysis must be formed manually as discussed in Chapter 5. One example of the python script can be found here https://colab.research.google.com/drive/17Epjowq0Y_sE2cAmu2mPPmj1ZFNe1e_. The incidence angle and the LOS displacements on the ascending and descending track can be extracted from QGIS with the identify feature tool.



```

1 load parms.mat;
2 ps_plot('v-do', -1);
3 load ps_plot_v-do.mat;
4 lon2_str = cellstr(num2str(lon2));
5 lat2_str = cellstr(num2str(lat2));
6 lonlat2_str = strcat(lon2_str, lat2_str);
7
8 lonlat_str = strcat(cellstr(num2str(lonlat(:,1))), cellstr(num2str(lonlat(:,2))));
9 %ind = ismember(lonlat_str, lonlat2_str);
10
11 lon = lonlat(:,1);
12 lat = lonlat(:,2);
13
14
15 %disp = ph_disp(ind);
16 %disp_ts = ph_mm(ind,:);
17 disp_co_seismic = ph_mm(:,2) - ph_mm(:,3);
18 export_res = [lon lat ph_disp ph_mm disp_co_seismic];
19
20 export_res = table(export_res);
21 writetable(export_res, 'stamps_tsexport.csv')

```

Figure A.3: MATLAB script used to generate outputs in CSV format

Finally, the georeferencer tool in QGIS can help solving the problem that pixel offset method in StripMapApp.py does not have the geocoding functionality. Georeferencer is also a powerful tool to overlay existing maps to the InSAR analysis results. There are a lot more functions in QGIS that are not covered by this manual. It is a good practice to explore new functions that can make the post-processing work more efficient.